LA-UR- 98-4759

Title:

Unsaturated Groundwater Flow beneath Upper Mortandad Canyon, Los Alamos, New Mexico

Author(s):

David Carl Dander
Water Quality and Hydrology Group,
ESH-18,
Los Alamos National Laboratory

October 15, 1998

Submitted to:

Los Alamos
NATIONAL LABORATORY

UNSATURATED GROUNDWATER FLOW BENEATH UPPER MORTANDAD CANYON, LOS ALAMOS, NEW MEXICO

by

David Carl Dander

A Thesis Submitted to the Faculty of the
DEPARTMENT OF HYDROLOGY AND WATER RESOURCES

In Partial Fulfillment of the Requirements
For the Degree of
MASTER OF SCIENCE
WITH A MAJOR IN HYDROLOGY

In the Graduate College
THE UNIVERSITY OF ARIZONA

1 9 9 8

STATEMENT BY AUTHOR

This thesis has been submitted in partial fulfillment of requirements for an advanced degree at The University of Arizona and is deposited in the University Library to be made available to borrowers under rules of the Library.

Brief quotations from this thesis are allowable without special permission, provided that accurate acknowledgment of source is made. Requests for permission for extended quotation from or reproduction of this manuscript in whole or in part may be granted by the head of the major department or the Dean of the Graduate College when in his or her judgment the proposed use of the material is in the interests of scholarship. In all other instances, however, permission must be obtained from the author.

SIGNED: ______________________________

APPROVAL BY THESIS DIRECTORS

This thesis has been approved on the date shown below:

______________________________	______________________
Dr. James E. Smith Adjunct Assistant Professor of Hydrology and Water Resources	Date
______________________________	______________________
Dr. Thomas Maddock III. Professor of Hydrology and Water Resources	Date

ACKNOWLEDGMENTS

Funding for this research was provided by Los Alamos National Laboratories (LANL's) Water Quality and Hydrology Group, ESH-18 with some assistance by a partial Graduate Research Fellowship granted from Associated Western Universities.

Thesis committee members who provided much appreciated assistance, guidance, and knowledge included Dr. David B. Rogers of LANL; Dr. James Smith and Dr. Thomas Maddock III. of the UA Department of Hydrology and Water Resources; and Dr. Arthur Warrick of UA Department of Soil, Water and Environmental Sciences.

Many members of LANL's Geoanalysis Group, EES-5, provided greatly appreciated help and assistance in using their own Finite Element Heat and Mass Transfer Code (FEHM) which was used extensively in this study.

Secretarial and administrative assistance from both LANL and UA are also appreciated, thanks. And finally, thanks to friends and family for support.

Contributors	Affiliation	Summary of Contribution
James Smith	UA, HWR	Thesis supervisor, committee member
Thomas Maddock III	UA, HWR	Academic supervisor, committee member
Arthur Warrick	UA, SWES	Thesis committee member
David Rogers	LANL, ESH-18	Research advisement/supervisor, committee member
Steve Rae	LANL, ESH-18	Funding arrangements
Bruce Gallaher	LANL, ESH-18	Funding arrangements, Hydrology guidance
Steve McLin	LANL, ESH-18	Hydrology guidance
Ernestine Martinez	LANL, ESH-18	Clerical assistance
Chris McLean	LANL, ESH-18	Computing and editorial assistance
Ramon Naranjo	LANL, ESH-18	Technical and editorial assistance
Larry Pratt	LANL, ESH-18	Technical and editorial assistance
William Turney	LANL, ESH-18	Technical and editorial assistance
Bill Purtymun	LANL, ESH-18	Research and x-section development assistance
Carl Gable	LANL, EES-5	Grid, code output, and FEHM assistance
Katherine Birdsell	LANL, EES-5	Hydrology and modeling knowledge
Andy Wolfsburg	LANL, EES-5	FEHM code support, Modeling guidance
George Zyvoloski	LANL, EES-5	FEHM code support
Bruce Robinson	LANL, EES-5	FEHM code support
Lynn McDonald	LANL, EES-5	Computing assistance
Phil Stauffer	LANL, EES-5	FEHM code support, Modeling guidance
Daniel Tartakovsky	LANL, EES-5	Grid and modeling assistance
Guy Romer	LANL, EES-5	FEHM code support, Modeling guidance
Alan Stoker	LANL, SAIC	Research and x-section development assistance
Richard Koch	LANL, SAIC	Research and x-section development assistance
Patrick Longmire	LANL, CST-7	Research and cross-section development assistance
David Broxton	LANL, EES-1	Research and cross-section development assistance
Josh Smith	LANL, CST-DO	Technical editing and illustration assistance
Corrie Thies	UA, HWR	Editing Assistance
Terrie Thompson	UA, HWR	Academic Advisement and Clerical assistance
Carol Johnson	Friend, PC support	Assistance with home computing problems
Robert & Carla Dander	Parents, family	Financial assistance, use of computer/other resources

TABLE OF CONTENTS

LIST OF ILLUSTRATIONS

LIST OF TABLES

ABSTRACT

Mortandad Canyon is a discharge site for treated industrial effluents containing radionuclides and other chemicals at Los Alamos National Laboratory, New Mexico. This study was conducted to develop an understanding of the unsaturated hydrologic behavior below the canyon floor. The main goal of this study was to evaluate the hypothetical performance of the vadose zone above the water table. Numerical simulations of unsaturated groundwater flow at the site were conducted using the Finite Element Heat and Mass Transfer (FEHM) code. A two-dimensional cross-section along the canyon's axis was used to model flow between an alluvial groundwater system and the regional aquifer approximately 300 m below. Using recharge estimated from a water budget developed in 1967, the simulations showed waters from the perched water table reaching the regional aquifer in 13.8 years, much faster than previously thought. Additionally, simulations indicate that saturation is occurring in the Guaje pumice bed and that the Tshirege Unit 1B is near saturation. Lithologic boundaries between the eight materials play an important role in flow and solute transport within the system. Horizontal flow is shown to occur in three thin zones above capillary barriers; however, vertical flow dominates the system. Other simulations were conducted to examine the effects of changing system parameters such as varying recharge inputs, varying the distribution of recharge, and bypassing fast-path fractured basalt of uncertain extent and properties. System sensitivity was also explored by changing model parameters with respect to size and types of grids and domains, and the presence of dipping stratigraphy.

1. INTRODUCTION

1.1. INTRODUCTION

Los Alamos National Laboratory (LANL) has been in operation since 1942. Many of the research activities of the Laboratory involve the use of hazardous and radioactive materials. For many years, treated and untreated effluents resulting from these activities were released directly into the environment. Today, disposal of Laboratory effluents into the environment is heavily regulated and monitored. The Laboratory is presently required to comply with many federal and state environmental programs geared towards protecting the environment.

Groundwater flow is a likely mechanism for transporting potential contaminants beneath the laboratory. For the most part, 111 km^2 (43 mi^2) of LANL lands can be divided into two environments: mesas and canyons. The greatest likelihood for water and contaminant movement may arise from infiltration beneath canyon bottoms and is the focus area of this study. The nature and extent of unsaturated flow beneath a western portion of the canyon, otherwise known and referred to as Upper Mortandad Canyon, is examined.

Mortandad Canyon, located in north-central New Mexico, is approximately 30 km northwest of Santa Fe between the towns of Los Alamos and White Rock (Figure 1.1). The canyon originates within the boundaries of Los Alamos National Laboratory and

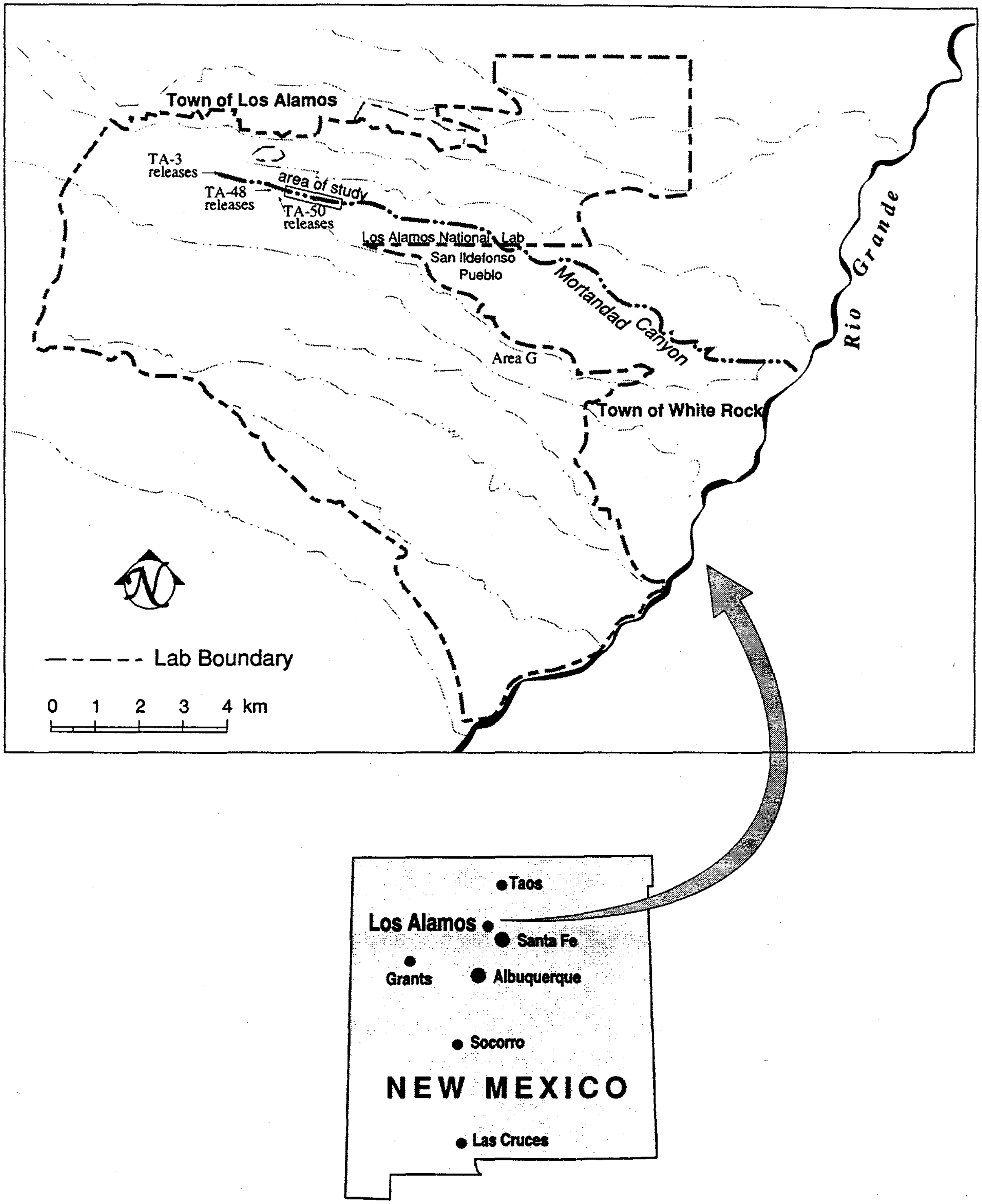

Figure 1.1 Regional location of Los Alamos National Laboratory.

extends about 16 km in an easterly direction to the Rio Grande. The upper 7 km of the canyon is on lands belonging to LANL, and the lower 9 km is on lands belonging to San Ildefonso Pueblo.

The canyon cuts into a sequence of volcanic tuffs underlain by other volcanic and sedimentary rocks on the Pajarito Plateau (Figure 1.2). The Plateau lies on the southeastern slopes of the Valles Caldera. Some aspects of the canyon's geometry and geology influence the hydrologic system within. In general, the hydrologic system consists of an intermittent stream, a shallow alluvial perched groundwater system, a thick unsaturated zone, and a deep regional aquifer. The stream flow is supplied by LANL effluents, snow melt, and storm runoff. Stream flow rarely exists below Upper Mortandad Canyon except during flood events. The shallow alluvial groundwater system extends through Upper Mortandad Canyon and another 2 km down canyon. Water in the regional aquifer flows east, about 300 m below the canyon floor. Most of the intervening rock between these two saturated systems is unsaturated (Stoker et al., 1991, Purtymun, 1995).

There are several potential sources of contamination entering the canyon; however, the source of most interest is the discharge from the Radioactive Waste Liquid Treatment Facility. Beginning in June 1963, treated effluents from this facility have been released into Upper Mortandad Canyon. Aside from ramifications of contaminants entering the system, the additional source of water has altered the natural system.

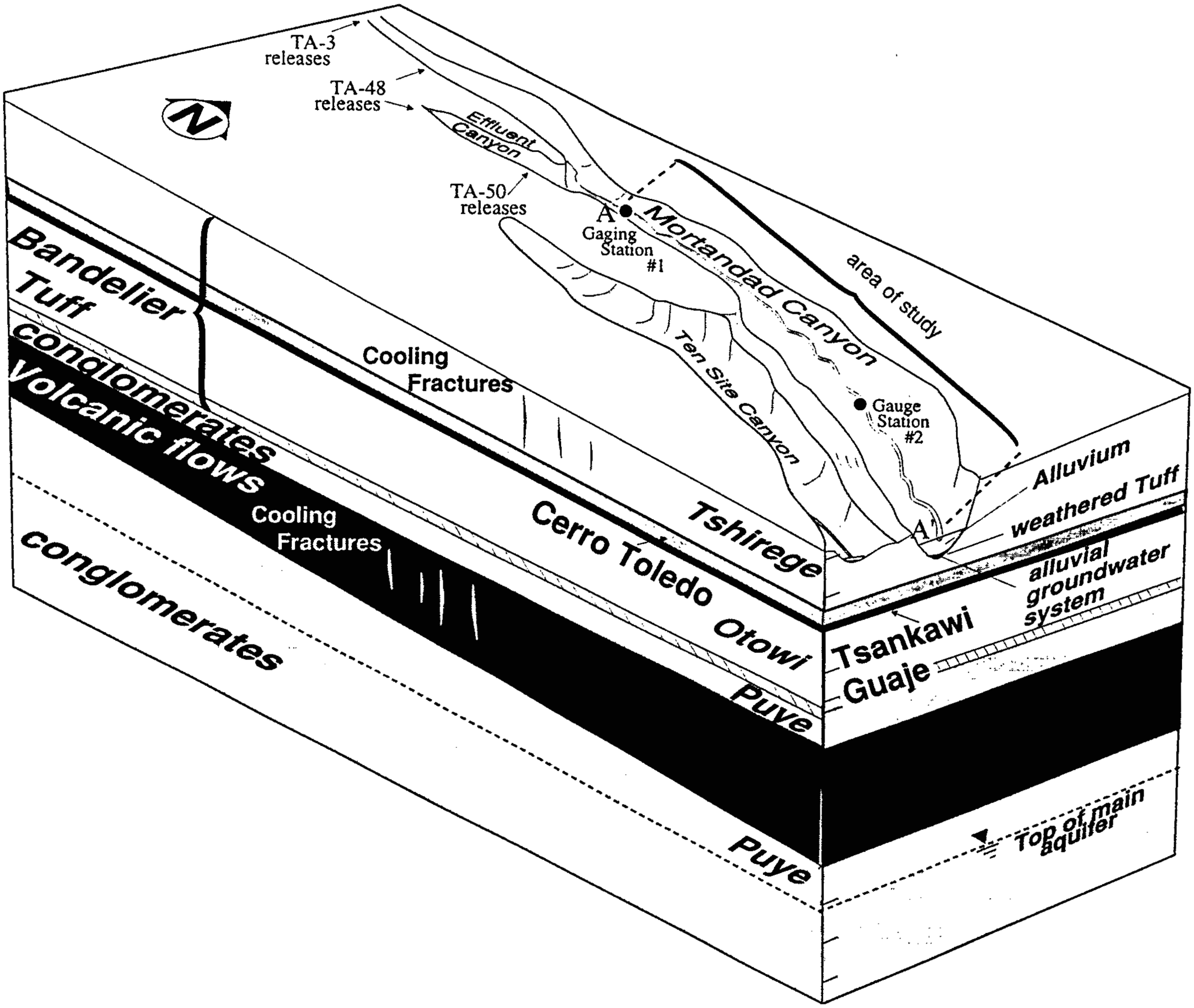

Figure 1.2 **Block diagram of Mortandad Canyon.**

Shallow groundwater flow within LANL in Mortandad Canyon has been modeled in several studies. However, these models did not include much of the deeper materials below the saturated-unsaturated interface at the base of the alluvium. Two studies that included modeling of saturated-unsaturated contaminant migration in the perched aquifer were conducted by Vollick (1992) and Mostafa (1993). Their models included a no flow lower boundary condition between 2 m to 15 m below the alluvium-tuff interface, thus neglecting leakage (or recharge) to the lower units. A study by Koenig and McLin (1992) used a lumped parameter model to examine the behavior of the perched groundwater system throughout the canyon. Their study examines and incorporates monthly water budget calculations at several locations by Purtymun (1967). They conclude that most (>75%) of the water in the system leaves as seepage into the tuff (Koenig and McLin, 1992). Another study by Stone (1995) included modeling of pre-1960 (before effluents) saturated groundwater flow using a no flow lower boundary at the base of the alluvium. The model was designed to help estimate recharge from surplus water in the domain; however results are preliminary. Preliminary modeling by Geddis (1992) examines flow in the upper unsaturated zone, below the perched groundwater system. Whereas other studies modeled the canyon along its axis, he conducted simulations of a cross-section perpendicular to the canyon about 2 km downstream from the Radioactive Waste Liquid Treatment Facility discharge point. He uses specified head and specified flux for a small part of the upper boundary, and a no flow conditions for the remaining boundaries. His work illustrates the importance of many simulation differences incorporated in this study, major differences include: Code selection, depth modeled, grid orientation, representing dipping stratigraphy, boundary conditions, variable recharge scenarios, and proximity of simulation domain to primary recharge source. These differences are described in the following section.

Unsaturated flow behavior at other sites, similar in geology and hydrology to Mortandad Canyon, has been modeled and is well-documented. Studies and modeling at Yucca Mountain by Montazer and Wilson (1984) and elsewhere at LANL by Birdsell et al. (1997) describe important aspects of geohydrology that influence flow and need to be explored and documented for this site.

> "The presence of certain hydrogeologic features affects flow in the unsaturated zone. These features include the presence of fractured porous media, layered units with contrasting physical properties, dipping units, and a deep water table resulting in a very thick unsaturated zone. The combination of these features provides a hydrogeologic framework that probably results in certain flow phenomena, namely infiltration and flow through fractured rocks, retardation of flow by capillary barriers, lateral flow, and vapor flow." (Montazer and Wilson, 1984)

Understanding these concepts and the unsaturated flow beneath the canyon is important in determining how contaminants may be transported within this and possibly other systems at LANL. This understanding is useful for monitoring and planning purposes related to other LANL programs such as the hydrogeologic workplan.

1.2 OBJECTIVES AND SCOPE OF WORK

The surface water and alluvial groundwater systems in Mortandad and surrounding canyons are fairly well characterized; however, knowledge of this unsaturated system is limited.

The main goal of this study is to evaluate the nature and extent of the unsaturated system beneath Upper Mortandad Canyon. The following questions are addressed:

- What role might recharge play in the distribution and movement of the water?
- At what rate and directions might water be moving within this unsaturated zone?
- How might the water within this unsaturated zone be distributed?

This modeling study uses a numerical model, FEHM (Finite Element Heat and Mass Transfer) by Zyvoloski et al. (1994b), to simulate unsaturated flow. It addresses limitations of other studies at this site, mainly those of Geddis' (1992) work. He used another numerical model, UNSAT2, by Davis and Neuman (1983), to simulate unsaturated flow in the upper unsaturated system (450 ft in depth). His work calls for further study of the system down to the regional aquifer, approximately 1000 ft below, which this study accomplishes. Geddis oriented a two-dimensional grid perpendicular to the canyon axis for simulations and concluded that unsaturated flow perpendicular to the canyon axis under the mesas was minimal. This study orients a two-dimensional grid down the axis of the canyon to incorporate the dip in stratigraphy and assess lateral flow behavior in that direction. An assumption of no dip in the stratigraphy perpendicular to the canyon axis is common in both studies. When setting up the grid in this study the proximity of the Radioactive Waste Liquid Treatment Facility discharge point was taken into consideration as well. Boundary conditions used by Geddis restricted his simulations to time dependent solutions, while the simulations in this study could reach steady state conditions with various recharge scenarios. He modeled a small portion of his upper boundary with both a specified flux and constant head boundary condition; his remaining boundaries were no flow. Although this study uses a specified flux (recharge) along the upper boundary close to that used by Geddis, it also examines recharge at various magnitudes distributed evenly and variably with respect to location. Simulations presented here incorporate the remaining upper boundary with several specified flux conditions; the lower boundary with a specified saturation condition to represent the water table at the regional aquifer; and side boundaries with no flow conditions.

This modeling study addresses these limitations among others, and simulation results are used to specifically:

- Provide estimates of the distribution of pressures, saturations, and liquid flux
- Assess potential pathways taken through the system
- Estimate travel times through the system
- Assess the effects of certain recharge scenarios

2. SITE DESCRIPTION

2.1. LOCATION AND PHYSIOGRAPHY

Los Alamos National Laboratory (LANL) is located in north-central New Mexico, USA, approximately 30 km northwest of Santa Fe between the towns of Los Alamos and White Rock (Figure 1.1).

> "The laboratory site is situated on the Pajarito Plateau, which consists of a series of finger-like mesas separated by deep east-to-west oriented canyons cut by intermittent streams. Mesa tops range in elevation from approximately 2,400 m (7,800 ft) on the flanks of the Jamez Mountains to about 1,900 m (6,200-ft) at the eastern termination above the Rio Grande Canyon."
>
> "Most Laboratory and community developments are confined to mesa tops. The surrounding land is largely undeveloped, with large tracks of land north, west, and south of the laboratory site being held by the Santa Fe National Forest, Bureau of Land Management, Bandelier National Monument, and Los Alamos County. The Pueblo of San Ildefonso borders the Laboratory to the east."
>
> "The laboratory is divided into Technical areas (TA's) that are used for building sites, experimental areas, waste disposal locations, roads, and utility right-of-ways. However, these uses account for only a small part of the total land area. Most land provides buffer areas for security and safety and is held in reserve for future use.
>
> "The Department of Energy controls the area within LANL and has the option to completely restrict access. The public is allowed limited access to certain areas of the laboratory." (Environmental Protection Group, 1994)

Mortandad Canyon, the focus of this study, originates within the boundaries of LANL and extends about 16 km in an easterly direction to the Rio Grande Canyon. The first 7 km of the canyon is on lands belonging to LANL, and the final 9 km is on lands belonging to San Ildefonso Pueblo. The elevation change, along the 1829 m (6000 ft) length of channel in the area of study, is approximately 58 m (283 ft), with the elevation of the western end being 2154 m (7066 ft) and the eastern end being 2096 m (6877 ft).

2.2. CLIMATE

The local climate is described as a "temperate mountain climate" with an average annual precipitation of 47.6 cm that varies greatly with elevation. Summers at LANL tend to begin warm and arid and end with typical daily thunder showers during the later part. Average monthly lows range between 51-55°F, and highs between 77-80°F. Autumns are generally calm, arid, and much cooler. Average monthly lows range between 27-47°F, and highs between 48-71°F. Winter temperatures fluctuate greatly, and snow storms are frequent enough to keep a snow base for a couple of months with average monthly lows ranging between 19-21°F, and highs between 39-43°F. Spring temperatures fluctuate greatly as well and are usually windy and dry. Average monthly lows range between 26-42°F, and highs between 49-67°F.

2.3. VEGETATION

Vegetation within Mortandad Canyon varies by elevation. Upper Mortandad Canyon is densely vegetated with shrubs, pine, fir, Box-Elder, Gambel oak, and

Chokecherry providing the dominant overstory, while the understory consists of forbs and grasses mainly of Bluegrass, Clematis, and Bedstraw (Miera et al., 1977).

2.4. LAND USE

Beginning in June 1963, liquid radioactive waste from the Laboratory was diverted to a new treatment facility located above Mortandad Canyon at Technical Area (TA)-50. Since that time, treated effluents from that facility have been released into the stream bed of Upper Mortandad Canyon. Other LANL sites, such as TA-3's Sigma building and former TA-48 outfalls, release waters to the canyon as well. However, the quality is better and the quantity is smaller than those from TA-50's Radioactive Waste Liquid Treatment Facility. The choice of Upper Mortandad Canyon for an effluent release site was based on several conditions considered favorable which included the following (Purtymun, 1964):

- No perennial streamflow
- The watershed is fairly small
- The depth to the regional aquifer is approximately 300 m
- The volume of the canyon's alluvial sediment on LANL's land is large
- No surface or groundwater flows down canyon past the LANL boundary
- High evapotranspiration rates
- The centralized LANL location
- The remoteness of the location

2.5. PHOTOGRAPHS

The photographs presented here, taken in October of 1996, show several significant aspects of Upper Mortandad Canyon.

The first photograph, Figure 2.1, shows TA-50's Radioactive Waste Liquid Treatment Facility discharge point, which lies in a tributary drainage to Mortandad Canyon. The effluent flows about 40 m to the confluence with Mortandad Canyon, then another 30 m passing a gaging station (GS-1). Discharges are performed once a holding tank becomes full, at which time 78.9 m^3 (20,885 gal) are released at 2.7 m^3/min (720 gal/min). Discharges vary from 4-6 days/week and 2-8 tanks/week. Yearly discharge volumes are approximately 50,000 m^3 (13,206,550 gal) (Water Quality and Hydrology Group, 1996).

The following four photographs, Figures 2.2, 2.3, 2.4, and 2.5 were taken further down canyon within the study area and show the canyon's appearance. Typical canyon geometry is illustrated in Figure 2.2. South-facing canyon walls are often vertical, while north-facing slopes typically have angles between 30° and 60°. Dense vegetation throughout this section of the canyon is depicted in Figure 2.3. Figure 2.4 depicts typical canyon geometry and vegetation. Figure 2.5 depicts the stream channel which is typically a couple of meters in width; the canyon bottom usually ranges between 20 m and 40 m in width.

Figure 2.1 Photograph of effluent discharge point.

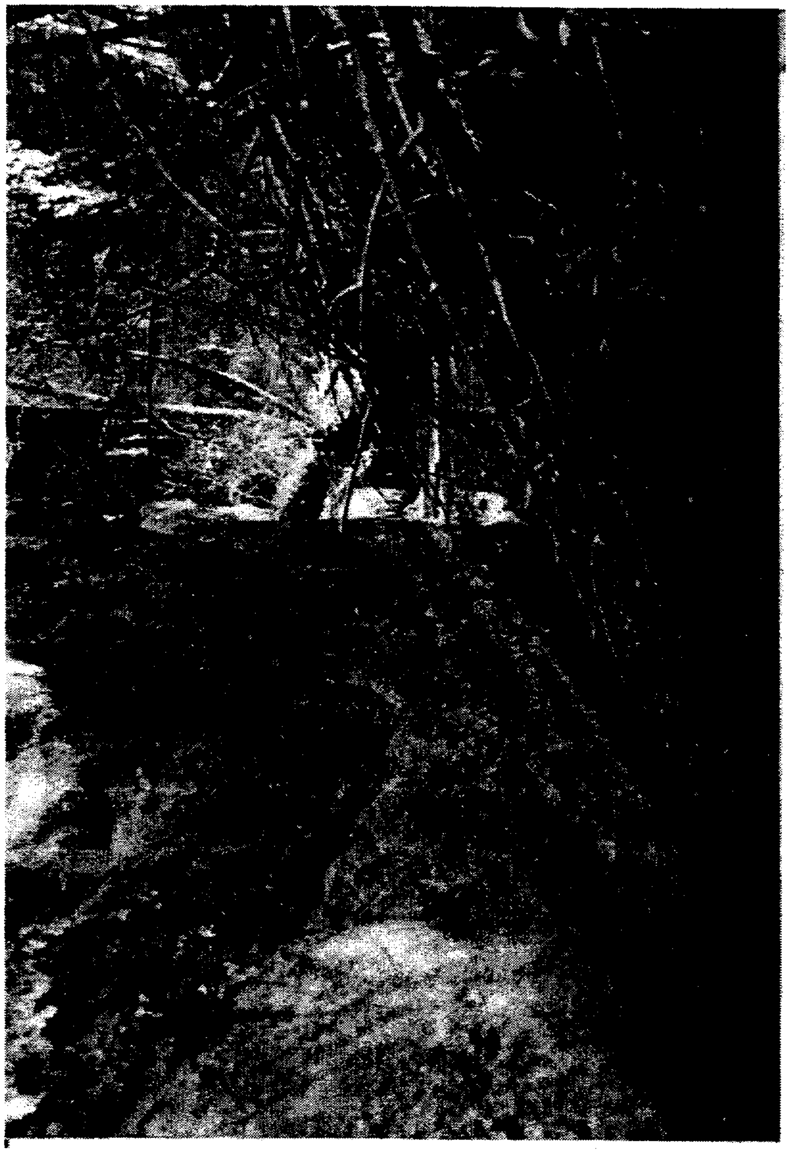

Figure 2.2 Photograph depicting canyon geometry.

Figure 2.3 Photograph depicting canyon vegetation.

Figure 2.4 Photograph of stream channel and canyon bottom.

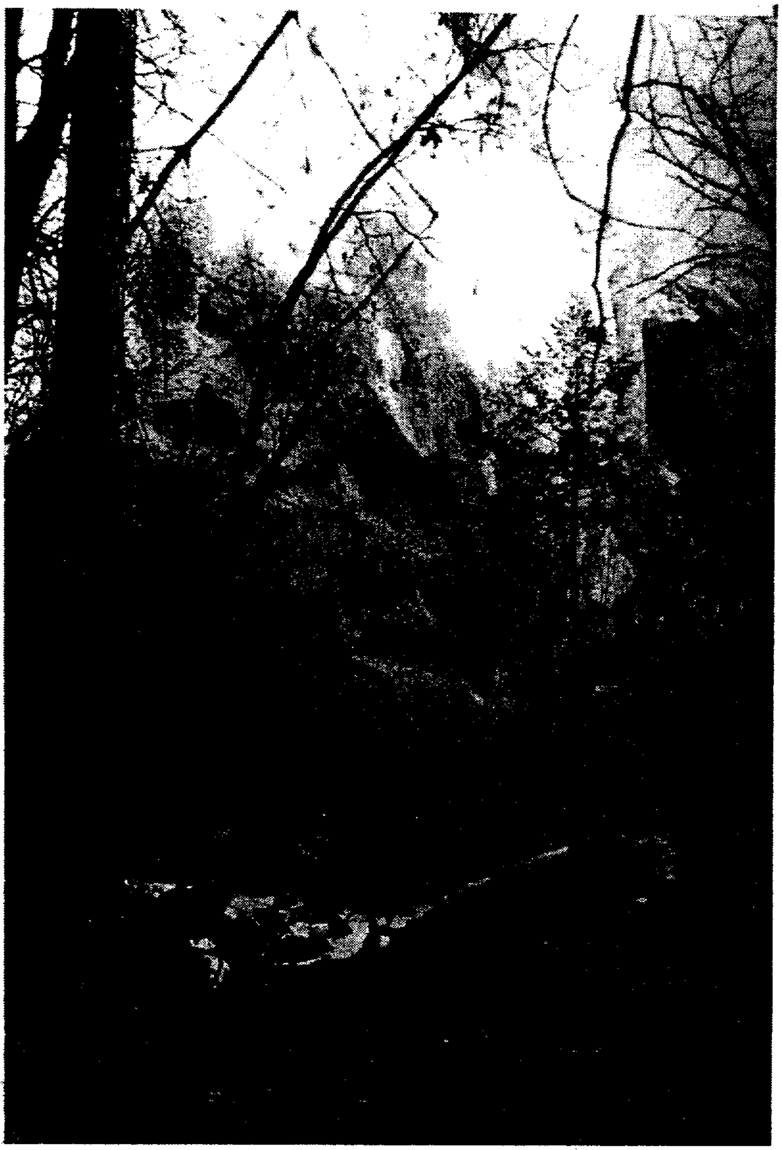

Figure 2.5 Photograph depicting canyon geometry and vegetation.

The final two photographs show the locations of former gaging stations, GS-1 and GS-2, used in water budget calculations (Figures 2.6 and 2.7). GS-1, located on the western end of the study area shown in Figure 2.6. Gaging station-2 was located slightly upstream of the eastern end of the study area, and its location is shown in Figure 2.7. Bank erosion of close to a meter of channel bottom from flooding events is noticeable around the flume in Figure 2.7.

Figure 2.6 Photograph of location of gaging station 1.

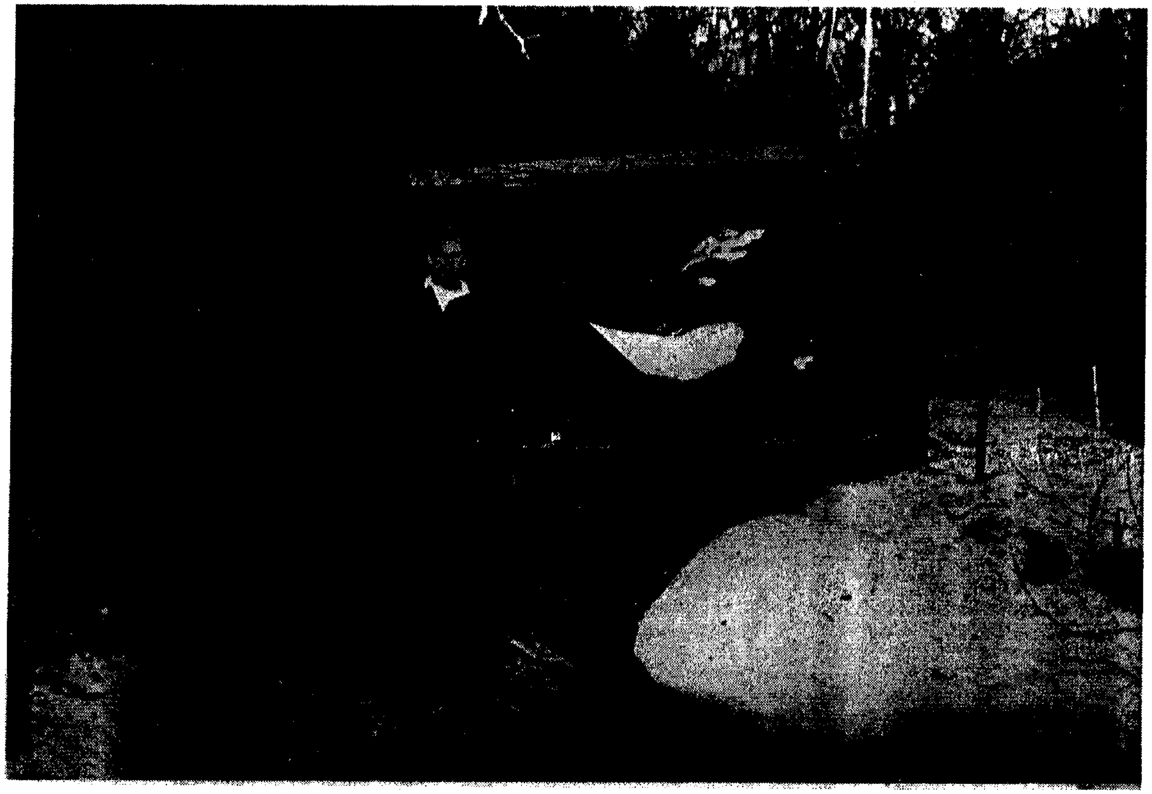

Figure 2.7 Photograph of location of gaging station 2.

3. HYDROGEOLOGY

3.1. GEOLOGIC SETTING

Mortandad Canyon cuts into a sequence of volcanic tuffs (the Bandelier Tuff) deposited between 1.2-1.6 million years ago. The Bandelier Tuff overlies other volcanic and sedimentary rocks deposited between 3-7 million years ago on the Pajarito Plateau. The plateau lies on the southeastern slopes of the Valles Caldera and covers an area about 300 km^2. The Bandelier Tuff blankets deeper sediments along the Rio Grande Rift and Puye Escarpment in places reaching over 1,000 m in thickness. The caldera and surrounding mountains and plateaus were the result of uplift and violent volcanic eruptions. The vertical geologic profile below Mortandad Canyon includes layers of sedimentary rocks interfingered with volcanic flows, layers of tuff, and alluvium.

3.2. GEOLOGIC UNITS

The geology of the canyon is shown in a longitudinal section which runs down the length of the canyon (Figure 3.1). It was produced using well data, subsurface maps, and other geologic cross-sections discussed by Broxton and Reneau (1995 and 1996), Purtymun (1995), and Vaniman et al. (1997). Wells in which geologic logs were used to develop Figure 3.1 are labeled across the upper surface and indicated in a map in Figure 3.2. Descriptions of the eleven units depicted in the figure are presented below. Unit

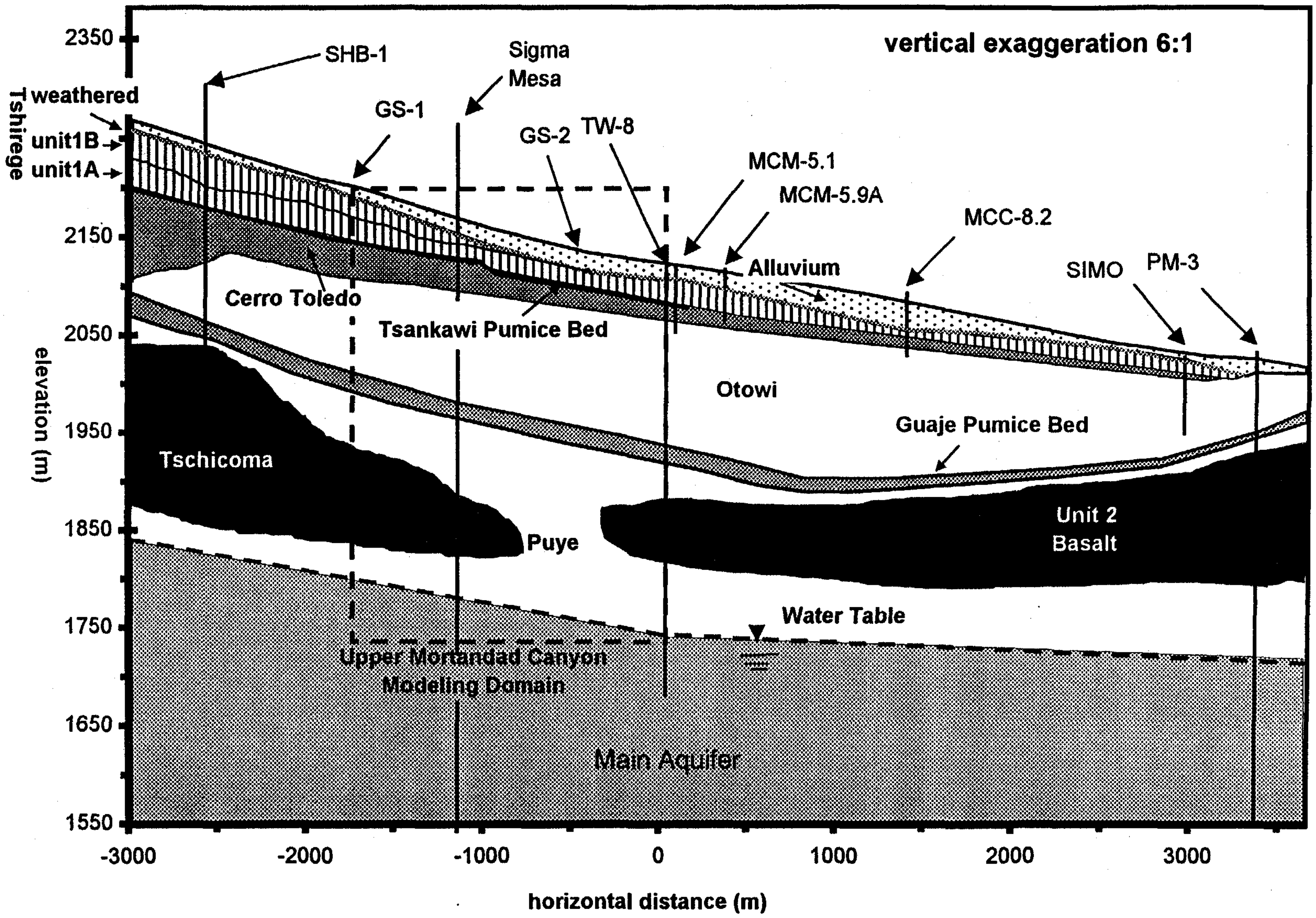

Figure 3.1 Mortandad Canyon stratigraphy.

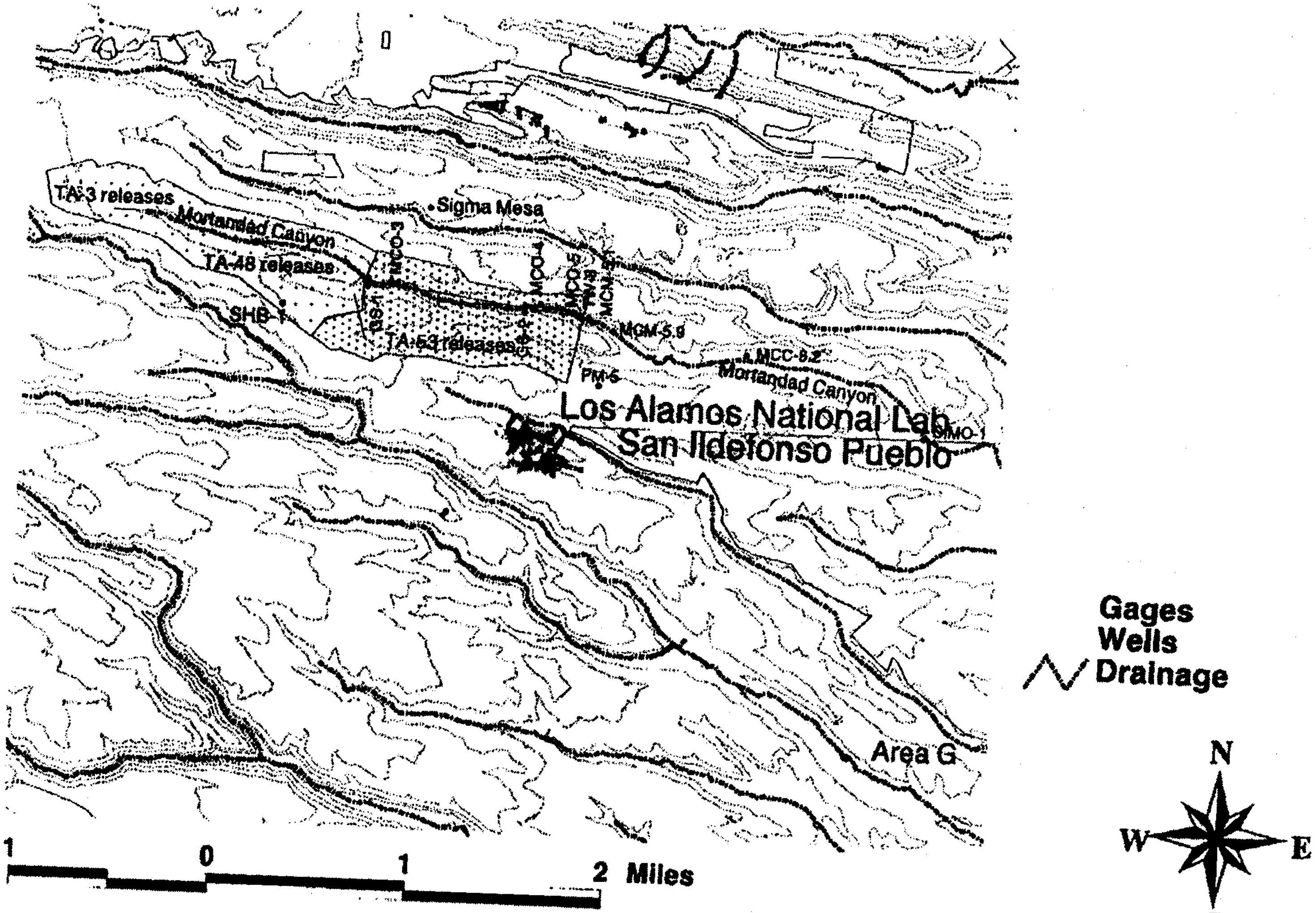

Figure 3.2 Map view of Mortandad Canyon

thickness discussions refer to materials within the modeling domain indicated in Figure 3.1 and are discussed further in section 3.4.

Extending upward from the regional aquifer, between 140 m and 180 m, is the Puye Formation. This formation is composed of several alluvial fan deposits derived from eroded layered dacitic domes of the Tschicoma Formation on the higher slopes of the Valles Caldera. The Puye Formation consisted of poorly consolidated fine- to coarse-grained sand containing larger fragments, some boulders and cobbles in size (Purtymun, 1967).

A later flow of the Tschicoma Formation interfingers with the Puye Formation from the west. The Unit 2 Basalt, which also interfingers with the Puye Formation, is one of several flows from a volcanic field to the east. The horizontal extent of both the Unit 2 Basalt and the Tschicoma Formation is not known, but is suspected to be discontinuous through this portion of the canyon (Broxton and Reneau, 1996). During this study these units are often referred to as volcanics. Thickness of both units ranges between 25 m and 75 m, pinching out abruptly near the center of Upper Mortandad Canyon. Fracturing and jointing in both flows were observed elsewhere at LANL; however, the degree of jointing below Mortandad Canyon is not known. A loss of drilling water during the installation of a deep well (TW)-8 in Mortandad Canyon suggests fractures in the Unit 2 Basalt. The Unit 2 Basalt, Tschicoma, and Puye Formations are all believed to have formed between 3-7 million years ago (Goff, 1989).

Resting unconformably upon the Puye Formation is the Bandelier Tuff, which is a series of volcanic ash-fall and ash-flow deposits. The Bandelier Tuff consists off the lower Otowi Member and the overlying Tshirege Member.

At the base of the Otowi Member is the Guaje Pumice Bed. It is an ash-fall and pumice-fall deposit consisting mainly of rounded fragments of pumice in a glassy ash [illegible]rtymun, 1967). The bed is approximately 10 m thick and was deposited about 1.6 million years ago (Goff, 1989).

The Otowi Member is a homogeneous non-welded pyroclastic flow deposit that was deposited about 1.6 million years ago (Goff, 1989). Below Upper Mortandad Canyon, the formation is about 70 m to 90 m in thickness.

Between the Otowi and Tshirege Members lie sediments of the Cerro Toledo Interval. The Cerro Toledo Interval is a complex sequence of epiclastic sediments and tephras of mixed provenance. It includes well-stratified tuffaceous sandstones and siltstones, primary ash-fall and pumice-fall deposits, and dacite-rich gravel and boulder deposits. Some erosion occurred prior to and following deposition (Purtymun, 1995). The thickness of this unit varies between 15 m and 30 m below Upper Mortandad Canyon.

At the base of the Tshirege Member lies the Tsankawi Pumice Bed. It consists of a thin pumice-fall with some surge deposits and water-laid material in an ash matrix (Purtymun, 1967). Deposition of the bed occurred about 1.2 million years ago (Goff, 1989). The bed is less than 1 m thick and is sometimes confused with the Cerro Toledo

Interval. For this study, the two units are combined and modeled as one and given the properties of the Cerro Toledo Interval.

The Tshirege Member, deposited about 1.2 million years ago, consists of several distinct ash-flows with varying degrees of welding and the Tsankawi Pumice Bed (Goff, 1989).

Unit 1A of the Tshirege Member is composed of fragments of pumice between 1/8 and 6 inches in diameter with fine glassy ash filling the spaces between (Purtymun, 1967). The unit is about 12 m in thickness.

Unit 1B of the Tshirege Member is similar to Unit 1A with somewhat smaller fragments. This unit pinches out beneath Upper Mortandad Canyon and is about 20 m in thickness at the western end of the canyon.

The weathered Units 1A and 1B of the Tshirege Member consist of a thin layer, between 2 m and 4 m in thickness, of variably weathered tuff. The weathered units are difficult to distinguish from the alluvium deposited above and the unweathered bed-rock below. Characteristics are similar to the unweathered tuff below, either Unit 1A or 1B, depending on location in the canyon (Rogers and Gallaher, 1995).

Alluvium is the surface deposit between 2 m and 11 m in thickness. Composition of alluvium varies from coarse-grained pebbly to a sandy-silty clay. Particle size distribution results of composite samples from a several locations in the upper canyon show less than 10% by weight was less than 500μ in size (Purtymun, 1975).

3.3. MATERIAL PROPERTIES

Physical and unsaturated properties for the Bandelier Tuff are taken from Rogers and Gallaher (1995). They compiled data from hundreds of core measurements from 21 boreholes throughout LANL with more than seventy collected around Mortandad Canyon. Data from laboratory pressure plate (SPOC, submersible pressure outflow cell) and psychrometer measurements were used to determine moisture retention curves (Rogers and Gallaher, 1995). Saturated moisture contents θ_{sat}, residual moisture contents θ_r, saturated hydraulic conductivity K_{sat}, and bulk densities ρ were determined by Stephens et al. (1991a,b) from core samples. Common laboratory methods for bulk density ρ and porosity ϕ measurements were used. Van Genuchten's curve fitting parameters α, N, and m were obtained by Rogers and Gallaher (1995) using the program RETC (van Genuchten et al., 1991). The mean values for material properties obtained from these cores and curves were used as model input to solve the flow equations presented in section 4.2.

Physical and unsaturated properties of the Guaje Pumice Bed come from similar analyses of a single core sample taken several km to the south-east of the canyon (Birdsell et al., 1997).

Physical and unsaturated properties of the Puye Formation are not known, and values from modeling done for Area G by Birdsell et al. (1997) were used. Estimated values from that study are similar to that of a coarse sand with decreased porosity to account for the larger materials in the conglomerate (Birdsell et al., 1997).

The physical and unsaturated properties of the Unit 2 Basalt and the Tschicoma Formation are not known, and values from modeling done for Area G were used (Birdsell et al., 1997). An equivalent porous media approach was used to evaluate flow through these fractured units. That is, no discrete fractures were included, and a single weighted average of the matrix and fracture van Genuchten parameters was assumed to be applicable. Matrix properties used for both units were from a similar basalt formation at Idaho National Engineering Laboratory (INEL) (Bishop, 1991). The fracture properties used were the same as those suggested as a conservative estimate for the basalt by Birdsell et al., (1997).

Moisture characteristic curves for each material are presented in Figure 3.3A, with moisture contents plotted against matric suctions in cm. Values were calculated using the following relationship, presented by van Genuchten (1980) as;

$$\theta(p_{cap}) = \frac{\theta_{sat} - \theta_r}{[1 + |\alpha \, p_{cap}|^N]^m} + \theta_r \,, \qquad [1]$$

where $\theta(p_{cap})$ is the volumetric moisture content as a function of capillary pressure head. The other terms, θ_{sat} saturated moisture content (also porosity) [unitless], θ_r residual moisture content [unitless], and the experimentally determined van Genuchten parameters α, m, and N, were derived from core samples discussed above. In Figure 3.3A Puye and (matrix) Basalt's maximum or saturated moisture contents $\theta_{sat,}$ are considerably less than

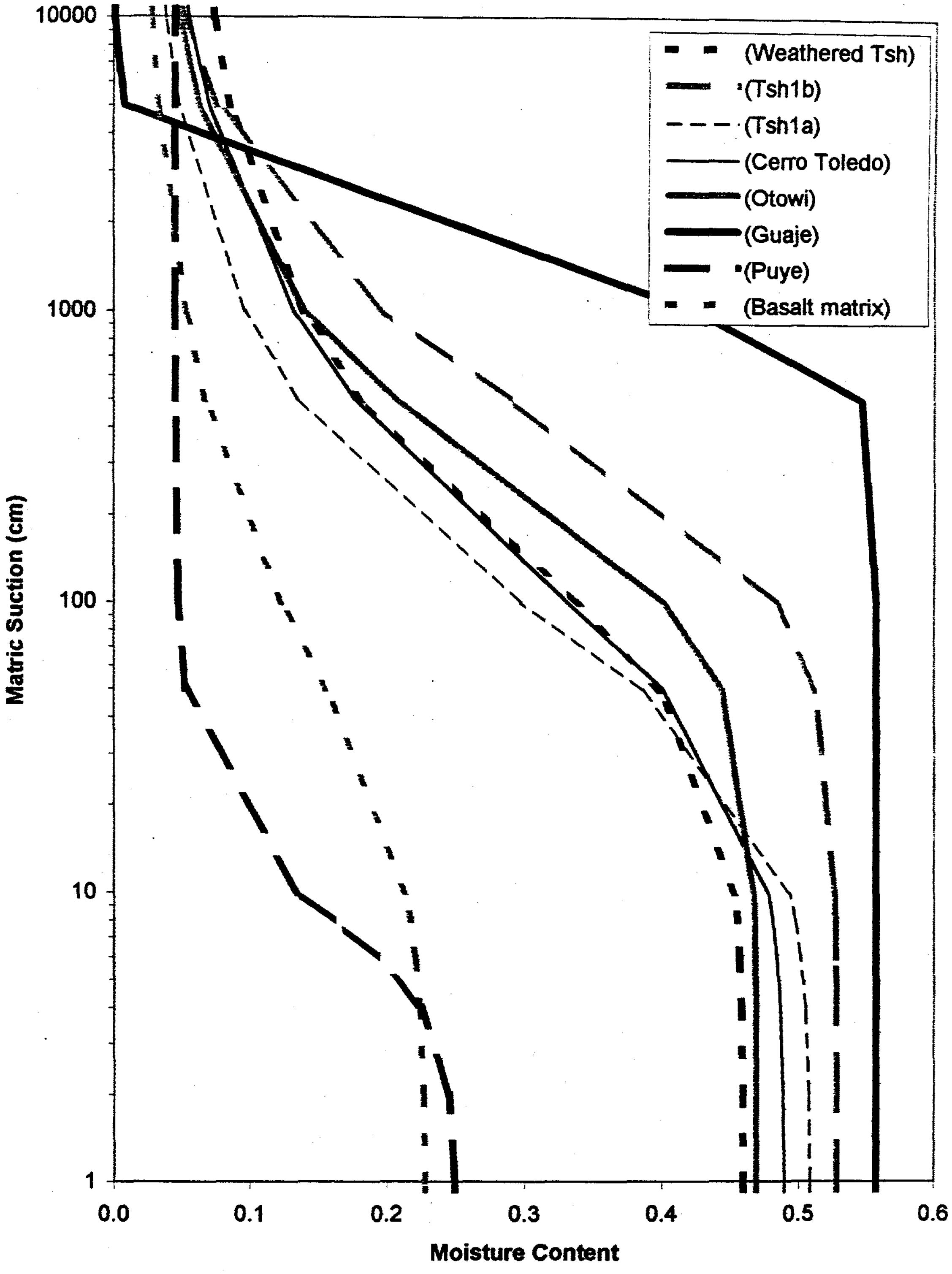

Figure 3.3A Characteristic curves. Note matric suction in cm and zero is atmospheric.

the other materials. This is mainly due to the low permeabilities of these units and is discussed later.

Similar curves are also presented in terms used during the modeling in this study in Figure 3.3B. Saturation S is plotted against matric suction in Mpa where zero is atmospheric pressure head. Moisture content θ was converted to saturation S by dividing by porosity ϕ of each material as in the relationship [all unitless]:

$$S = \theta / \phi \qquad [2]$$

In Figure 3.3B the Puye and Guaje curves have much steeper slopes than the remaining materials. This shows that pores spaces to release or gain water within a smaller range of matric suctions than the other materials. The van Genuchten parameters m and N that were derived for these materials indicate the steeper slopes seen in these curves. Also noticeable in this figure is the matric suctions required for these two materials to release water (air entry pressure) differs from the other materials. The Puye Formation requires very little matric suction to release pore water while the Guaje requires a larger matric suction for the same purpose. For the Guaje Pumice bed, matric suctions less than these values do not change saturations. Differences in these curves become important during flow simulations.

Hydraulic conductivity K, is plotted against moisture content in Figure 3.4 and was determined by the relationships presented by van Genuchten (1980) as:

$$K(S) = K_{sat}\, k_r \qquad [3]$$

$$k_r = S_e^{1/2} \left[1 - \left(1 - S_e^{1/m} \right)^m \right]^2 \qquad [4]$$

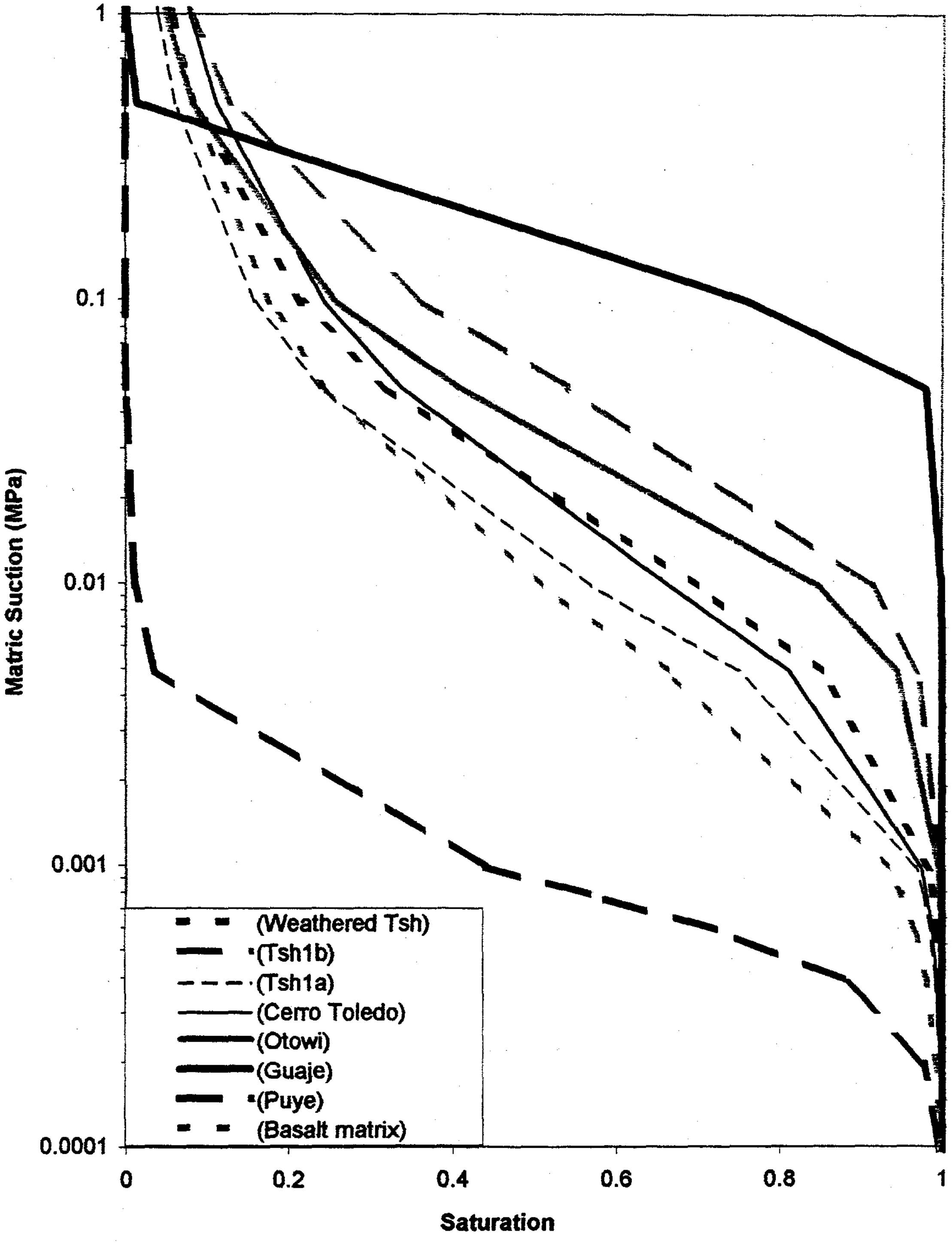

Figure 3.3B Characteristic curves. Note matric suction in MPa units where zero is atmospheric.

$$S_e = (S_l - S_{lr}) / (1 - S_{lr}) \qquad [5]$$

Where k_r is the relative permeability determined from Equation [4], and K_{sat} is the saturated hydraulic conductivity determined from well cores. The term S_e is the effective saturation determined from other saturation values S_l liquid saturation, S_{lr} residual liquid saturation, and S_{lmax} the maximum liquid saturation which equals 1. Saturation values are unitless and were converted from moisture contents using Equation [2]. The Puye and Basalt (matrix) units stand out from other materials with higher and lower hydraulic conductivity, respectively. Fractured basalt properties were not plotted because conductivities were well out of range.

Porosity and saturated permeability k_{sat} are plotted against depth in Figure 3.5. The Guaje and Basalt properties stand out from the others. Plots for the fracture properties of the Basalt show high permeability and low porosity; and plots for the matrix properties of the Basalt are low for both permeability and porosity. Although an effective continuum approach (weighted average between matrix and fracture properties discussed in section 4.3) is used to simulate these materials, these values are later shown to have a great effect on the flow and particle tracking solutions.

Specific values of each material used to develop the curves above and as model input are indicated in Table 3.1, with the addition of bulk density ρ [M/L^3].

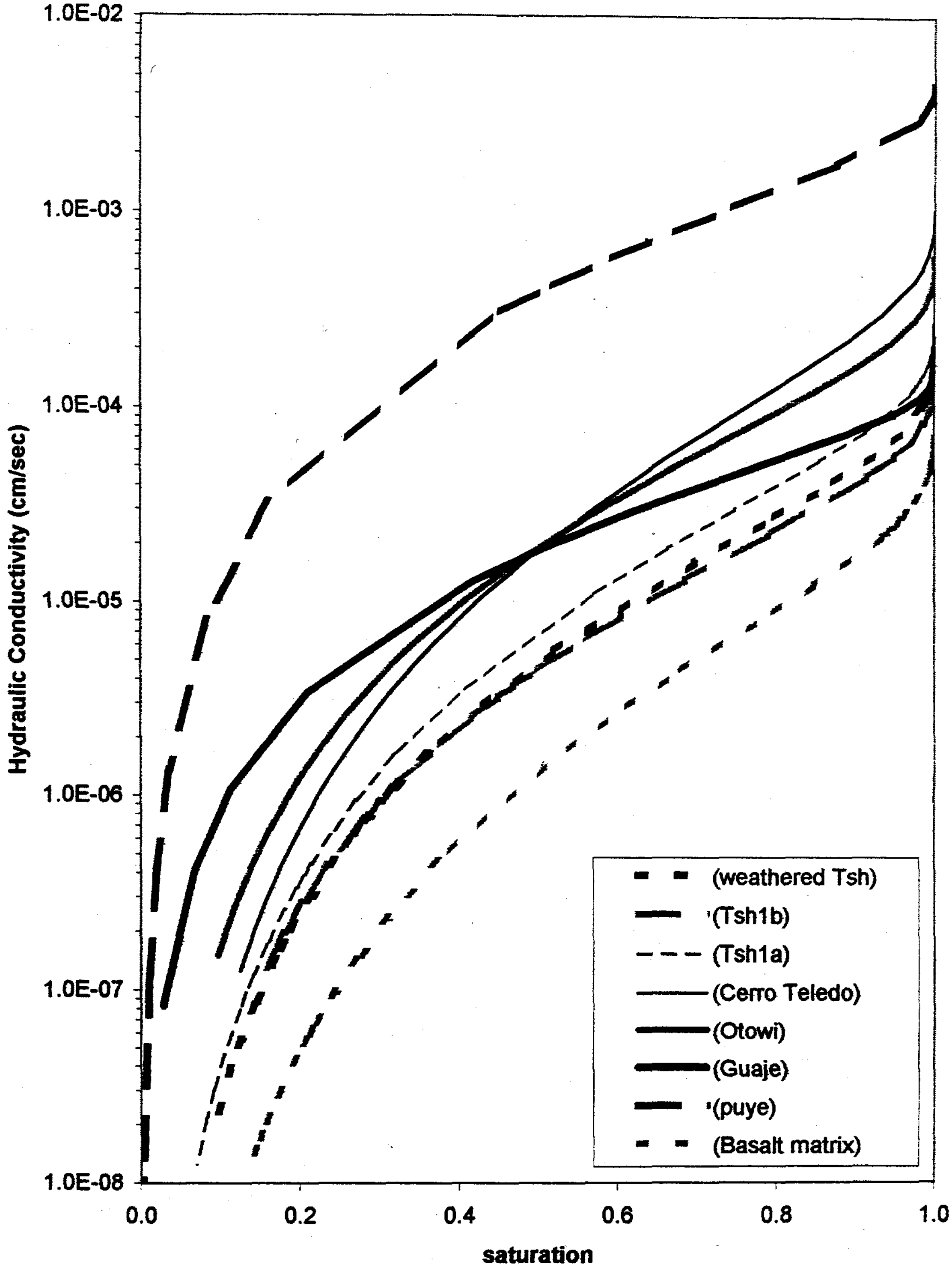

Figure 3.4 Hydraulic Conductivity curves.

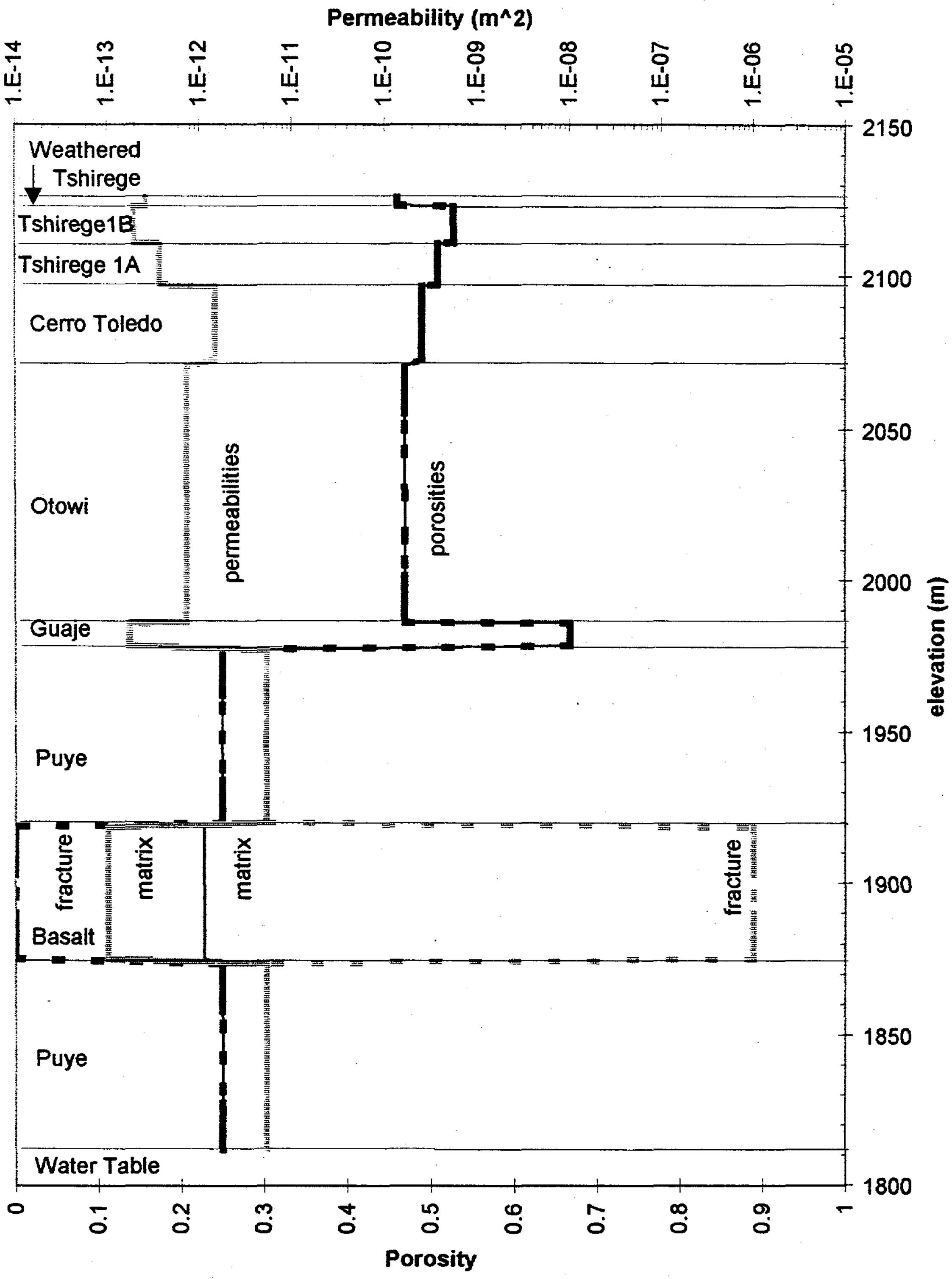

Figure 3.5 Porosity and saturated permeability depth profiles.

Table 3.1 Material Properties.

	α	N	M	θsat	θres	Ksat	ϕ	perm	ρ
Weathered Tshirege	0.00014	1.5830	0.3683	0.4600	0.051	0.20	0.46	2.65E-13	1260
Tshirege Unit 1b	0.00004	1.6600	0.3976	0.5280	0.009	0.15	0.528	1.96E-13	1180
Tshirege Unit 1a	0.00022	1.5920	0.3719	0.5090	0.018	0.28	0.509	3.68E-13	1160
Cerro Toledo Interval	0.00019	1.4810	0.3248	0.4900	0.017	1.12	0.49	1.50E-12	1250
Otowi Formation	0.00007	1.7110	0.4155	0.4690	0.026	0.54	0.469	7.25E-13	1180
Guaje Pumice Bed	0.00001	4.0264	0.7516	0.5570	0.000	0.13	0.667	1.73E-13	810
Puye Formation	0.00145	2.6800	0.6269	0.2500	0.045	4.00	0.25	5.32E-12	1200
Volcanics matrix	0.00038	1.4740	0.3216	0.2280	0.015	0.08	0.228	1.00E-13	1200
Volcanics fracture	0.00038	1.4740	0.3216	0.0001	0.000	838080	0.0001	1.00E-06	1200
Puye Formation	0.00145	2.6800	0.6269	0.2500	0.045	4.00	0.25	5.32E-12	1200
units	m^-1	unitless	unitless	unitless	unitless	m/day	unitless	m^2	kg/m^3

3.4. HYDROGEOLOGIC LONGITUDINAL SECTION

A subsection of the domain shown in Figure 3.1 is used for simulation purposes and is presented in Figure 3.6. The method by which the lithologic contact depths throughout the modeling domain were produced is now described. Contacts were represented by lines connecting the contacts observed in wells. Some slight adjustments were made using the most reliable well data when contact points did not line up exactly. The location of each well discussed below is shown in a map of the area in Figure 3.2. Most of those wells are also shown as projections to the stratigraphy indicating well depths in Figure 3.1. Deep wells extending through the Bandelier Tuff consisted of TW-8 within the Mortandad Canyon; and Sigma Mesa, 35-2028, SHB-1, PM-3, and PM-5 each outside the canyon but nearby. Several intermediate wells within the canyon penetrate through the Tshirege Units: They include MCM-5.1, MCM-5.9A, MCC-8.2, and SIMO. Shallow wells terminating above or just below the alluvium-tuff interface include, MCO-3, 4, 4.9, and 5.

(A) Water Table- The water level at the time of completion of Test Well (TW)-8 was used as one contact point. Wells PM-3, PM-5, SHB-1, and Sigma Mesa were used to determine the slope of the regional aquifer surface passing through TW-8. The slope of the regional water table within the area modeled is 0.011 dipping east.

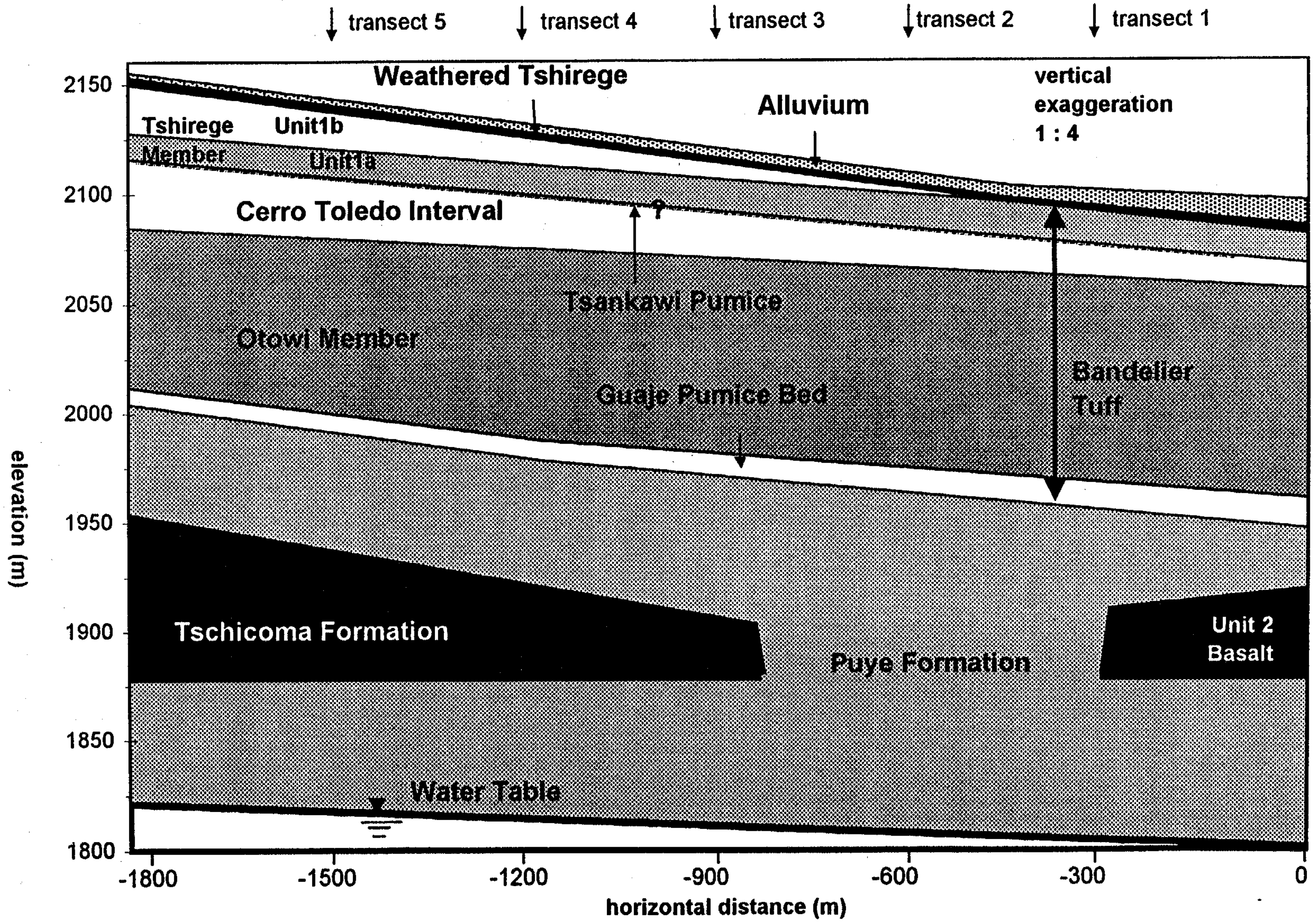

Figure 3.6 Stratigraphy of Upper Mortandad Canyon model domain.

(B) Puye Formation- Data from wells SHB-1, Sigma Mesa, and TW-8 were used to determine the upper contact of this unit. The lower contact was not used, because the water table lies within this unit. The unit is interfingered by the volcanic flows discussed below.

(C) Unit 2 Basalt- Data from wells TW-8 and PM-3 were used to determine the upper and lower contacts for the basalt. The basalt flow is shown interbedded with the Puye Formation. It is not known how far west this unit extends. It is assumed to stop before it contacts the Tschicoma flow to the west.

(D) Tschicoma Formation- Data from wells Sigma Mesa and SHB-1 were used to determine the upper and lower contact of the Tschicoma Formation. This flow is shown interbedded with the Puye Formation. It is not known how far east this unit extends. It is assumed to stop before it contacts the Unit 2 Basalts to the east.

(E) Guaje Pumice Bed- Data from wells SHB-1, Sigma Mesa, PM-3, and TW-8 were used to determine the upper and lower contact of this unit.

(F) Otowi Member- Data from wells SHB-1, 35-2028, and MCC-8.2 were used to determine the upper contact of this unit. Data from wells SHB-1, Sigma Mesa, and TW-8 were used to determine the lower contact of this unit.

(G) Cerro Toledo/Tsankawi Pumice Bed- These two units are treated as a single unit labeled the Cerro Toledo. This was done because the Tsankawi was not distinguished from the Cerro Toledo in most wells. Logs from wells SHB-1, 35-2028, MCM-5.1, MCM-5.9A, MCC-8.2, SIMO, and PM-3 were used to determine the upper contact of this unit. Logs from wells SHB-1, 35-2028, and MCC-8.2 were used to determine the lower contact of this unit.

(H) Unit 1A and Unit 1B of the Tshirege Member- Logs from wells SHB-1, 35-2028, Sigma Mesa, TW-8, MCM-5.1, MCM-5.9A, MCC-8.2, SIMO, and PM-3 were used to determine the lower contact of Unit 1A and the upper contact of Unit 1B. An outcropping near GS-2 of a very thin vapor phase notch (Unit 1A/Unit 1B contact) projects westward parallel to the Unit 1A lower contact line, thus dividing the two units. Material properties of the vapor phase notch are not known and are not represented in the model.

(I) Weathered Unit of the Tshirege Member- Logs from wells MCO-3, 4, and 4.9 were used to determine the upper and lower contacts of this unit.

(J) Alluvium- Known surface elevations along the cross-section were taken from GS-1 and 2; MCO-3, 4, 4.9, and 5; and TW-8. Logs from these MCO wells were used to determine the lower contact. The alluvium is included in the longitudinal section; however, it is not modeled as it lies outside the modeling domain.

3.5. HYDROLOGY

3.5.1. Surface Water

Stream flow in the canyon consists of a stretch of intermittent flow within Upper Mortandad Canyon. The stream flow is supplied by effluents, snow melt, and storm runoff. The extent of surface flow changes continuously; however, flow is only observed beyond Upper Mortandad Canyon during short periods of heavy runoff. Downstream from Upper Mortandad Canyon, the alluvium thickens and the canyon widens, creating a less favorable setting for surface flow. A more detailed account of the behavior of the stream is found in work by Stoker (1991) and Purtymun (1964).

Gaging stations GS-1 and GS-2 are approximately 1200 m apart in Upper Mortandad Canyon (Figure 3.6). Although much flow data exist from GS-1 over the past 35 years, GS-2 flow data are limited to a period from March 1962 through June 1965 (Purtymun, 1967). Flow data from these two stations were part of the water budget used in this study, and are discussed below.

3.5.2. Groundwater

A small perched groundwater zone exists within the alluvium deposited along the canyon bottom. The alluvium within Upper Mortandad Canyon increases in thickness with distance downstream, from 0 m to 12 m. The thickness of the perched groundwater at the base of the alluvium also increases with distance downstream, usually between 0 m and 6 m. The depth from the surface to that perched groundwater increases with distance downstream as well, usually between 0 m and 7 m. The thickness of, and depth to, the perched groundwater both change with time. The width of this perched groundwater system relates to the width of the canyon and the concave shape of the alluvium-rock interface below, usually between 20 m to 40 m. This perched groundwater system does not extend to the LANL boundary about 4 km down stream from Upper Mortandad Canyon.

The regional aquifer is approximately 300 m below the perched alluvial groundwater system and is used for municipal and LANL water supply. Most of the intervening rock between the alluvial groundwater and regional aquifer is unsaturated. Many wells exist in the canyon; however, few extend beyond a few feet into the bedrock.

3.6. WATER BUDGET

Purtymun (1967) developed a water budget for the shallow alluvial groundwater system in Mortandad Canyon. He provided an estimated of water loss from the alluvium into the unsaturated system below. The budget used 1963-1966 surface flow data, stream gradients, hydraulic conductivity of the alluvium, alluvial groundwater volume, and an estimate of evapotranspiration (Purtymun, 1967). The main components of the budget are shown in a schematic which includes the governing equation (Figure 3.7). A list of these components and the equations used to calculate monthly values of each are as follows:

- Surface water (gain) was determined from the difference in surface flows measured at GS-1 and GS-2, representing surface water in and surface water out respectively.

  Surface water gain = Surface water in - Surface water out

Most of the surface water entering the upper canyon is lost by infiltration into the alluvium prior to leaving this section of the canyon. Precipitation volume was assumed to be accounted for by the surface water in and out terms.

- Underflow (loss) or horizontal groundwater flow <u>out</u> of alluvium was estimated using Darcy's law:

$$Q = -K\,(\Delta h/\Delta L)\,A \qquad [6]$$

where:

Q is the horizontal outflow rate $[L^3/T]$

$\Delta h/\Delta L$ is the watertable gradient [unitless]

A is the cross sectional area of alluvium $[L^2]$

K is the alluvium hydraulic conductivity of 244.8 m/d $[L/T]$ or 6000gpd/ft^2, the method and exact location are unknown.

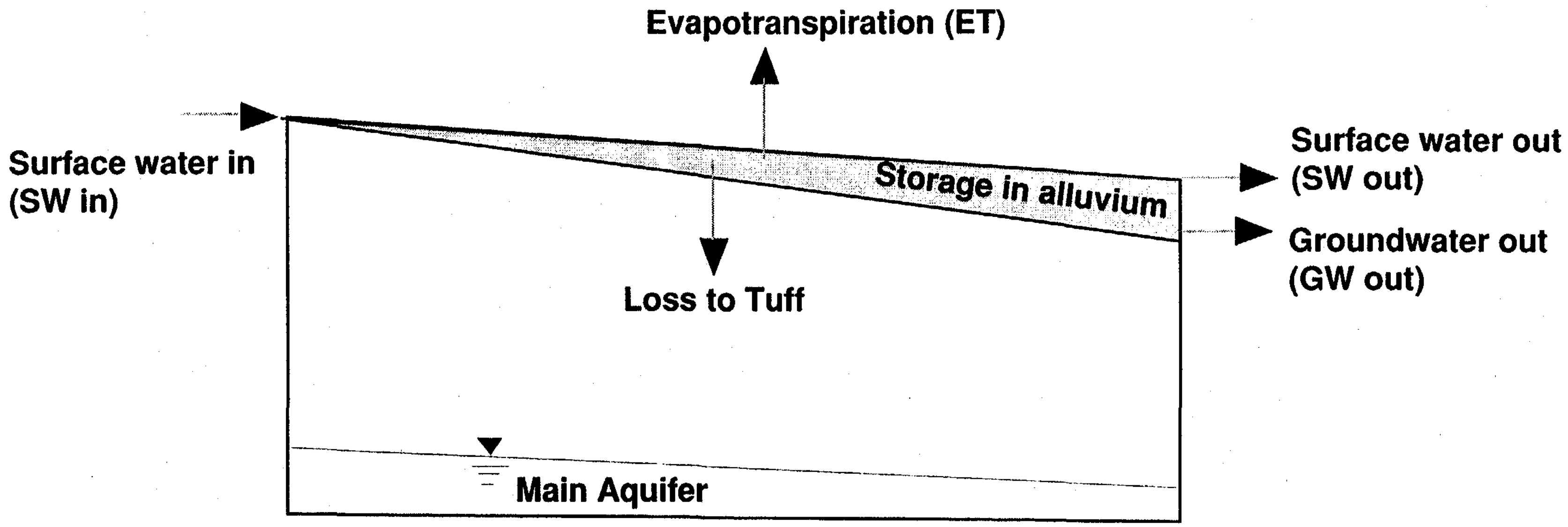

$$\triangle \text{Storage} = \text{input} - \text{output}$$

$$\triangle \text{Storage} = (\text{SW in}) - (\text{SW out} + \text{GW out} + \text{ET} + \text{Loss})$$

$$\text{Loss} = (\text{SW in} - \text{SW out}) - \triangle \text{Storage} - \text{GW out} - \text{ET}$$

Figure 3.7 Water budget for Upper Mortandad Canyon surface and alluvial groundwater.

Groundwater flow <u>into</u> Upper Mortandad Canyon or underflow (gain) is very small and assumed to be zero due to the absence of alluvium at the upper end of the modeling domain.

- Evapotranspiration (loss) was applied only to the upper canyon because of its lush vegetation. Purtymun (1967) estimated potential evapotranspiration (PE) using a modified set of Thornthwaite's equations (Hantush, 1959). Estimates were calculated as follows:

$$i = (T_m / 5)^{1.514} \qquad [7]$$

$$I = \sum_{n=1}^{12} i_n \qquad [8]$$

$$a = [6.75 \times 10^{-7}]I^3 - [7.71 \times 10^{-5}]I^2 + [1.79 \times 10^{-2}]I + 0.49 \qquad [9]$$

$$UPE = 1.6\,(10T/I)^a \qquad [10]$$

$$PE = (b/30)UPE \qquad [11]$$

where:

T_m is the mean monthly temperature in °C.

i is the monthly heat index which is a function of T_m in table 3 in (Hantush, 1959).

i_n is the value of I for any particular month.

I is the heat index which is the sum of the 12 monthly index values of I.

a is an empirical exponent that depends on I from table.

T is the mean temperature during any chosen period in °C.

UPE is the monthly unadjusted potential evapotranspiration in cm.

PE is the monthly potential evapotranspiration in cm.

b is an adjustment factor giving the duration of sunshine for the month and latitude expressed in terms of a 12-hour day.

- Δ Storage (gain or loss) in the shallow alluvial groundwater system determined from porosity and groundwater volume using water level measurements.

These components were used by Purtymun (1967) in the governing equation in Figure 3.7 to determine the loss to tuff used for the upper boundary condition in this study. Data from his calculations are shown in Table 3.2 and plotted in Figure 3.8. In the winter of '63-'64 the gaging station froze; therefore, no surface flow data was available. The data shows seasonal variations in water gained from the surface. Furthermore, that water gain from the surface is roughly inversely proportional to the water loss to the tuff.

Table 3.2 Water Budget for Upper Mortandad Canyon. Values are for volumes in m^3, area in m^2, and rate in m/yr.

	surface water (in - out)	change in storage	lateral groundwater flow (in - out)	evapotranspiration	recharge		
month	gain	gain or loss	loss	loss	loss		
Jul-63	11045.2	4331.9	-907.2	-1738.8	-6392.0		
Aug-63	7975.8	2007.2	-971.5	-1379.7	-7057.3		
Sep-63	6879.6	-1432.6	-608.6	-1096.2	-6535.6		
Oct-63	5322.2	-1360.8	-396.9	-850.5	-4725.0		
Nov-63	5133.2	-650.2	-302.4	-207.9	-4770.4		
Dec-63	0.0	-147.4	-525.4	0.0	0.0		
Jan-64	0.0	-635.0	-211.7	0.0	0.0	total recharge volume	
Feb-64	0.0	90.7	-238.1	0.0	0.0	121258	
Mar-64	0.0	438.5	-990.4	-75.6	0.0		
Apr-64	4010.6	1175.6	-767.3	-378.0	-2230.2	recharge volume/year	
May-64	5344.9	635.0	-1156.7	-982.8	-2649.8	60629	
Jun-64	8168.6	555.7	-1409.9	-1398.6	-2071.4		
Jul-64	5360.0	3288.6	-1470.4	-1701.0	-2336.0	surface area	
Aug-64	4993.4	-147.4	-722.0	-1474.2	-7295.4	13290	
Sep-64	4883.8	-4498.2	-313.7	-1020.6	-5239.1		
Oct-64	4532.2	-1689.7	-241.9	-680.4	-3761.1	recharge rate/year	
Nov-64	8380.3	-151.2	-374.2	-132.3	-5428.1	4.562	
Dec-64	9741.1	2445.7	-903.4	0.0	-6902.3		
Jan-65	11340.0	1935.4	-1655.6	0.0	-7881.3		
Feb-65	9828.0	1803.1	-1670.8	0.0	-8969.9		
Mar-65	9450.0	-812.7	-1447.7	-75.6	-7200.9		
Apr-65	10092.6	725.8	-1791.7	-378.0	-8739.4		
May-65	11472.3	-816.5	-1372.1	-945.0	-10965.8		
Jun-65	10931.8	-1810.6	-820.3	-1360.8	-10107.7		

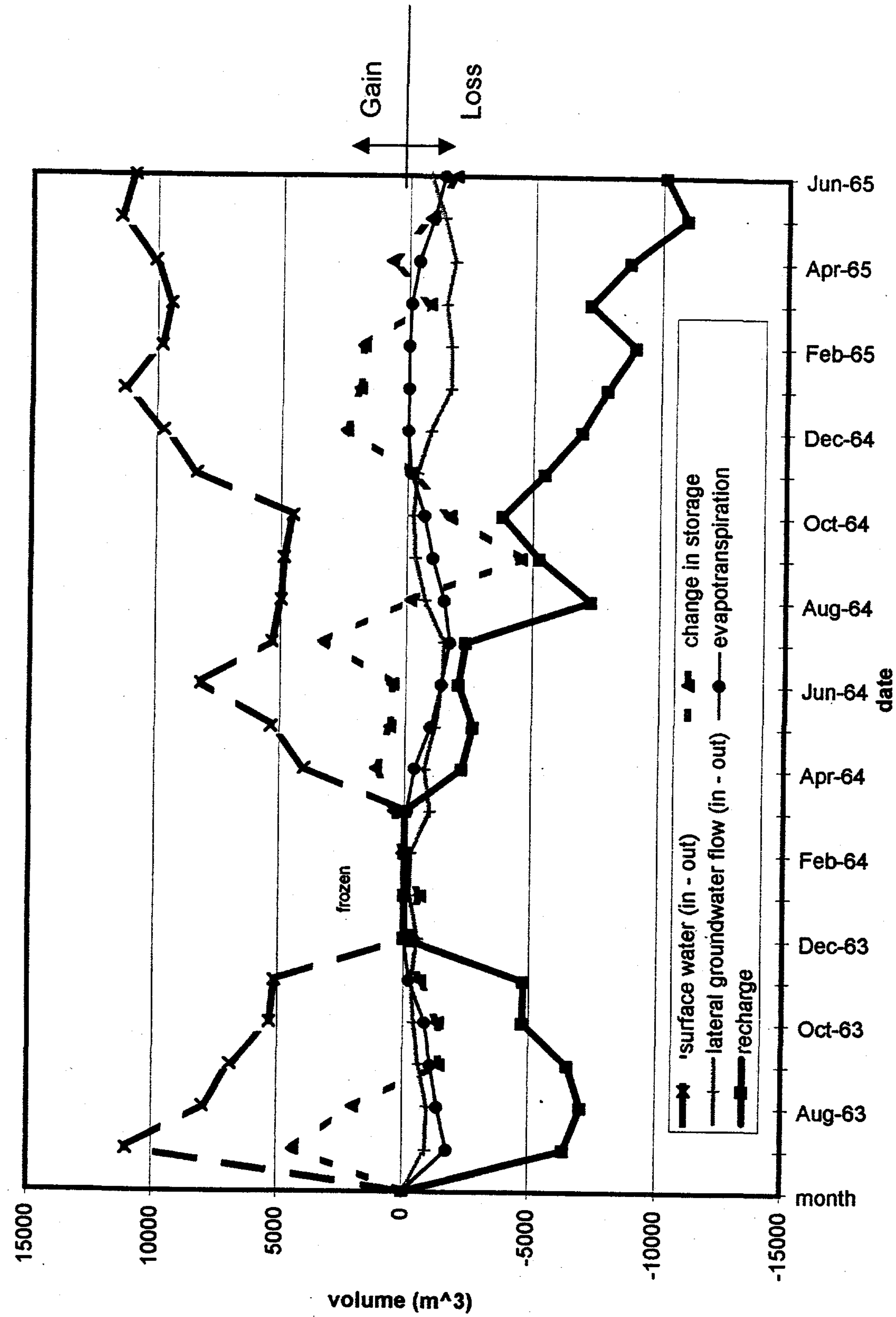

Figure 3.8 Water Budget plot of Upper Mortandad Canyon.

4. NUMERICAL FLOW MODEL

4.1. INTRODUCTION

The computer code and equations used for modeling unsaturated flow and transport in Mortandad Canyon are described here, in addition to the code options implemented. This is followed by discussions of the boundary conditions used and how the finite element grids were created.

4.2. SIMULATION CODE

The Finite Element Heat and Mass Transfer code (FEHM) is a numerical code developed at LANL to simulate subsurface flow and transport processes (Zyvoloski et al., 1994a and b). In this study, the code used a two-dimensional, isothermal, saturated/unsaturated system to model flow. The equation solved was the air-water-isothermal flow equation for water mass. A simplified form of this equation is the conservation of mass equation which is solved in a series of controlled volume finite element cells:

$$\partial A_m/\partial t + |\overline{\nabla} \bullet \mathbf{f}_m| + q_m = 0 \qquad , \qquad [12]$$

where $\partial A_m/\partial t$ is the change in storage of liquid mass per unit volume with time [M/L^{3}t], $\overline{\nabla} \bullet \mathbf{f}_m$ is the net liquid mass flux [M/L^{3}t], and q_m is the liquid mass source (or sink) [M/L^{3}t].

The first mass balance component, A_m accumulation of liquid mass [M/L^3], is the product of material porosity ϕ [unitless], liquid saturation S_l [unitless], and density of the liquid ρ_l [M/L^3] given by Corey (1994) as:

$$A_m = \phi (S_l \rho_l) \qquad [13]$$

The liquid saturation S_l is determined using the following relationship, presented by van Genuchten (1980) as:

$$S_e(p_{cap}) = \frac{1}{[1 + |\alpha p_{cap}|^N]^m} \quad , \qquad [14]$$

also written in the form FEHM uses (Zyvoloski et al., 1994b):

$$P_{capl} = (1/\alpha)[S_e^{-1/\lambda} - 1.0]^{1.0 - \lambda} \qquad [15]$$

The air entry pressure α [1/L], and N [unitless] are each experimentally determined van Genuchten parameters for each material modeled. The terms λ and m are related to N by:

$$\lambda = m = 1 - (1/N) \qquad [16]$$

The residual liquid saturation S_{lr}, and maximum liquid saturation S_{lmax} which equals 1.0 and does not include entrapped air, are both known for each material [unitless]. The primary variable capillary pressure head p_{cap} [L], is solved for by the code using a Newton-Raphson technique discussed at the end of this section.

The second mass balance component, $\mathbf{f}_m$ liquid mass flux [M/L^2t], is the product of the density of the liquid and Darcy flux $\bar{v}$ [L/t]:

$$\mathbf{f}_m = \rho_l \bar{v}_l \qquad [17]$$

Liquid velocity is determined by Darcy's law, where gravitational and capillary forces are separated. The relationship is given by Corey (1994) as:

$$\bar{v}_l = (-kk_r / \mu_l)(\bar{\nabla} P_l - \rho_l \bar{g}) \qquad [18]$$

Where k is intrinsic permeability of each material [L^2], k_r is the relative permeability of each material [unitless], μ_l is the fluid viscosity [M/Lt], P_l is the pressure of the liquid [$M/L\,t^2$], and $\bar{g}$ is the acceleration due to gravity [L/t^2]. The relative permeability of each material is determined from a relationship given by van Genuchten (1980) in equation [4] and expressed by Zyvoloski (1994) in the manual as:

$$k_r = [1.0 - (1.0 - S_e^{1/\lambda})^{\lambda}]^2 S_e^{1/2}, \qquad S_e < S_{lmax} \qquad [19]$$

The third mass balance component, q_m liquid mass [$M/L^3\,t$] source (or sink), is used to indicate both internal and boundary node fluxes to represent boundary conditions. Internal sources (or sinks) are not used in this study.

Rearrangement of the mass conservation equation terms, with transmissibility D_{ml} [L^2/t] expressed as:

$$D_{ml} = kk_r\rho_l / \mu_l \quad , \qquad [20]$$

produces the air-water-isothermal flow equation seen in the users manual as (Zyvoloski et al., 1994b):

$$-\overline{\nabla} \bullet (D_{ml} \overline{\nabla} P_l) + q_m + \partial/\partial z(\overline{g} D_{ml}\rho_l) + \partial A_m/\partial t = 0 \qquad [21]$$

FEHM solves Equation [21] as a Jacobian matrix equation at each time step using the Newton-Raphson technique.

A particle tracking method was used to simulate advective transport of particles on a cell-by-cell basis. The method uses a residence time transfer function (RTTF) which includes the following two steps:

(1) Compute the residence time of a particle at a cell using the following method:

$$M_f \div \sum m_{out} = \tau^{part} \text{ or } \tau^{f}, \qquad [22]$$

where:

M_f is the fluid mass associated with a cell

M_{out} is the outlet fluid mass flow rates

τ is the residence time of a particle or fluid within each cell

(2) Send each particle to an adjacent cell, with the probability of traveling to a given cell proportional to the mass flow rate to that cell from the previous flow solution (Zyvoloski et al., 1994a).

Particle movement to a given cell is proportional to the liquid mass transferred to that cell from the flow solution of the system. Only advection was allowed to occur with no dispersion, reactions, or matrix diffusion. FEHM solves the equations that describe the RTTF method at each node and time step.

4.3. CODE OPTIONS USED

The FEHM code requires that input data used to run the simulations be sorted into groupings of similar code operations. These groups are referred to as macros. The macros used in this study are discussed below. Detailed information and input for each macro can be found in Zyvoloski et al. (1994b) and Appendix A.

pres The first simulation for each grid used a rough approximation of pressure and saturation designated in this macro for all cells in each material in the modeling domain. It assigns a single starting pressure and saturation for all cells in each material in the modeling domain.

init For each simulation following an earlier run, the previous output was used as the initial pressure and saturation conditions for each node in the modeling domain. When *init* macro is included, the *pres* macro is over written.

perm This macro assigns saturated permeabilities for all cells in each lithologic units in the modeling domain.

rpl This macro was used to assign the relative permeability and capillary pressure model type (in this case, van Genuchten) including the hydraulic parameters used to solve the air-water-isothermal flow equation for all cells in each material in the modeling domain. In the Basalt and Tschicoma units that were highly fractured, the code implemented an effective continuum (or continuous porous media) approach to represent permeability and capillary pressure. Here, a weighted average of the two sets of van Genuchten parameters was used, one to represent fracture flow and the other to represent matrix flow. Parameters needed in this macro included residual and maximum liquid saturations, inverse air entry pressure, the parameter "n" in the van Genuchten equation, and low cutoff point for unreliable low saturations in the fitting curve.

rock Material properties that are not saturation-dependent are assigned in this macro: rock densities, specific heat, and porosities. Values are assigned for all cells in each material in the modeling domain

coor This macro assigns nodes numbers and coordinates produced by either the GEOMESH grid generator (Gable et al., 1995) or the Rectangular Grid generator (Lundquist, 1994) discussed in section 4.5.

elem This macro describes how nodes are connected in the finite element grid. This information was produced by either the GEOMESH grid generator (Gable et al., 1995) or the Rectangular Grid generator (Lundquist, 1994) discussed in section 4.5.

zone Zones used in this study include lithologic and boundary zones. This macro assigns groups of lithologic and boundary nodes indicated in the *coor* macro to zones.

flow This macro specifies the type of system being modeled, in this case an isothermal air-water system. Boundary conditions are also specified here. Lower boundary nodes (at the water table), were given specified saturation conditions using a saturation of 0.99. Side boundaries are not specified here; therefore, a default no-flow condition is set. The upper surface boundary was a specified flux boundary. Saturations and an impedance parameter were designated at the boundaries, allowing conversions to mass-source or sink strengths. Boundary condition specifics and equations used are discussed in section 4.5.

time This macro controls the times used in the simulation. Values include length of simulation, initial time-step size, and maximum number of time steps allowed. Printout intervals and/or times for nodal information to be produced also can be indicated.

ctrl This macro assigns various control parameters needed for equation solvers and matrix solver routines. Assigned values include: (1) Maximum number of iterations allowed in either the overall Newton Raphson cycle or the inner cycle to solve for the corrections at each iteration. (2) Tolerance for the Newton Raphson cycle and the number of orthogonalizations in the linear equation solver. Second, the zone and order of partial Gauss elimination. (3) Implicitness factor, direction of gravity, and value of upstream weighting. (4) Time-step multiplier and the number of times it will be used, and the maximum and minimum time step sizes. (5) Parameters that specify the geometry (X-Y plane), and the external storage of geometric coefficients.

iter This macro sets parameters used in the linear equation solver routine: Multipliers for linear and quadratic convergence regions of the Newton-Raphson iterations, tolerances for the adaptive implicit method for the solver, over-relaxation factors, reduced degrees of freedom method, and reordering parameter.

sol This macro defines the type of solution required (coupled solution) and defines the element integration type (Lobatto or node point quadrature).

air This macro designates the type of air module used (1 degree of freedom solution to the saturated-unsaturated problem is produced). It also gives a reference temperature and pressure.

cont This macro sets the type of contour output (AVS) and the properties of the contours (pressures, Darcy fluxes, saturation, material properties, and concentrations of particles). The simulation time and time steps which are implemented also are indicated here.

ptrk This macro runs a particle tracking simulation with the following options: Number of particles to be released; times the flow solution and particle tracking solution is enabled and disabled; half-lives, phases, and concentrations of particles; transport mechanisms, sorption coefficient, dispersivity, molecular diffusion coefficients, and retardation factors; and matrix porosity and fracture spacing. Finally, the times and method that the particles entered the system is specified.

node This macro indicated the node numbers at which detailed output is desired. Output includes coordinates, temperatures, pressures, capillary pressures, flow fluxes, and energy fluxes.

4.4. BOUNDARY CONDITIONS

Boundary conditions for this study are described below and illustrated in Figure 4.1. Upper boundary nodes were given a specified flux condition at the base of the alluvium. The water budget recharge estimate applies to the entire upper section of the canyon. This rate was divided by the area of the canyon bottom to give a rate per unit area. Monthly rates given by Purtymun (1967) were averaged for a two-year period

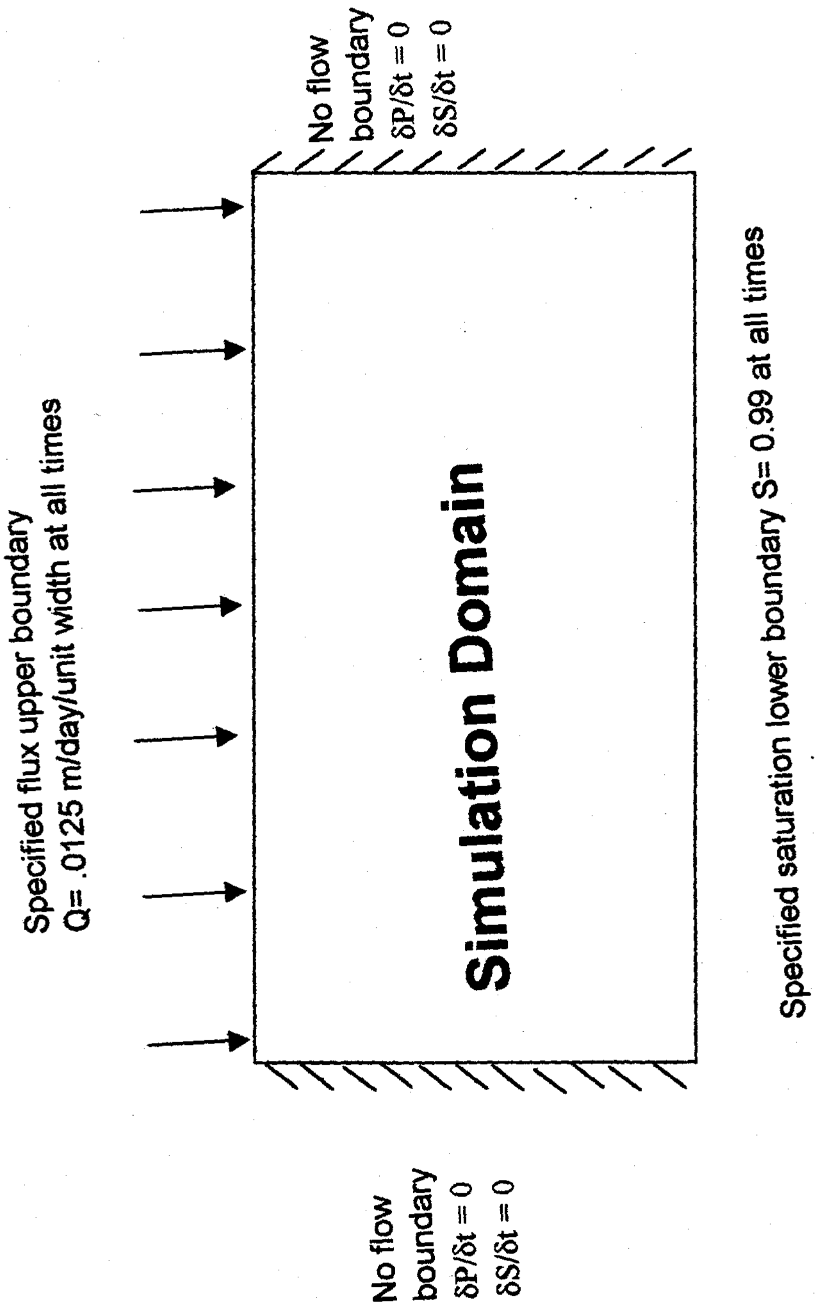

Figure 4.1 Boundary Condition

resulting in a 4.562 m/yr. recharge. The recharge rate was multiplied by the area along the top of each element to give volume for each cell. The volumetric recharge was converted to mass source strengths q_m [M/ L^3t]. This liquid source strength was used as the specified flux upper boundary condition [q(x,y,t)=constant]. Most simulations which incorporated this flux distributed it evenly along the upper boundary. Some simulations varied the amount or distribution of the flux across the upper boundary (described in Chapter 5). The lower boundary nodes in this simulation are located at the regional water table. Those nodes were given a specified saturation condition using a saturation of 0.99 [S(x,y,t)=0.99]. The code holds those nodes at these saturations during simulations, the mass source strength q_m [M/ L^3t] (or recharge to the water table) passes through these nodes at a rate determined by the equation:

$$q_m = I_m (S_l - S_{flow}) \quad , \qquad [23]$$

where I_m is an impedance factor [M/L^3t], S_l is the in-place liquid saturation, and S_{flow} is the specified saturation [unitless]. An impedance parameter of 1e-2 [M/L^3t] was used. It was set to produce expected fluxes out of the system within the code suggested few orders of magnitude of fluxes into the system.

No-flow side boundary conditions were used and no water was allowed to pass through side boundary nodes [q(x,y,t)=0]. Discussion of effects on the flow and particle tracking solutions due to this boundary condition are presented in Chapter 5.

4.5. FINITE ELEMENT GRIDS

Five finite element grids were used and are presented in this study. Four simple grids were produced using the Rectangular Grid Generator (Lundquist, 1994) and the fifth using the GEOMESH Grid Generator (Gable et al., 1995). Several variations on the dimensions of the grid cells and domain were explored. Specifics on grid changes and reasoning for changes are presented and discussed in detail in Chapter 5.

5. SIMULATION APPROACH, RESULTS, AND DISCUSSION

5.1. MODELING APPROACH

This chapter describes the modeling approach and simulations that were conducted. Throughout the chapter, Table 5.1 should be referred to as a useful summary and comparison of the simulations. Differences between simulations include changes in grid sizes, domain sizes, tilting of stratigraphy, presence of volcanics (Unit 2 Basalt and Tschicoma Formation), and changes in recharge amount and distribution. Twelve simulations of flow and transport are presented.

The first four simulations indicated in Table 5.1, as simulation numbers 1-4, vary mainly in terms of spatial discretization of five separate structured (distinguishable rows and columns), rectangular, two-dimensional, finite-element grids. They are used to evaluate the effect of grid size and spacing in solution quality. A stratigraphic profile, taken at -1200 m on the x-axis of the canyon's longitudinal section in Figure 3.6, was used for the lithologic interfaces for these grids, numbered 1-4. The Unit 2 Basalts are combined with the Tschicoma Formation and given common material properties and referred to as the Basalt/Tschicoma unit or the volcanics.

The next seven simulations indicated as simulation numbers 5-11 in Table 5.1, incorporate variations in parameters affecting the flow and transport solutions using the grid (number 3) that gives the best solution. Sensitivity to parameters of high uncertainty

Table 5.1 Simulation Descriptions.

grid name	grid #	simulation #	width	depth	horizontal spacing	vertical spacing	vertical spacing per unit	number of nodes	number of elements	stratigraphic dip?	volcanics present?	transect location	horizontal transects	base case recharge	recharge distribution	purpose
vertical rectangular grid	1	1	50 m	314 m	2 m	2 m	varies	4108	3925	n	y	center	n	x 1	even	examine effects of dipping stratigraphy
tilted rectangular grid	2	2	50 m	314 m	2 m	2 m	varies	4108	3925	y	y	center	y	x 1	even	examine effects of dipping stratigraphy
1st refined rectangular grid	3	3	300m	314 m	1.5m	varies	16	29145	28800	y	y	center	y	x 1	even	examine effects of grid size and material interface resolution
2nd refined rectangular grid	4	4	300m	314 m	1.5m	varies	14	25527	25200	y	y	center	n	x 1	even	assure 1st refined is properly discretized
1st refined rectangular grid	3	5	300m	314 m	1.5m	varies	16	29145	28800	y	n	center	n	x 1	even	examine effects of absence of fractures
1st refined rectangular grid	3	6	300m	314 m	1.5m	varies	16	29145	28800	y	y	center	n	x 2	even	examine effects of increasing recharge
1st refined rectangular grid	3	7	300m	314 m	1.5m	varies	16	29145	28800	y	y	center	n	x 0.5	even	examine effects of decreasing recharge
1st refined rectangular grid	3	8	300m	314 m	1.5m	varies	16	29145	28800	y	y	center	n	x 0.1	even	examine effects of decreasing recharge
1st refined rectangular grid	3	9	300m	315 m	1.5m	varies	16	29145	28800			center	n	x 0.01	even	examine effects of decreasing recharge
1st refined rectangular grid	3	10	300m	314 m	1.5m	varies	16	29145	28800	y	y	none	n	x 1	increase	examine effects of changing recharge distribution
1st refined rectangular grid	3	11	300m	314 m	1.5m	varies	16	29145	28800	y	y	none	n	x 1	decrease	examine effects of changing recharge distribution
Mortandad Canyon Grid	5	12	1828m	varies	varies	varies	varies	23981	46346	y	in parts	300-m interval	n	x 1	even	model entire cross-section

were explored by varying the distribution and amounts of recharge, and removing the Unit 2 Basalt/Tschicoma Formation which may not extend through this longitudinal section.

The final simulation, number 12, included an unstructured (undistinguishable columns and rows), triangular, two-dimensional, finite element grid, number 5. This grid included the entire longitudinal section in Figure 3.6. Its purpose was to simulate flow in the unsaturated zone beneath all of Upper Mortandad Canyon. It includes all lithologic contacts and thickness ranges encountered, whereas other simulations depicted a specific stratigraphic profile from that longitudinal section.

Material properties for each unit, described in section 3.3 and in Table 3.1, were used as input data for all simulations. Boundary conditions, described in section 4.4 and in Figure 4.1, included no flow for the sides, specified saturation for the bottom, and specified flux for the top, for all simulations.

A steady-state solution was assumed to be achieved once the fluid mass in the domain remained constant (changing less than $1.0\text{x}10^{-5}$ kg) with respect to simulation time. Simulated time was performed out to 1E+9 days to assure water mass in the domain was constant. Time step size increased by a factor of 1.2 if a solution falls within a tolerance or maximum difference of 1E-5 of the previous solution within 10 iterations. If the solution fails to meet this convergence criteria, the time step size is reduced by half. The factors of increasing and decreasing time step size, tolerance, and number of iterations are set by the modeler. All simulations ran until they met steady-state criteria described above. In Figure 5.1, simulated time is plotted against both fluid mass and time step size for one of the simulations later discussed. The results showed that the total water in the domain drained until a constant mass was reached at about 1E-5 days. Some lithologic units drained while others filled depending on initial saturations in those units. Beyond that same simulated time (1E-5 days), time step size increases steadily. The exception is notch at the far right side of the time-step size plot. This final time-step did meet the convergence criteria; however, the final time step size is not a full increment in order to match the specified final simulation time (1e+9). Later simulations reached steady-state much earlier because the initial saturations were better estimated from previous results.

Several modeling assumptions were made in this study. The two-dimensional longitudinal section used in these simulations assumes no flow perpendicular to the canyon axis. Geddis (1992) modeled the system in a cross section perpendicular to the canyon axis and concluded that subsurface flow in that direction was minimal.

Recharge is assumed to be distributed evenly along the study area: There is uncertainty associated with the water budget estimates of this recharge into the tuff, and it is not known how this recharge is distributed in time and space. Results that follow show the systems behavior with recharge higher, lower, and equal to the water budget estimates. Results also are shown for two extreme cases of recharge distribution: Recharge both increasing and decreasing linearly along the upper boundary, with respect to distance from the western side of the modeling domain.

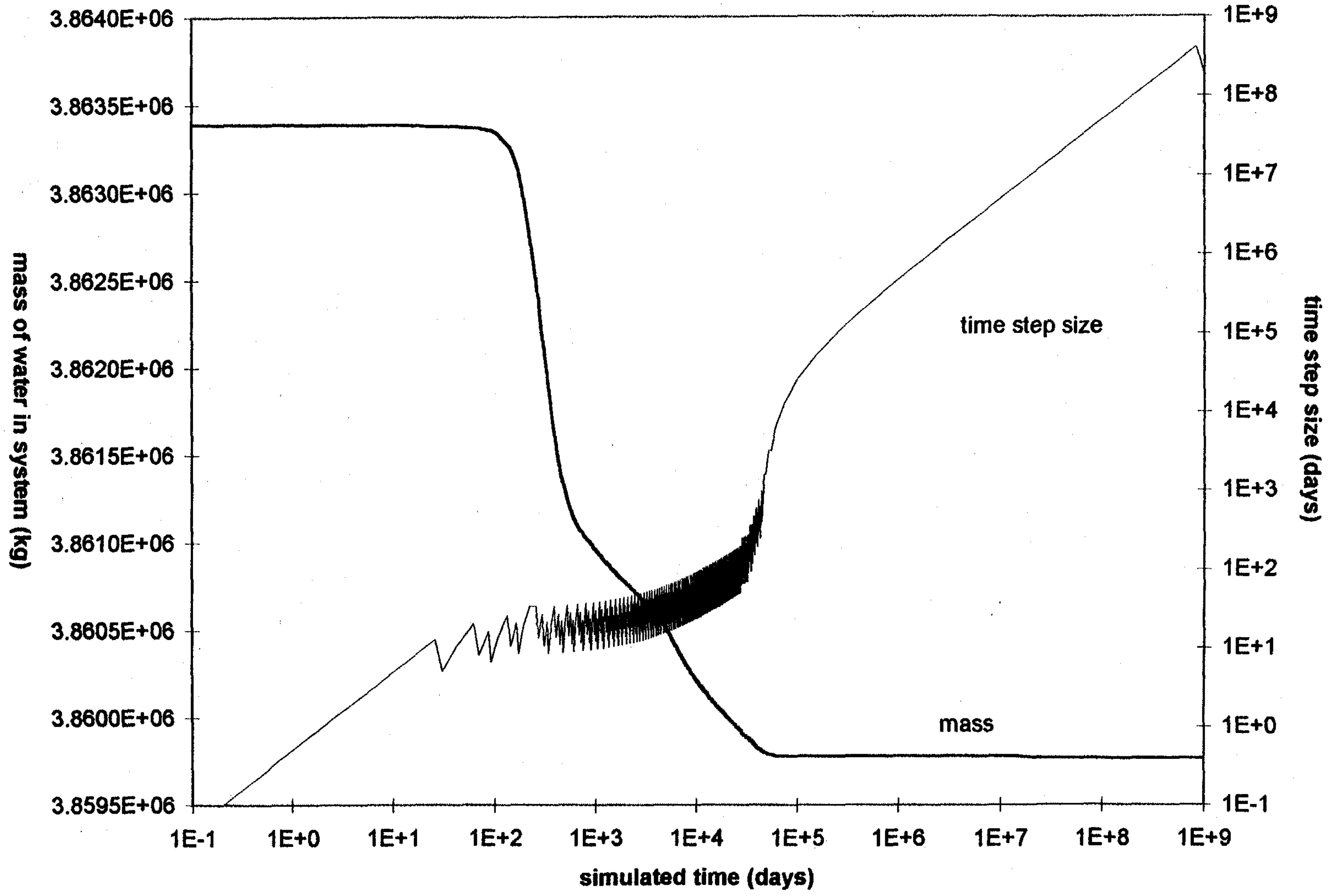

Figure 5.1 Steady-state constant mass and infinite time step.

Another assumption was that material and hydraulic properties of the rocks are isotropic and homogeneous. Additionally, the extent of the Puye Formation, Tschicoma Formation, and Unit 2 Basalt as well as their associated properties are not known.

Finally, the Guaje Pumice Bed is shown dipping down canyon. Its actual dip is slightly away from the canyon axis, but that cannot be incorporated into the two-dimensional approach used here. The effect of this would divert water away from the canyon axis causing lower saturations and slower flow rates along the canyon axis than modeled in this study. In reality a component of horizontal flow away from the canyon axis would be present, but, it is not know how great it would be. It is assumed that it would be small based on the actual dip in that bed and the two-dimensional approach would be sufficient to represent this system.

5.2. VERTICAL RECTANGULAR GRID NUMBER 1, SIMULATION 1

This simulation used a simple grid. It illustrates the importance of the dip in the stratigraphy. The stratigraphy above -1200 m on the x-axis of the canyon's longitudinal section in Figure 3.6, was used to indicate lithologic interfaces in grids 1-4. Material properties for each unit, described in section 3.3 and Table 3.1, were used as input data for all simulations. Boundary conditions for simulations 1-4 included no flow for the sides, specified saturation for the bottom, and specified flux of base case recharge for the top.

A two-dimensional rectangular grid was constructed with properties given in Table 5.1 (grid number 1). Lithologic interface contact elevations were adjusted slightly to match the 2 m grid spacing intervals extending horizontally across the grid seen in Figure 5.2.

Initial conditions for all nodes were set at a saturation of 0.30. Thus, when the simulations began, saturations changed (filling or emptying pores), while the nodes in each lithologic unit in the system approached the appropriate pressures and saturations according to the material characteristic curves.

Flow results of this simulation from the horizontal center of the grid are plotted as pressure, saturation, average linear velocity, and Darcy flux depth profiles along side similar results of the same grid but tilted for comparison reasons (Figures 5.3, 5.4, and 5.5). Comparison of the simulations illustrate the effects of dipping stratigraphy and are discussed further in section 5.3.

Resulting pressure heads matched saturations in Figure 5.3 for each lithologic unit according to respective characteristic curves shown in Figure 3.3B. Note that gage pressures are given in Figure 5.3 and matric suction are given in Figure 3.3B, both are in MPa. The largest changes in pressures and saturations occur at each lithologic interface shown in Figure 5.3. Saturation values in the lower units, the Puye Formation

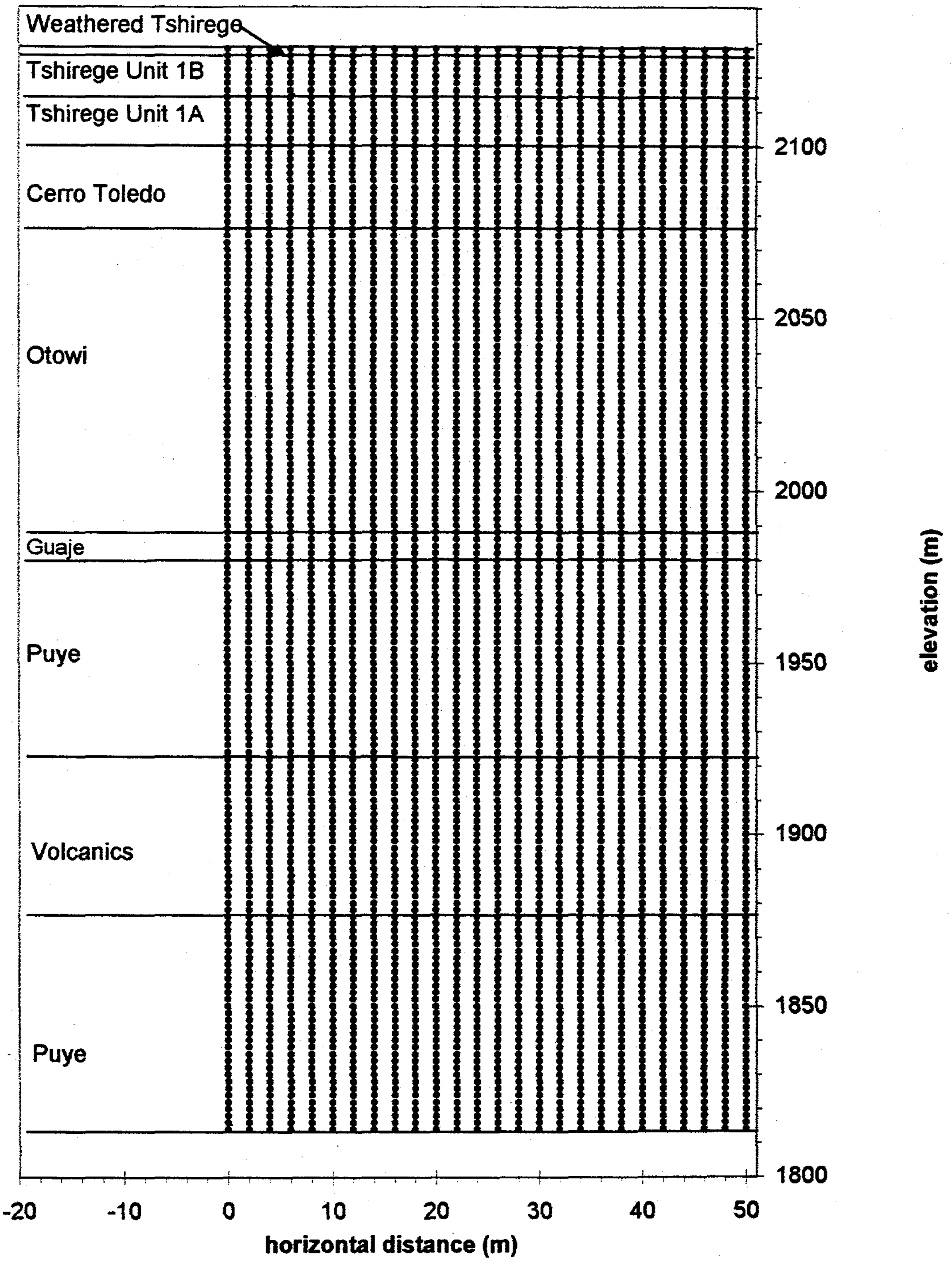

Figure 5.2 Node locations in Vertical Rectangular Grid, with about 1:4 vertical exageration.

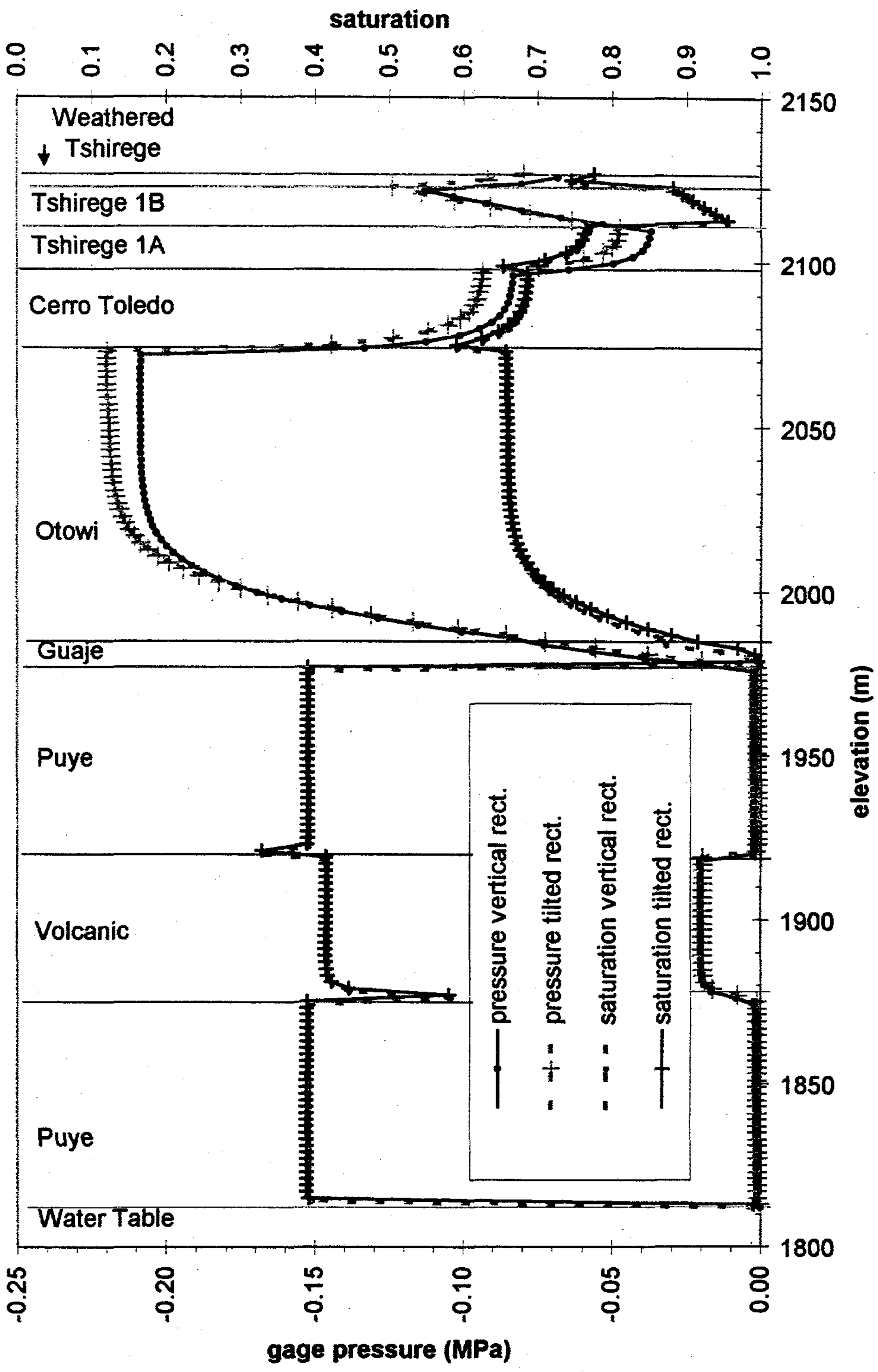

Figure 5.3 Pressure and saturation depth profile at center of Vertical Rectangular and Tilted Rectangular Grids.

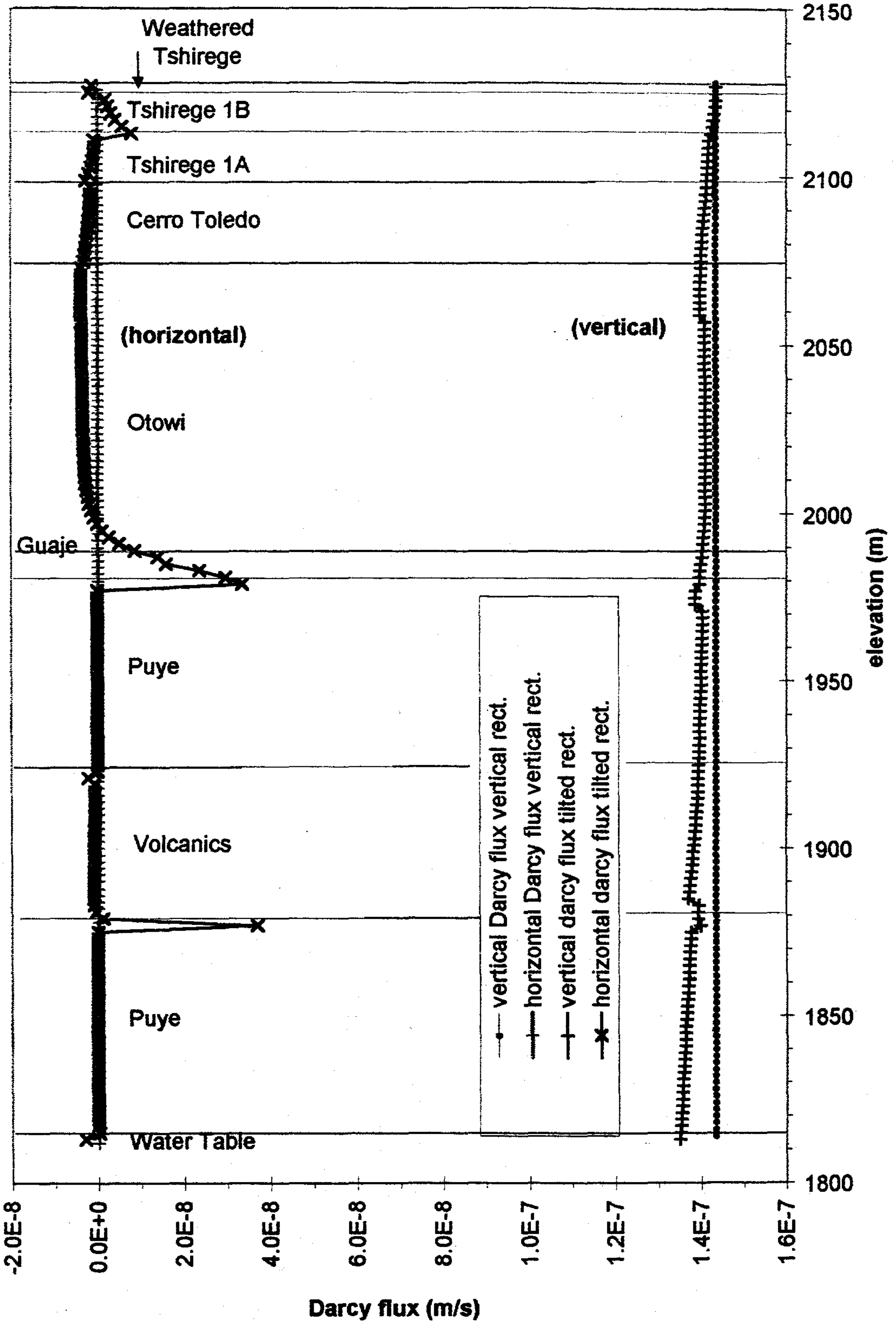

Figure 5.4 Vertical and horizontal Darcy flux depth profile at center of Vertical Rectangular and Tilted Rentangular Grids.

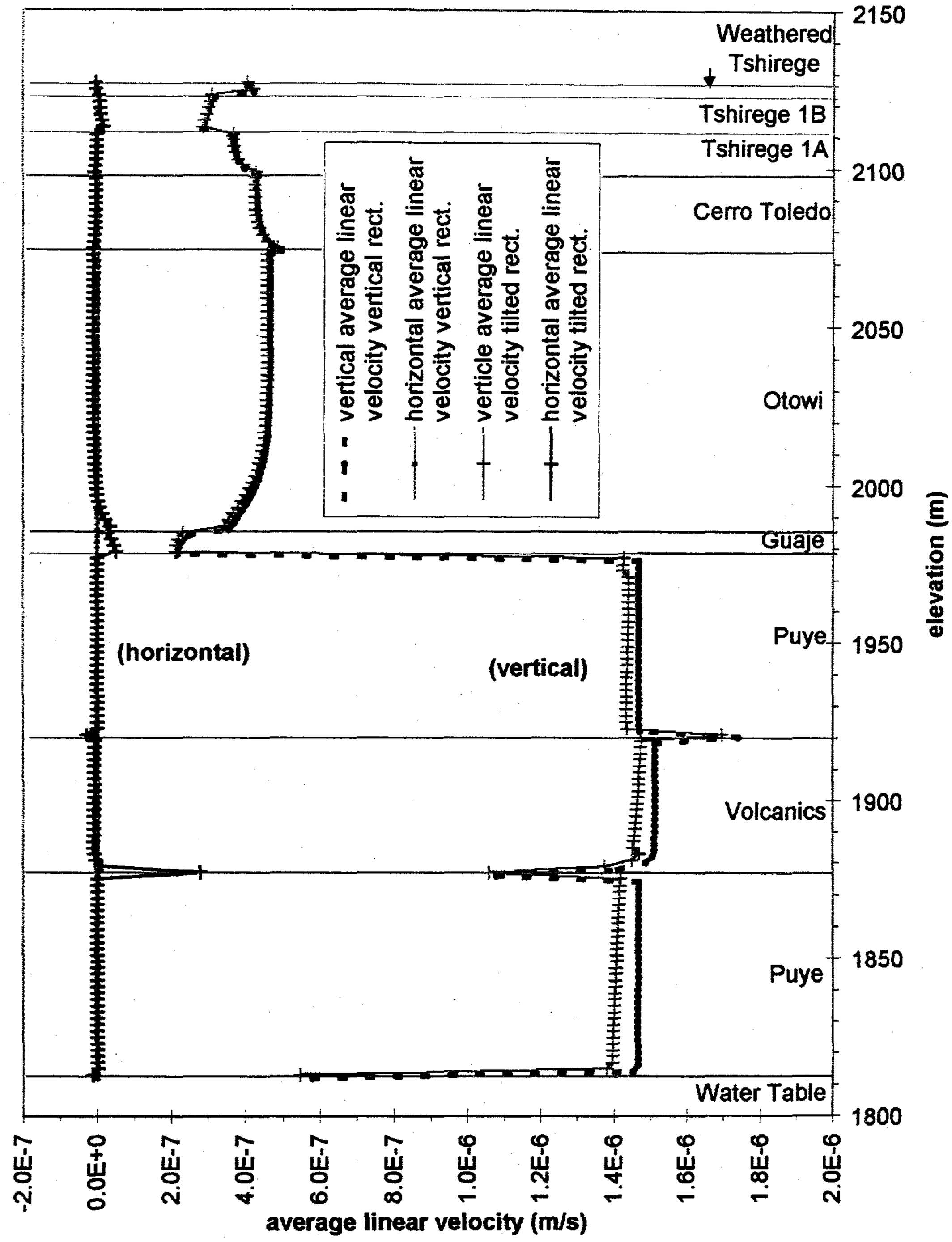

Figure 5.5 Vertical and horizontal average linear velocity depth profile at centerof Vertical Rectangular and Tilted Rectangular Grids.

and volcanics, are much less than those in the upper Bandelier Tuff units. Pressures in the Puye Formation are close to atmospheric. However, the slope and position of the characteristic curves in Figure 3.3B, dictate that the saturations remain at 40% while the base of the Guaje Pumice Bed with less pressure (more matric suction) reaches saturation. The base of the Tshirege Unit 1B is close to saturation at about 97%.

The FEHM code outputs a Darcy flux that indicates the mean specific discharge at each node in the system, they are plotted in Figure 5.4. The Darcy flux was converted to average linear velocity by dividing by the volumetric water content at each node. These average linear velocities plotted in Figure 5.5 represent the rate at which a solute would move through the system with no dispersion, reactions, or matrix diffusion. There are no horizontal components of flow shown in either figure for this simulation. This is due to the horizontal orientation of the stratigraphy and the constant recharge flux at each node along the upper boundary. Vertical Darcy flux is constant throughout the depth profile at 1.43E-7. Vertical average linear velocity changes according to the saturations seen in Figure 5.3 and porosity of each material throughout the depth profile. The largest changes in velocities and saturations occur at each lithologic interface.

Using this flow solution, a particle tracking simulation was performed in order to find the rates and pathways of a solute in the system. A pulse of 1000 particles entered the system at a center node on the upper boundary.

Results from the particle tracking simulation are plotted as a breakthrough curve at the lower boundary in Figure 5.6. The plot show breakthrough curves for simulations

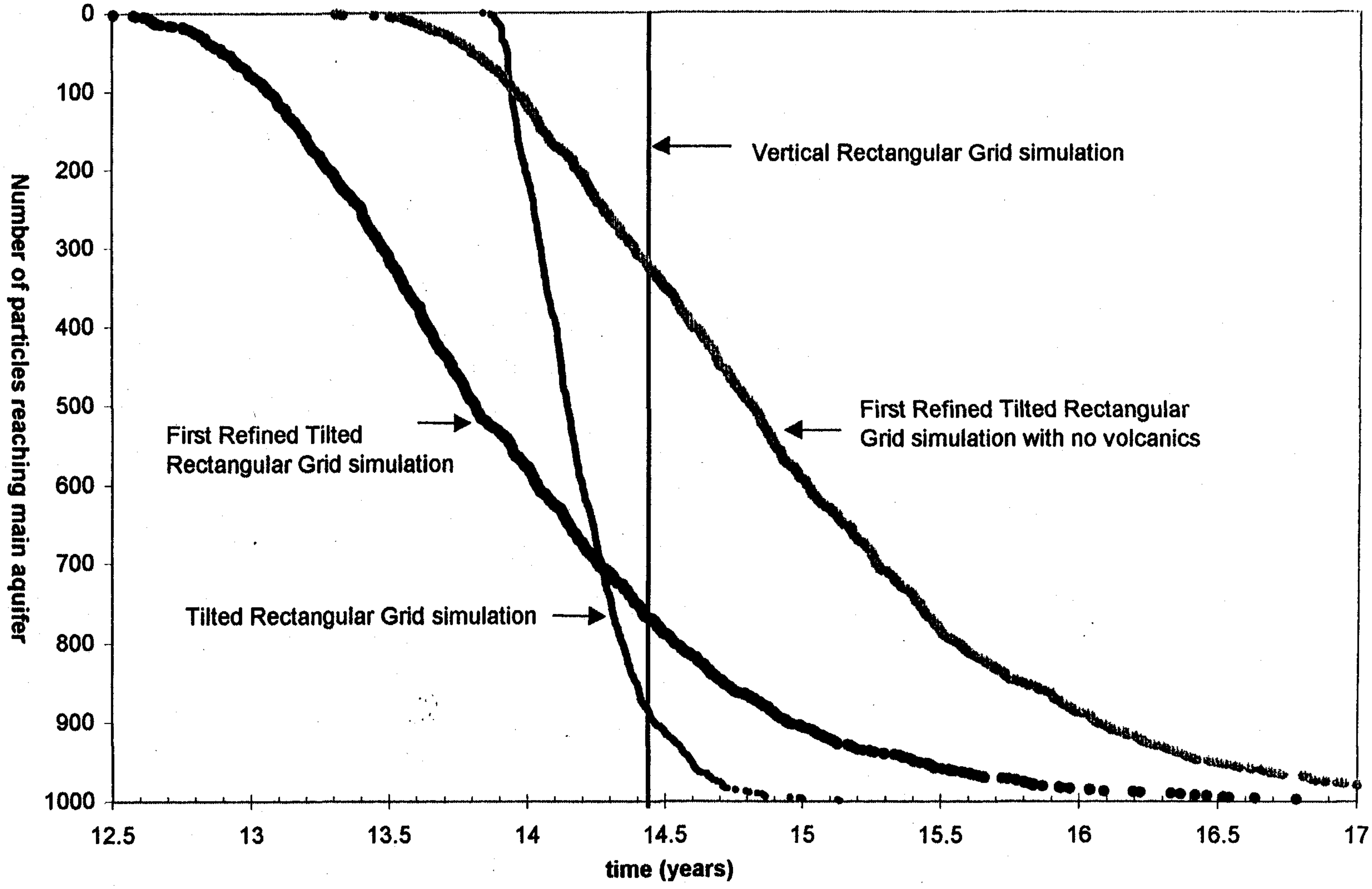

Figure 5.6 Breakthrough curves for various grid simulations at base case recharge.

discussed in the following sections; the curve representing this simulation is labeled "Vertical Rectangular" near the center of the figure. The plot shows times in years required for the particles to reach the regional aquifer. Because there is no horizontal flow occurring in this simulation, all of the particles travel downward at the same rate; however, that rate varies according to the average linear velocities at each node. The breakthrough curve for this simulation shows piston flow, with all particles arriving at the lower boundary at the same time, at approximately 14.4 years.

5.3. TILTED RECTANGULAR GRID NUMBER 2, SIMULATION 2

To better represent the dipping stratigraphy beneath Upper Mortandad Canyon, the grid described in the prior example was rotated so the beds dip down-canyon (Figure 5.7). The setup was the same as the previous grid, except that this grid is rotated 1.3°. The angle of the grid rotation was chosen using the dip of the Guaje Pumice Bed, which is close to the dip of the other units. The greatest horizontal flow velocities were expected in the Guaje based on the previous simulation results. The dips from the other units were tested and differences in results were small. Initial conditions for all nodes were set according to the final conditions of the previous simulation. The stratigraphy and all other code parameters were the same as the previous simulation.

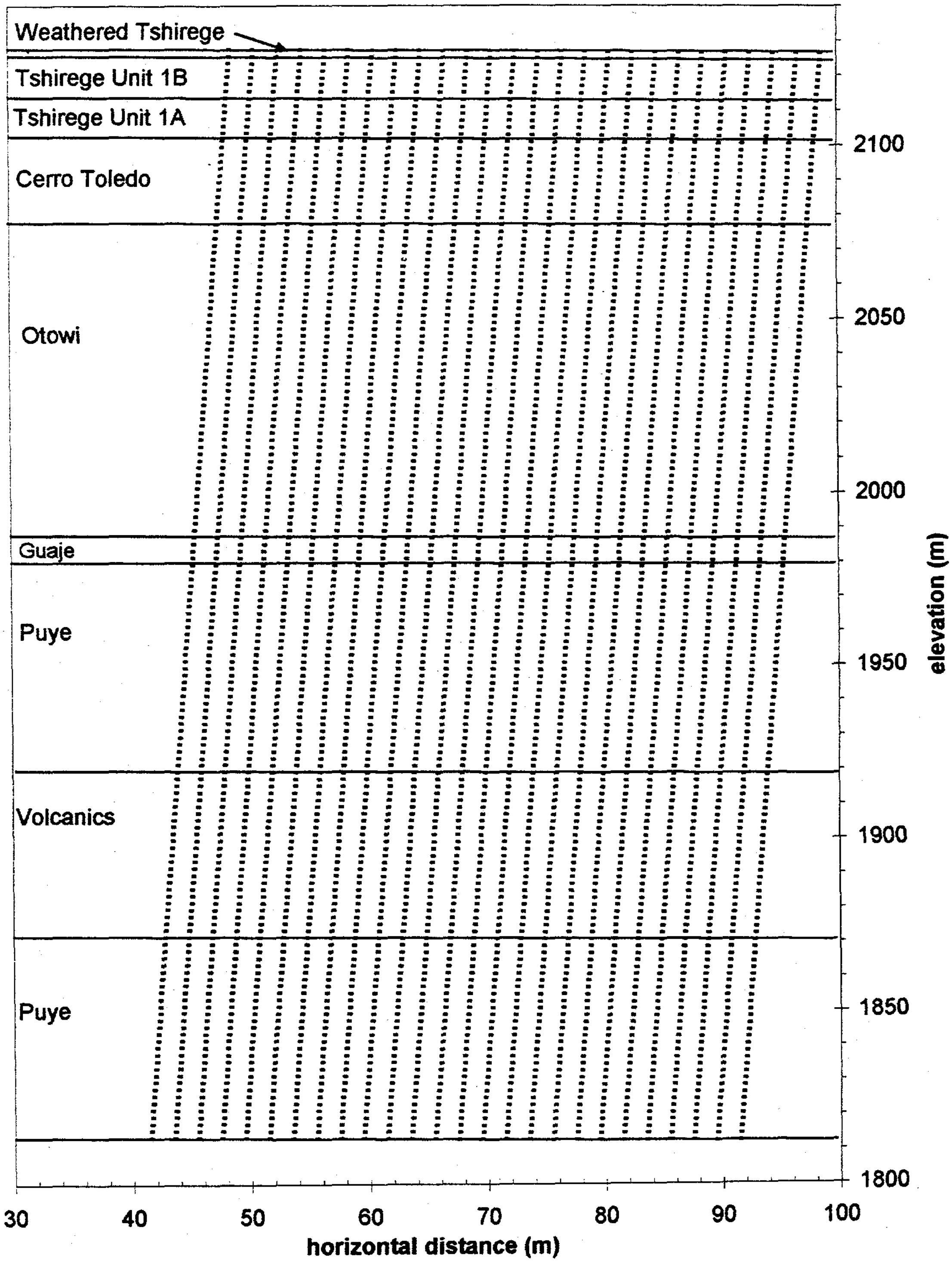

Figure 5.7 Node locations in Tilted Rectangular Grid, with about 4:1 vertical exageration.

Flow results from the horizontal center of the grid of this simulation (number 2) are plotted as depth profiles shown alongside results from the Vertical Rectangular Grid simulation (number 1) in Figures 5.3-5.5.

Saturation profiles seen in Figure 5.3, are similar for both simulations. However, pressures in the Bandelier Tuff are slightly lower in simulation 2 than in simulation 1. Reasons for this are discovered and discussed later in this section. A horizontal component of average linear velocity and Darcy flux is apparent at each lithologic contact seen in Figures 5.4 and 5.5. A localized change in vertical velocity can also be seen in the same figures at these lithologic contacts. Lateral flow occurs along dipping interfaces where there is a large permeability and hydraulic conductivity contrast. Capillary barriers are most evident in Figures 5.3-5.5 at the Tshirege 1B/1A interface, the Guaje/upper Puye interface, and at the Basalt/lower Puye interface. At these interfaces there is a large contrast in hydraulic conductivity; this results in increased saturation, and horizontal flow above these interfaces. The highest vertical average linear velocities are occurring within the volcanic and Puye formations, which have the higher hydraulic conductivity. The lowest vertical average linear velocities occur in the less conductive upper units. In theory, vertical Darcy flux within any lithologic unit with the same material properties should remain constant with depth. This is not the case in Figure 5.4 and an influence from the side boundary condition imposed was suspected to be at fault, and tested for.

Pressure, saturation, vertical Darcy flux, and horizontal Darcy flux at each node in the domain are plotted relative to their horizontal position in Figures 5.8, 5.9, 5.10, and 5.11, respectively. This was done to determine and illustrate if and to what degree side boundary conditions imposed effect the solution throughout the domain. Ideally, nodes occurring along the same row should have similar values regardless of horizontal position. Some node values occurring across the same row in the grid have been connected to illustrate their variability next to a horizontal line for comparison. The maximum difference in gage pressure along a same row 16 m from center (horizontal distance particles travel at this recharge rate discussed later), was 0.0043 Mpa. The maximum difference in saturation along a same row 16 m from center, was 1.46%. Those values seem small; however, they produce a greater effect on the Darcy fluxes. The maximum difference in vertical Darcy flux along a same row 16 m from center, was 3.67E-8 or 26.7%. Furthermore, the maximum difference in horizontal Darcy flux along a same row 16 m from center, was 5.62E-9 or 63.5%. Variations in values along the same grid row are caused by the no-flow side boundary conditions. Little moisture reaches the deeper units near the up-gradient (left) side boundary, while a build-up of moisture occurs on the down-gradient (right) side boundary. This in turn causes increased rates of flux to the down-gradient (right) side and decreased rates of flux to the up-gradient (left) side. This effect (variations in values across rows) is less apparent inward from the sides. Therefore, increasing the width of the simulation domain could move these side effects away from most of the domain.

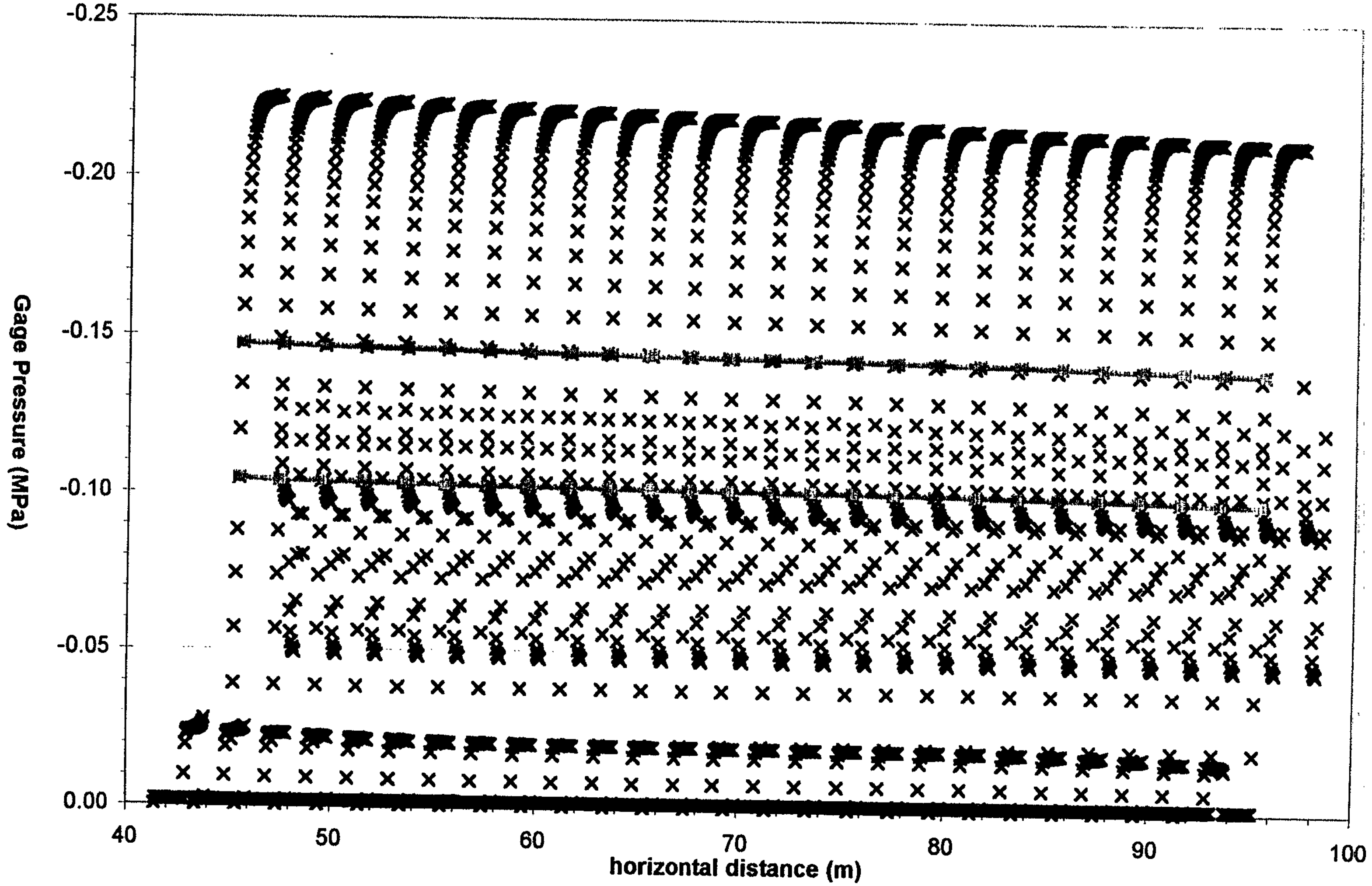

Figure 5.8 Pressure at each node in the Tilted Rectangular Grid simulation with respect to horizontal position.

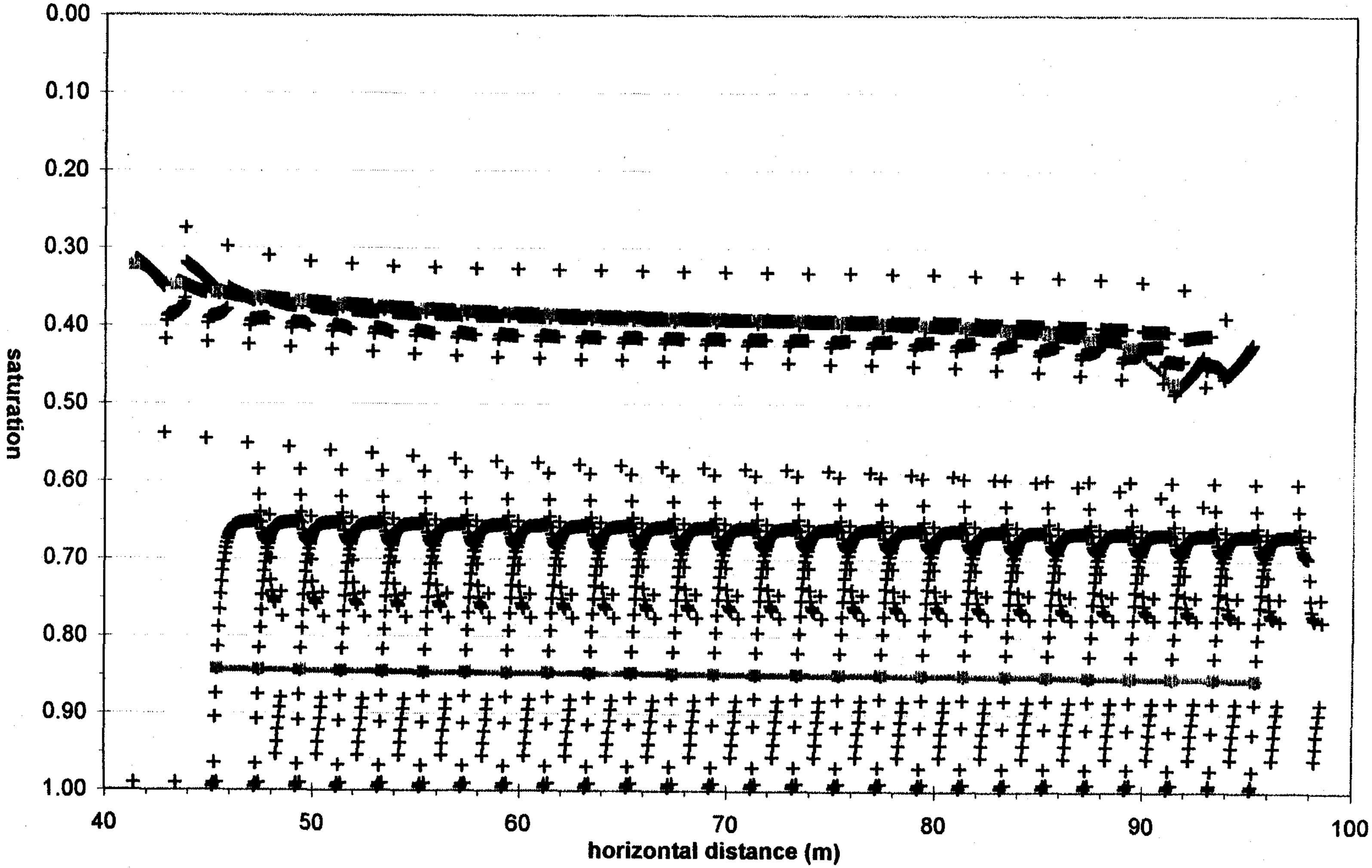

Figure 5.9 Saturation at each node in the Tilted Rectangular Grid simulation with respect to horizontal position.

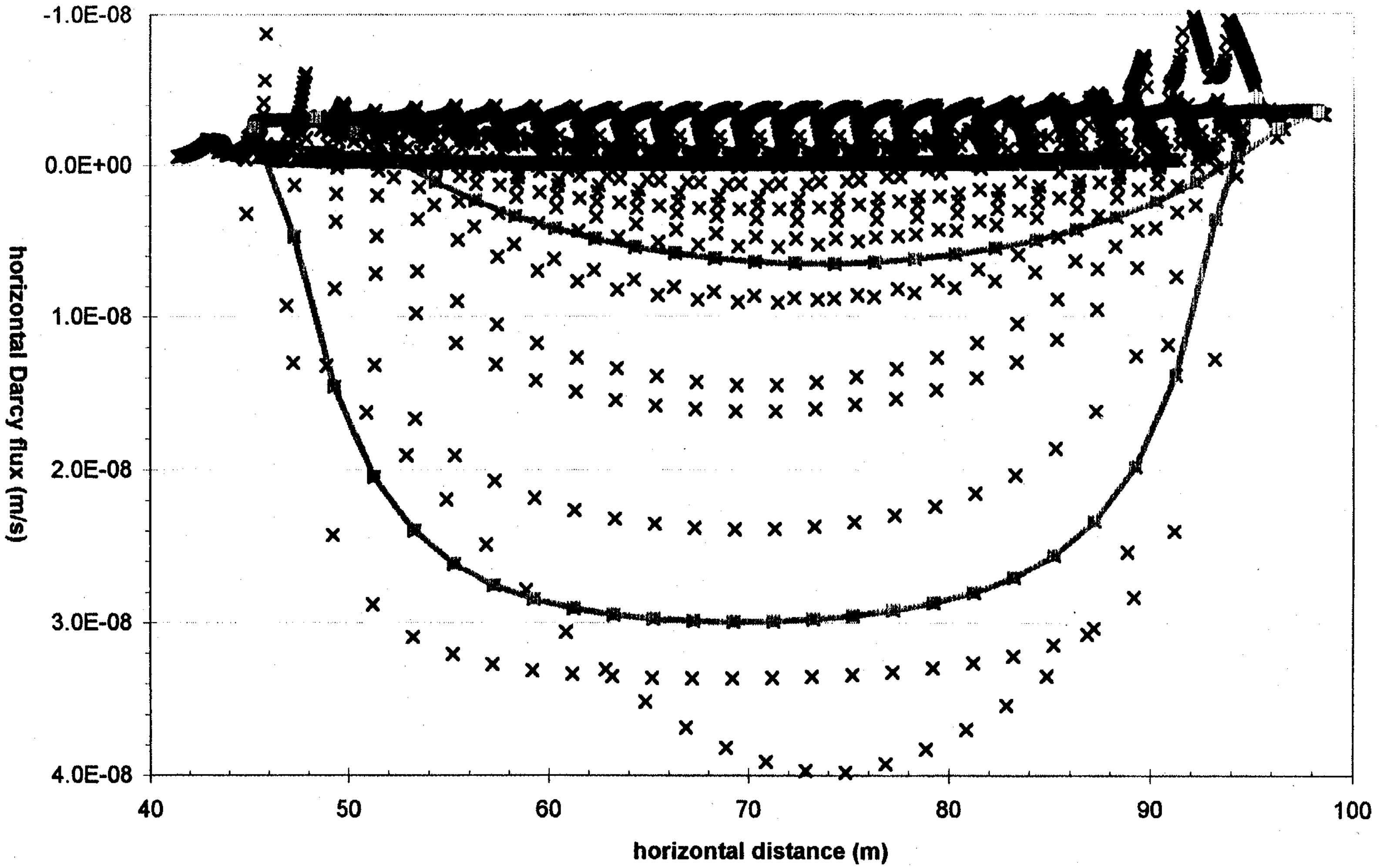

Figure 5.10 Horizontal darcy flux at each node in the Tilted Rectangular Grid simulation with respect to horizontal position.

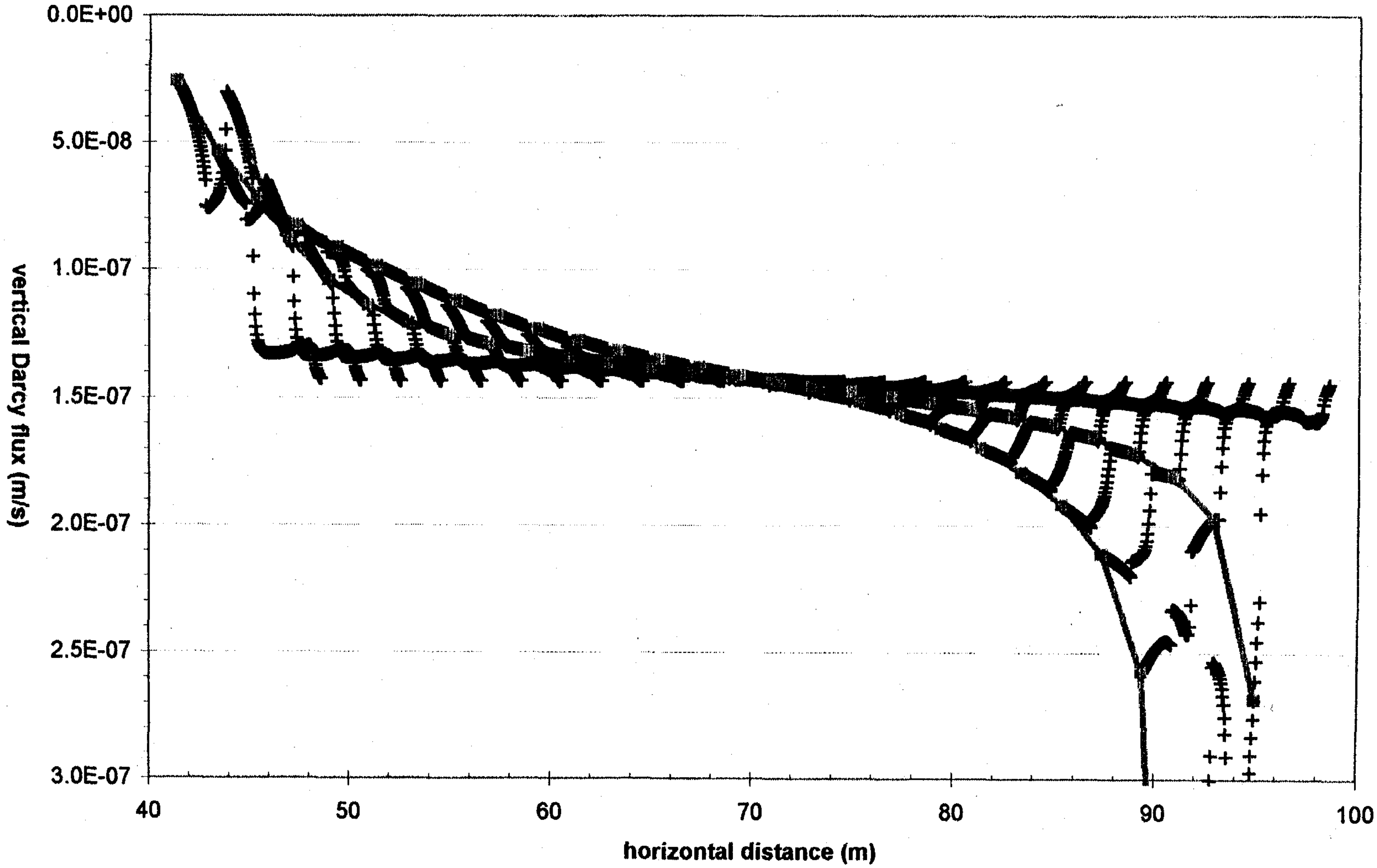

Figure 5.11 Vertical Darcy flux at each node in the Tilted Rectangular Grid simulation with respect to horizontal position.

Using the flow solution from this tilted grid simulation, a particle tracking simulation was performed. The particle tracking was done in the same manner as with the previous grid simulation without the dipping stratigraphy. Results from the particle tracking simulation are plotted as a breakthrough curve at the lower boundary and indicated as "Tilted Rectangular" in Figure 5.6. The breakthrough curve for this simulation shows the mean of the particles arriving at the lower boundary in approximately 14 years. Due to higher flow rates in part of the grid, resulting from influence of side boundary conditions and tilting of the grid, the arrival time of 14 years is faster than the Vertical Rectangular Grid. The apparent dispersion exhibited in the plot (particles arriving at varying times) is caused by differences in flow across the grid. The path taken by each particle affects the arrival time to the lower boundary and intermediate nodes. The horizontal distance traveled by particles by the time they reach the regional aquifer is approximately 16 m.

These two simulations provide a base case for comparison to subsequent simulations; provide an estimate of pressures, saturations, and velocities in the system; illustrate the importance of the dip in the stratigraphy; and outlined some new issues of concern. Specific issues which are addressed in following simulations include: the domain width's relation to the influence of side boundary conditions; the grid cell dimensions relation to differences in particle arrival times in breakthrough curves; and the need for better grid resolution at lithologic interfaces.

5.4. FIRST REFINED TILTED RECTANGULAR GRID NUMBER 3, SIMULATION 3

This refined grid was developed for several reasons: The first was to illustrate the effect of grid size and spacing on the flow and particle tracking solutions. Based on the previous simulation (number 2) vertical spacing at the lithologic interfaces needed to be reduced to better capture large changes in flow results occurring there. The second was to determine the extent of the zone of influence from the side boundary conditions. The third was to obtain a solution with minimal effects from the side boundary conditions. To achieve this the domain width was expanded to a size that isolated side boundary influence from most of the flow solution, and accommodated the particle tracking solution away from that zone of influence. Boundary influence response to adjustments in horizontal node spacing was explored with little effect, but domain width was determined to be the important factor.

Properties of the Refined Tilted Rectangular Grid (number 3) are listed in Table 5.1 and shown in Figure 5.12. The stratigraphy and all other code parameters were the same as previous simulations. Horizontal node spacing is always 1.5 m. Each lithologic unit included 16 rows of nodes that decrease in height by a factor of 1/2 towards the lithologic interfaces. The vertical node spacing varied with proximity to the interface, between 14.50 m at the center of the largest unit and 0.07 m next to the interface of the thinnest unit. This kept the number of nodes to a minimum, gave adequate resolution where needed, and captured large changes in system response at each interface. All other code parameters were the same as the previous simulation.

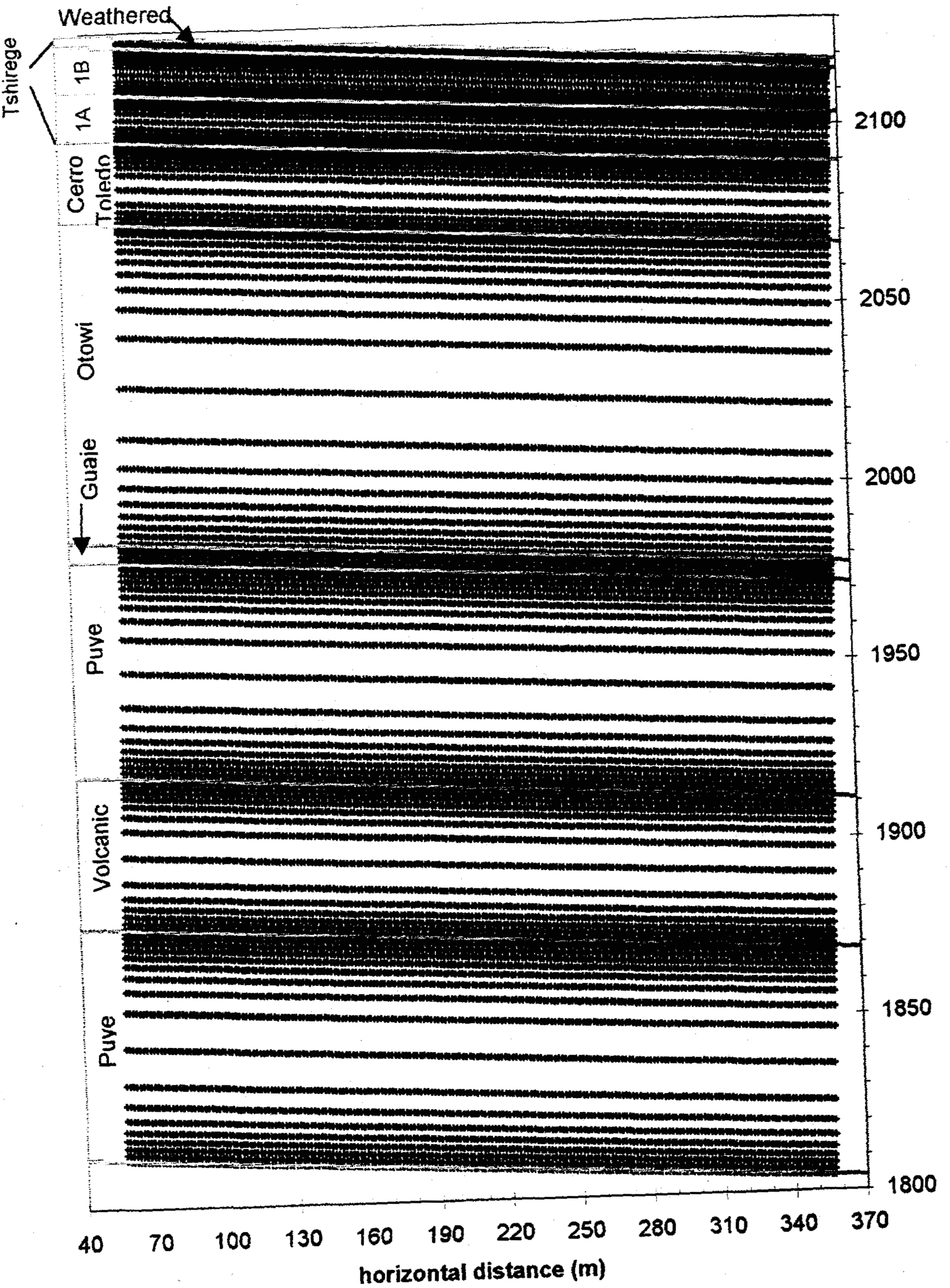

Figure 5.12 Node locations in First Refined Grid, with about 2:3 vertical exaggeration.

Flow results from the horizontal center are plotted as depth profiles and indicated as Refined 1 in Figures 5.13, 5.14, 5.15, 5.16, 5.17, and 5.18.

Saturations and pressures seen in previous simulations differ slightly from this simulation mainly in the Bandelier Tuff units (Figures 5.13 and 5.14). This is attributed to the influence from side boundary conditions influencing center nodes in the previous simulations. That influence is now isolated from most of the flow solution in this simulation because of the wider domain creating a more accurate solution for nodes near the center of the domain. The same can be said for the vertical and horizontal Darcy flux and average linear velocity depth profiles in figures 5.15-5.18. This difference is best illustrated in the vertical Darcy flux depth profile in Figure 5.17, because of the small range in flux rates.

Reducing vertical grid spacing at lithologic contacts also changed the solution in another way, that difference is most noticeable in both average linear velocity profiles in Figure 5.15-5.16. The peaks and dips at the top and bottom of the volcanics in these profiles are sharper and larger at the lithologic interfaces than previous simulation due to this increased vertical resolution. The maximum horizontal velocity which occurs at the base of the volcanics are twice as high in this simulation 3 than simulation 2. Maximum vertical velocity, which occurs at the base of the upper Puye unit is approximately 5% higher than that velocity in simulation 2. Differences in peak values of results indicate that the previous grids were not adequately discretized at important locations (at lithologic interfaces).

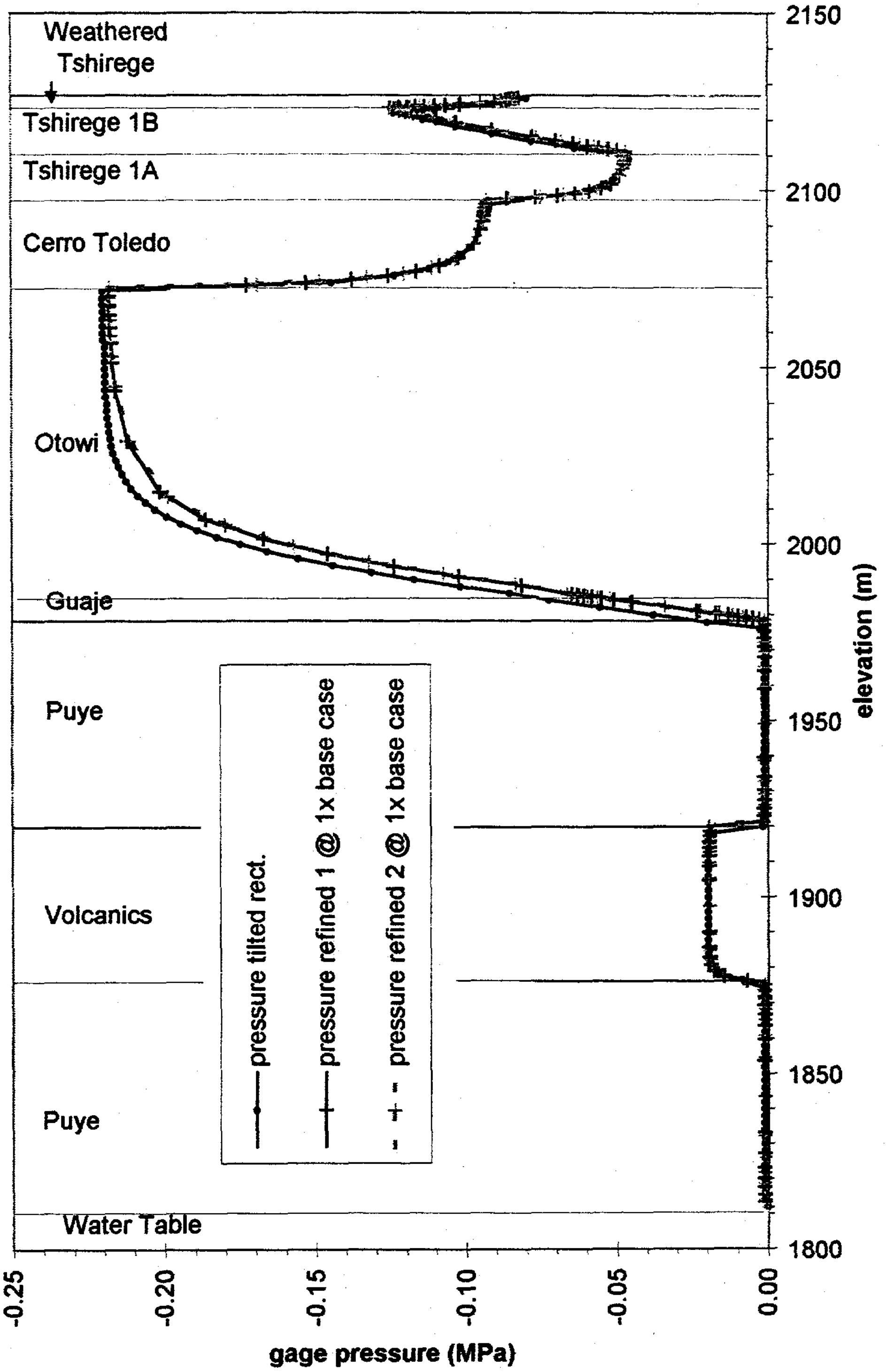

Figure 5.13 Pressure depth profile at center of each grid.

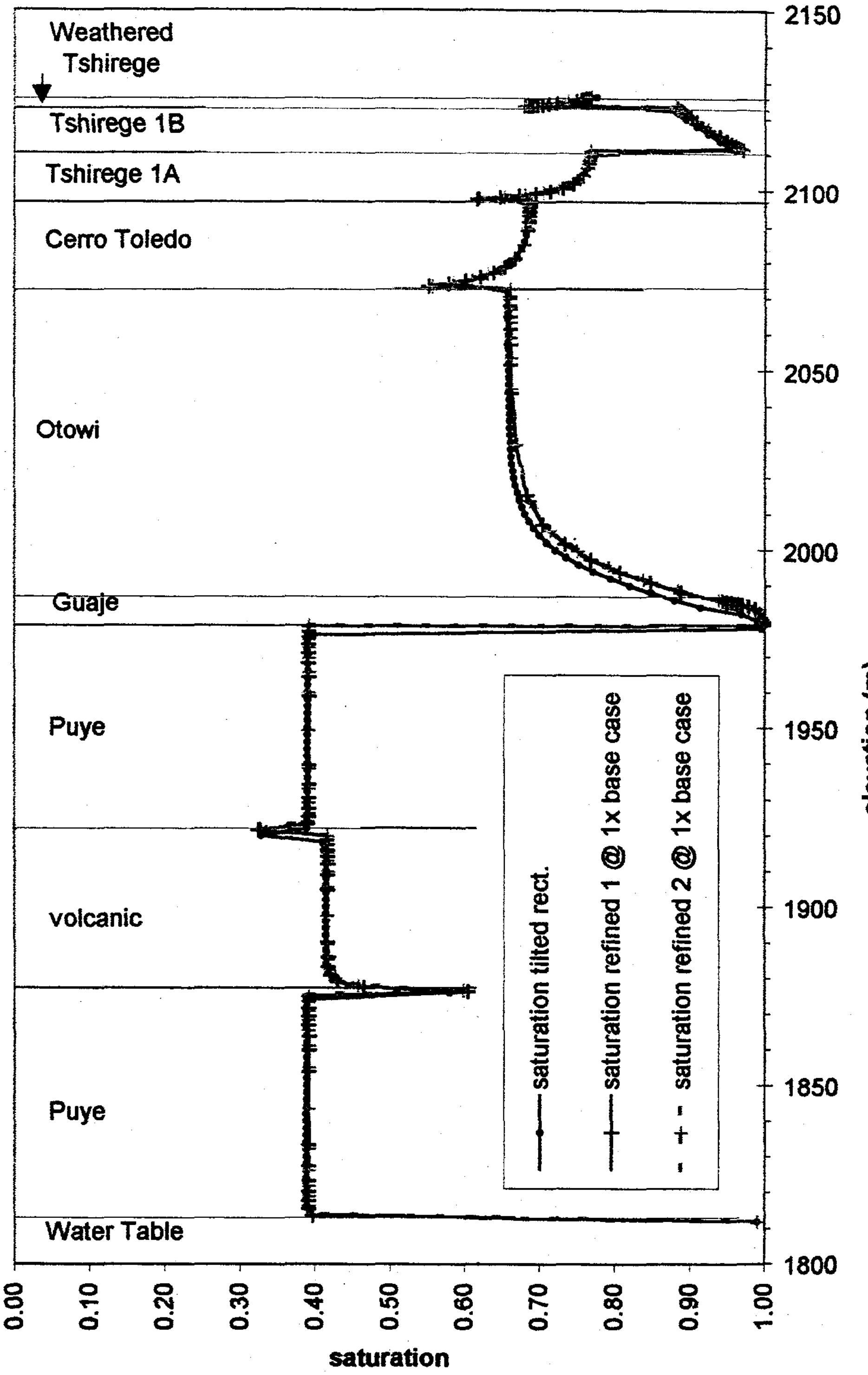

Figure 5.14 Saturation depth profile at center of each grid.

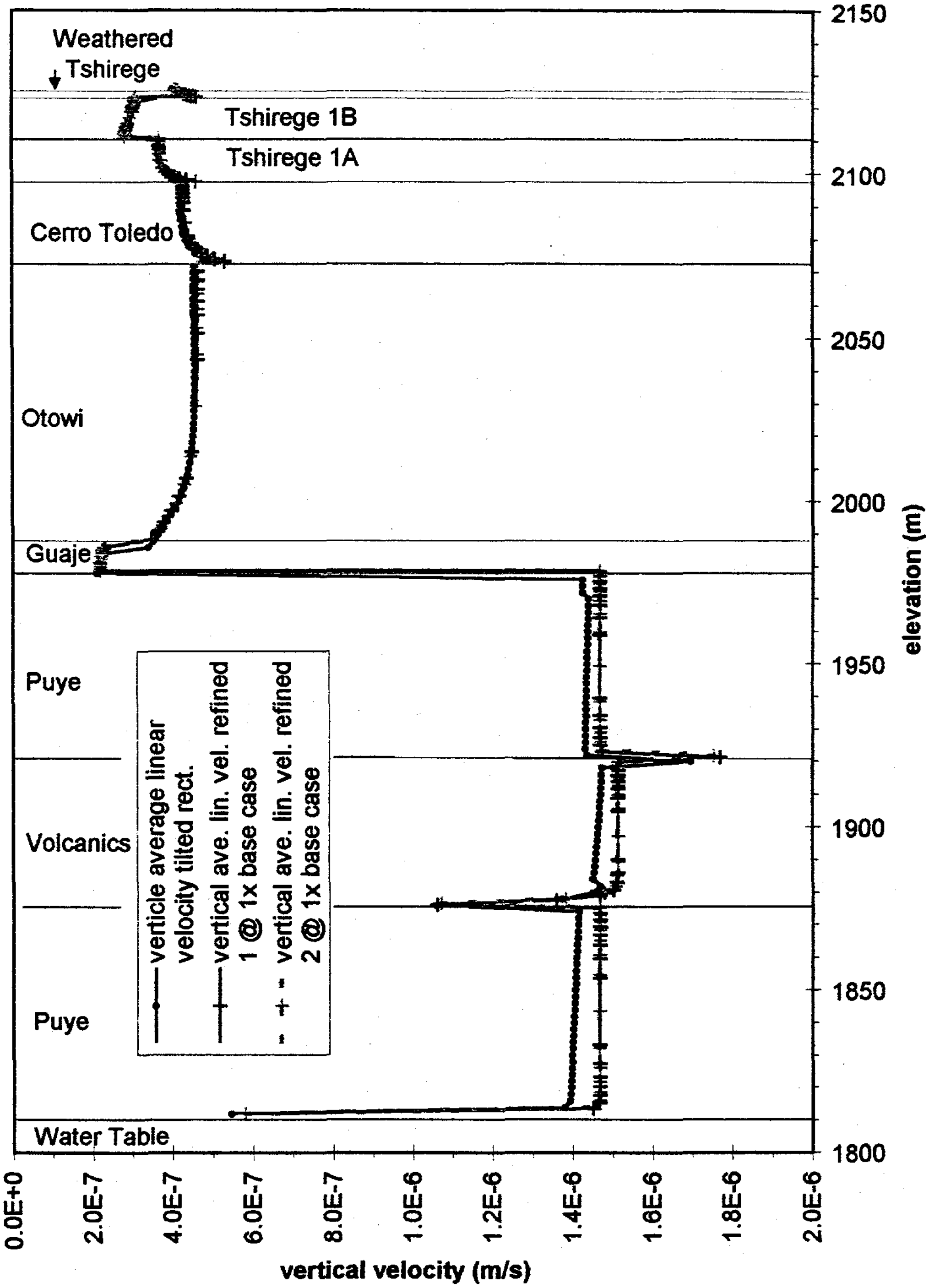

Figure 5.15 Vertical average linear velocity depth profile at center of each grid.

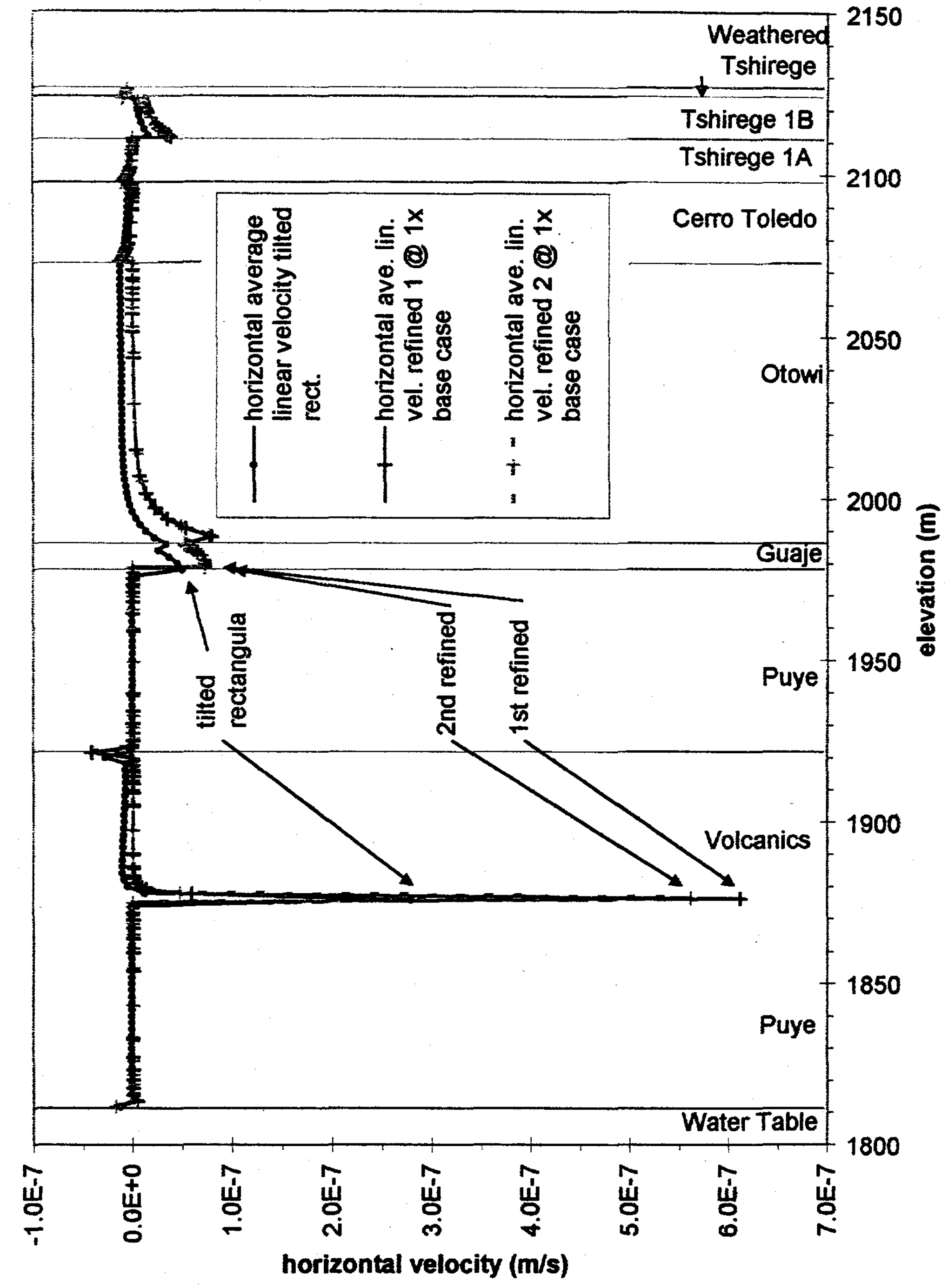

Figure 5.16 Horizontal average linear velocity depth profile at center of each grid.

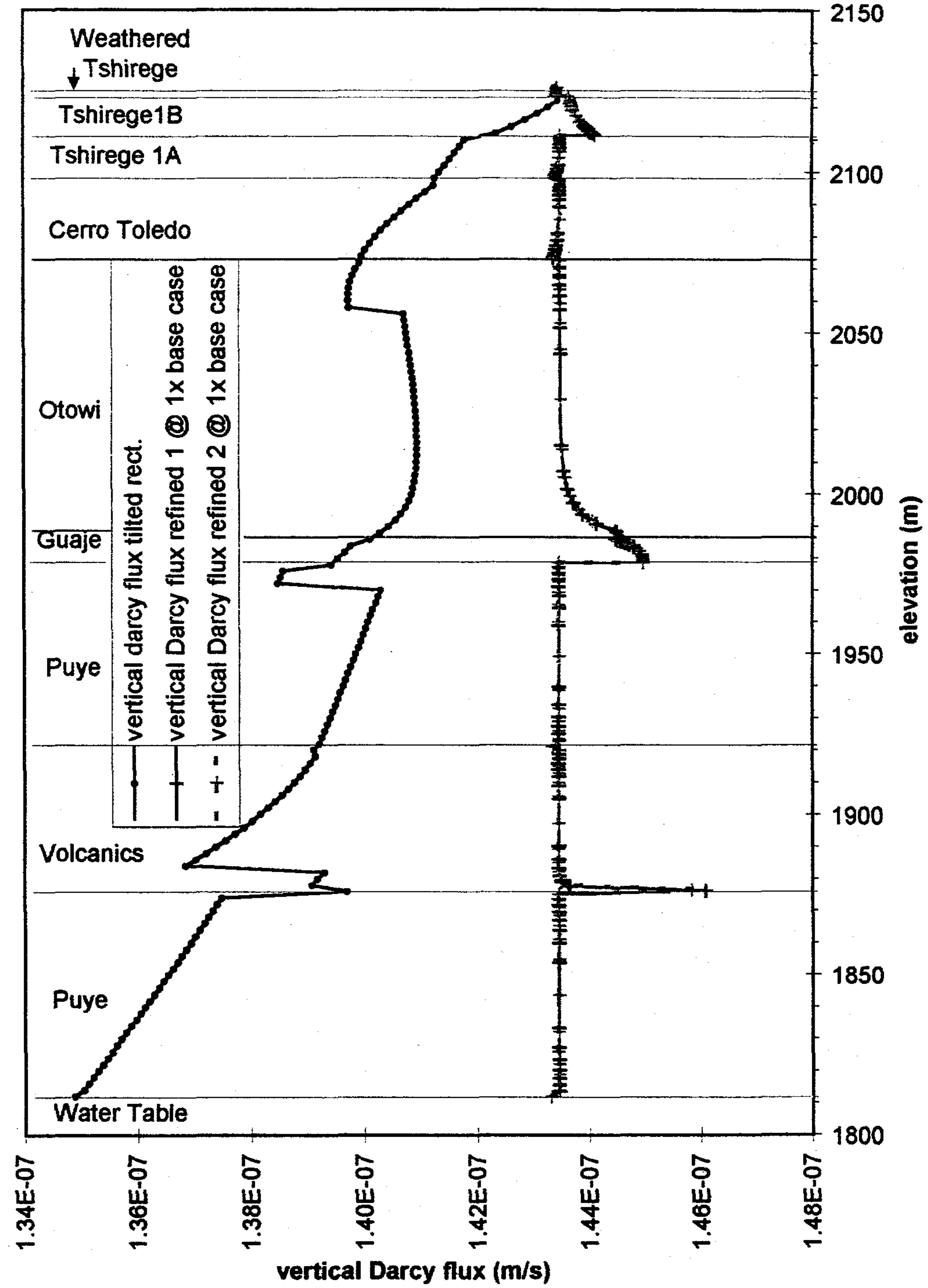

Figure 5.17 Vertical Darcy flux depth profile at center of each grid.

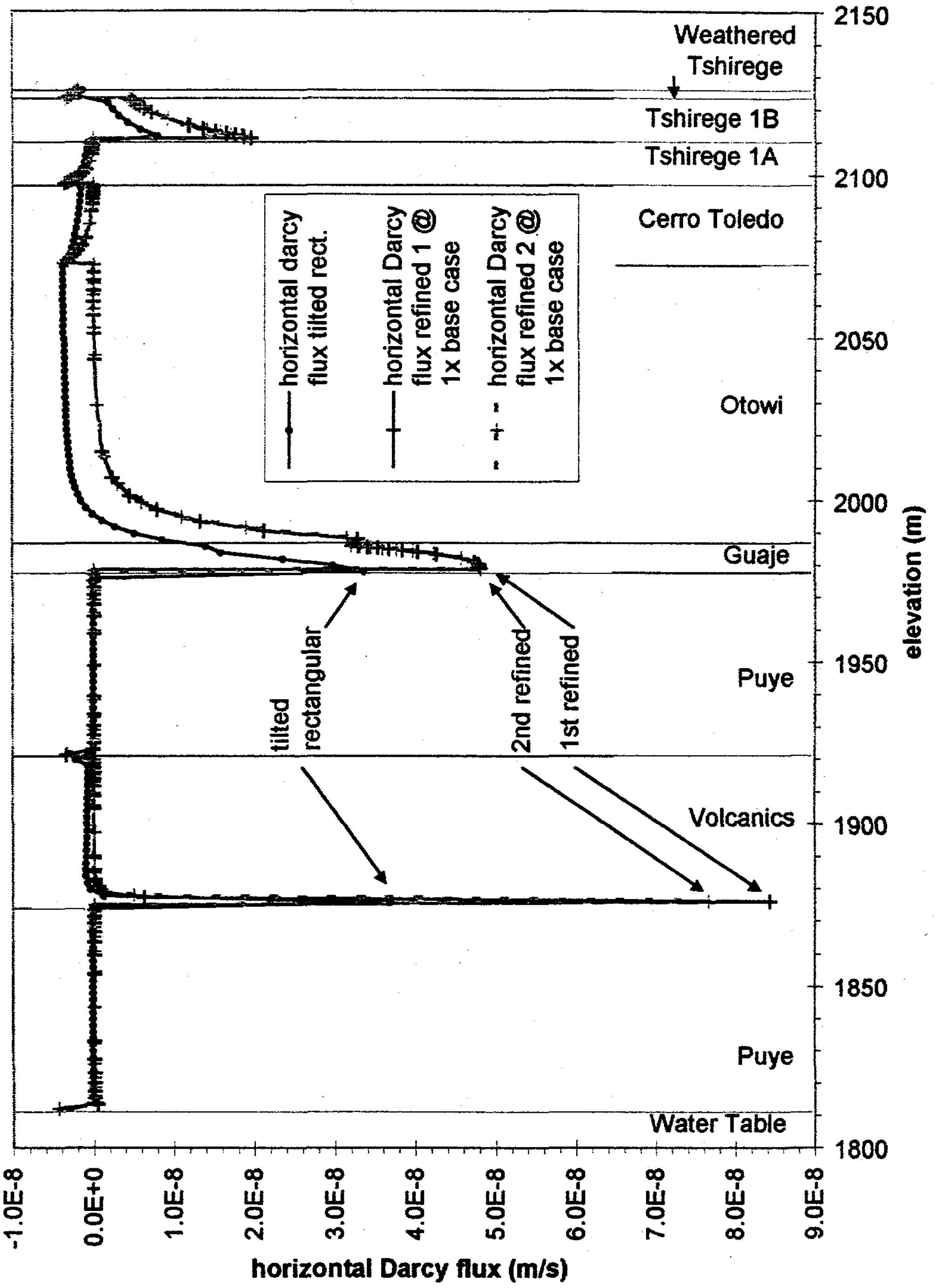

Figure 5.18 Horizontal Darcy flux depth profile at center of each grid.

Pressure, saturation, vertical Darcy flux, and horizontal Darcy flux for each node in the domain are plotted relative to their horizontal position in Figures 5.19, 5.20, 5.21, and 5.22. As in similar plots from simulation 2, some sets of nodes along the same row in the grid have been connected to illustrate their variability next to a horizontal line for comparison. Flow values are relatively constant on each of these plots between 120 m and 320 m on the X-axis. Although horizontal variation in flow results is still present in the domain, the effect from the side boundary conditions discussed in section 5.3 dies out approximately 50 m from the sides.

The maximum difference in vertical Darcy fluxes along the same row 16 m from center (horizontal distance particles travel at this recharge rate) was less than 1.0E-12 or 0.0007%, compared to the 26.7% seen in simulation 2. Additionally, the maximum difference in horizontal Darcy fluxes along the same row 16 m from center was less than 1.4E-12 or 0.005%, compared to the 63.5% seen in simulation 2. The maximum difference in pressures along the same row 16 m from center was less than 0.000007 Mpa, compared to .0043 seen in simulation 2. The maximum difference in saturation along the same row 16 m from center was less than 0.00001%, compared to the 1.46% seen in simulation 2. Comparison of these maximum differences illustrates how the side effects are now restricted to the part of the grid near the side boundary. Nodes towards

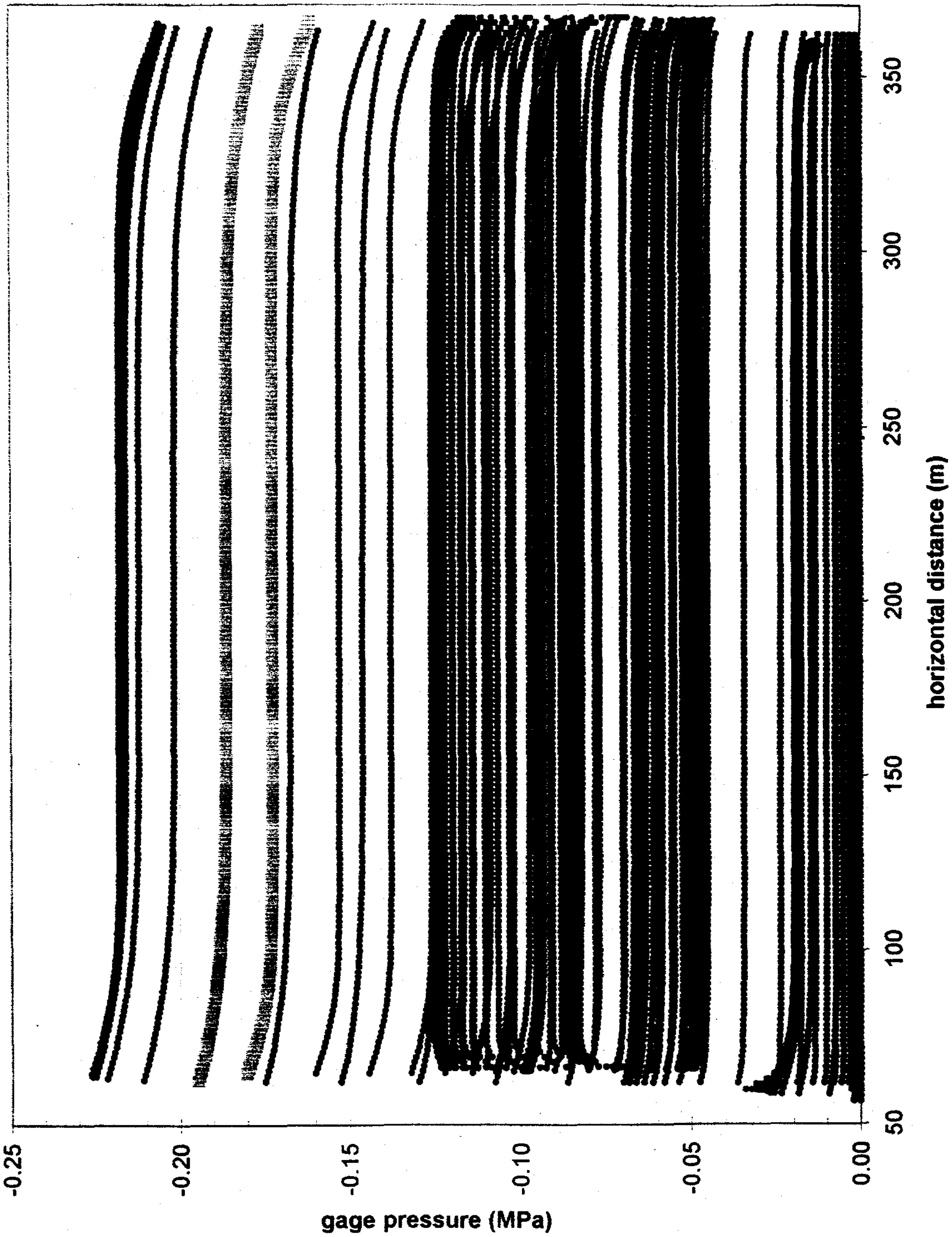

Figure 5.19 Pressure at each node in the First Refined Tilted Rectangular Grid simulation with respect to horizontal position.

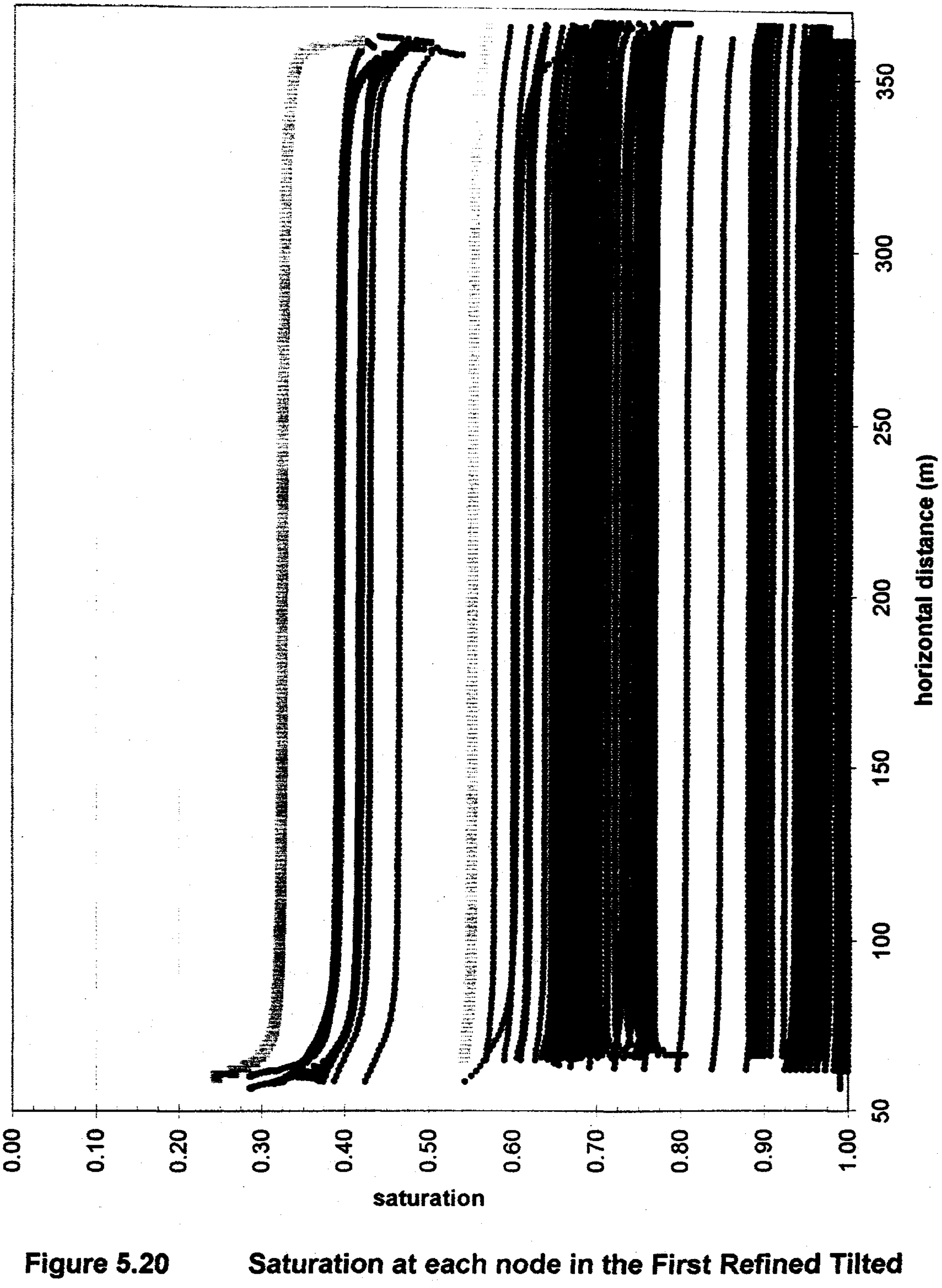

Figure 5.20 **Saturation at each node in the First Refined Tilted Rectangular Grid simulation with respect to horizontal position.**

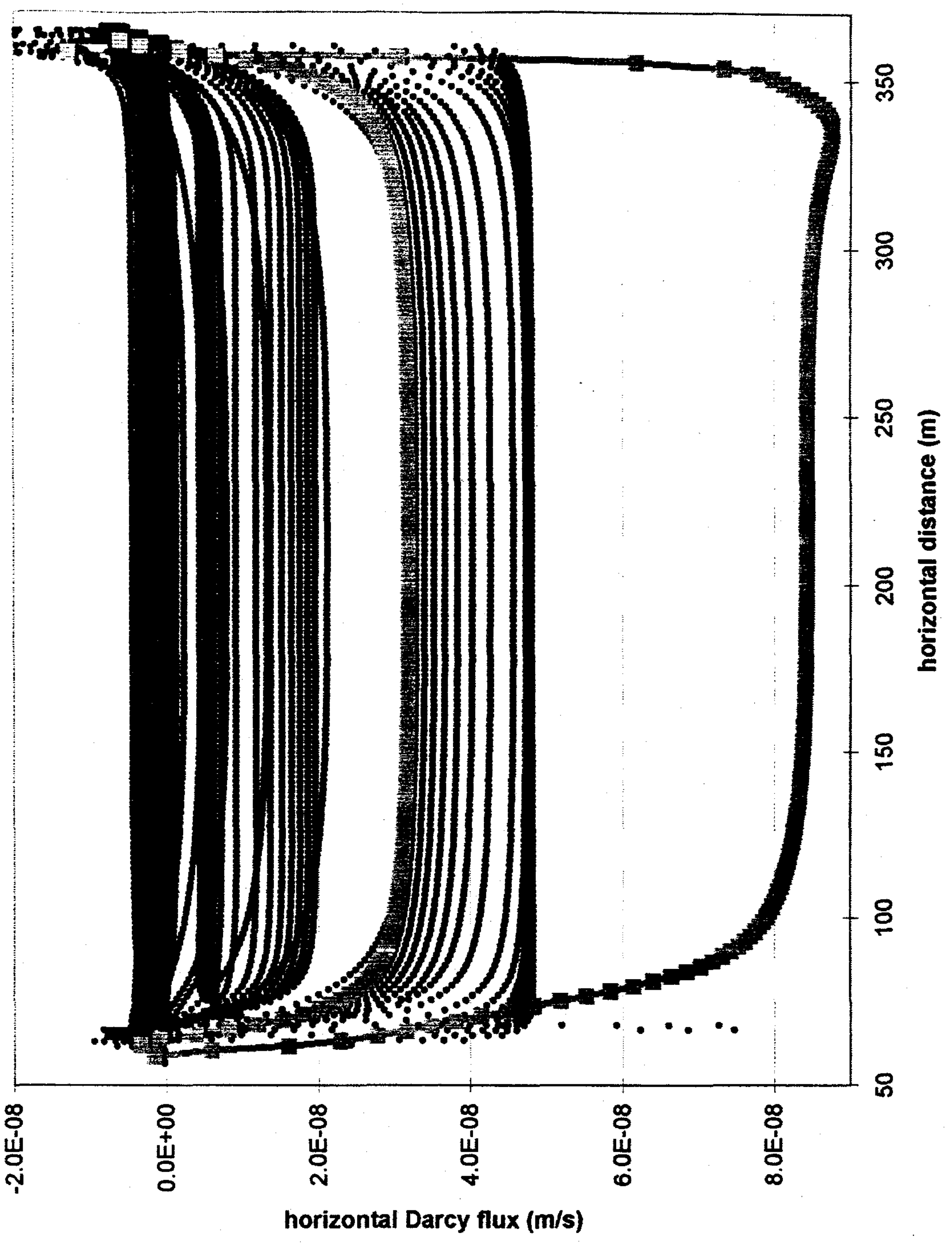

Figure 5.21 Horizontal Darcy flux at each node in the First Refined Tilted Rectangular Grid simulation with respect to horizontal position.

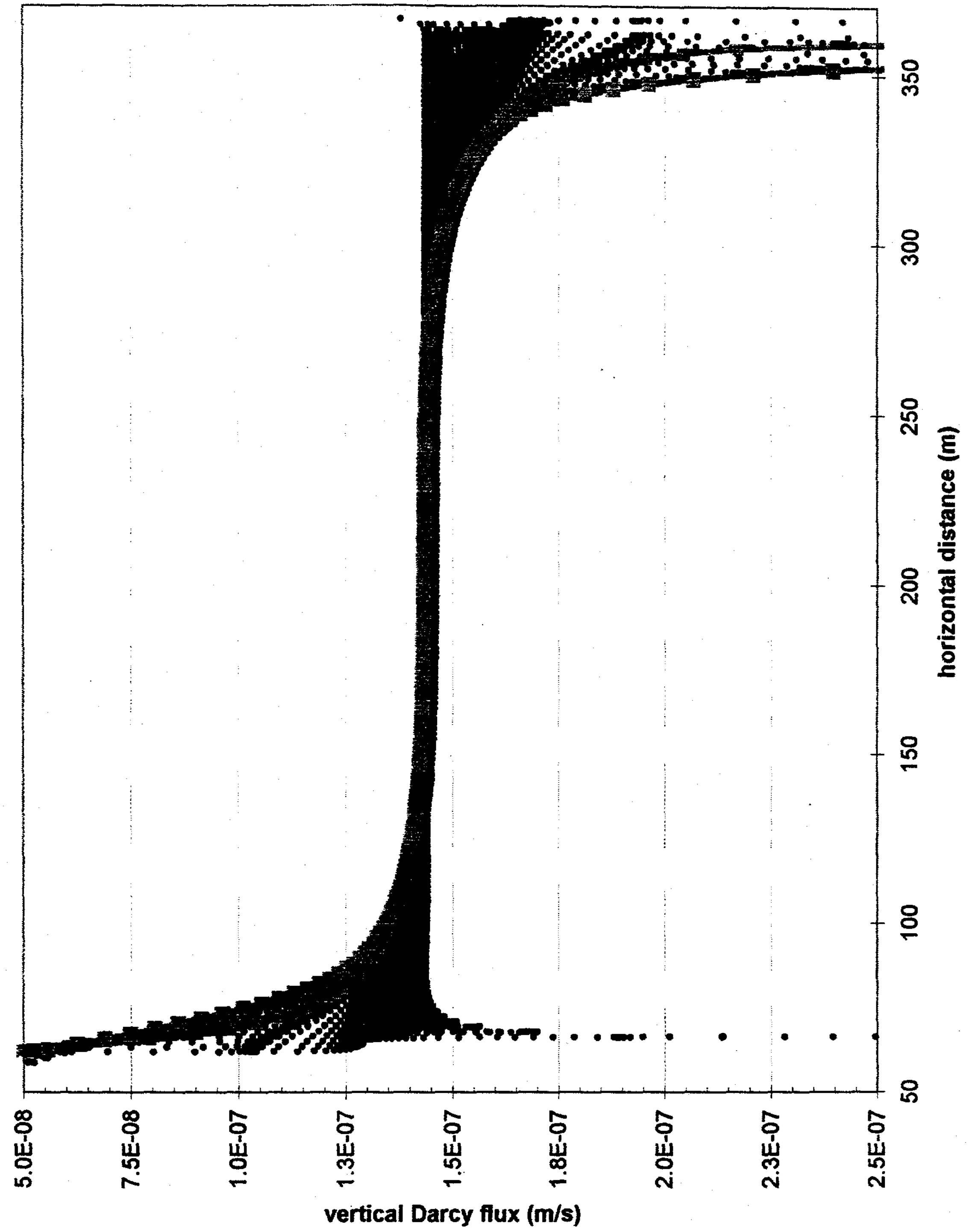

Figure 5.22 Vertical Darcy flux at each node in the First Refined Tilted Rectangular Grid simulation with respect to horizontal position.

the center are free of horizontal variation in flow rates. Although side boundary effects are minimal, the spread in travel times is much greater than simulation 2. This is due to the particles having to take longer paths between nodes, and is a result of grid size.

Effects from side boundary conditions were reduced in this wider grid. The effects on flow velocity from the no-flow side boundary conditions are limited to a zone of about 50 m from each side, and should be excluded from particle tracking and other interpretations. Nodes outside those zones were used for particle tracking, and nodes at the center were used to plot flow results.

Using the flow solution from this refined grid simulation, a particle tracking simulation was performed. The particle tracking was done in the same manner as with the previous simulations. Results from the particle tracking simulation are plotted as a breakthrough curve at the lower boundary and labeled as First Refined in Figure 5.6. The breakthrough curve for this simulation shows the mean of the particles reaching the regional aquifer in approximately 13.8 years, sooner than all previous simulations. These arrival times are sooner than simulation 2 due to the greater vertical velocities observed when side boundary conditions did not influence the transport solution. The spread in arrival times caused by different paths was greater than simulation 2 because the horizontal velocities were greater and particle paths through the system were more variable in lengths. The horizontal distance traveled by particles by the time they reach the regional aquifer was again approximately 16 m.

5.5. SECOND REFINED TILTED RECTANGULAR GRID NUMBER 4, SIMULATION 4

To assess if the previous simulation, (number 3) was adequately discretized, another simulation was performed with a slight increase in the vertical grid spacing to see if the solution was affected. Finer vertical grid spacing was not used because grid aspect ratios became too great, causing code convergence problems. Properties of the Second Refined Tilted Rectangular Grid (number 5) are listed in Table 5.1 and is shown in Figure 5.23. Horizontal node spacing is always 1.5 m. Each lithologic unit included 14 rows of nodes, 2 less per unit than grid number 3. The spacing decreased in height by a factor of 1/2 towards the lithologic interfaces. Minimum node spacing at the thinnest lithologic unit interface was 0.08 m. Vertical grid spacing was slightly coarser, while horizontal spacing remained the same. The stratigraphy and all other code parameters were the same as previous simulations.

Flow results from the horizontal center of the grid are also plotted as depth profiles in Figures 5.13-5.18.

The pressure and saturation profiles in figures 5.13 and 5.14 appeared to be the same as in simulation 3. Average saturations in the Puye are about 39% and about 42% in the volcanics. Those saturations peak to 62% at the base of the volcanics and dip to 33% at the base of the upper Puye unit. Saturations increase with depth from 78% to 97% in the Tshirege Unit 1B, from 65% to 88% in the Otowi Formation then continue increasing

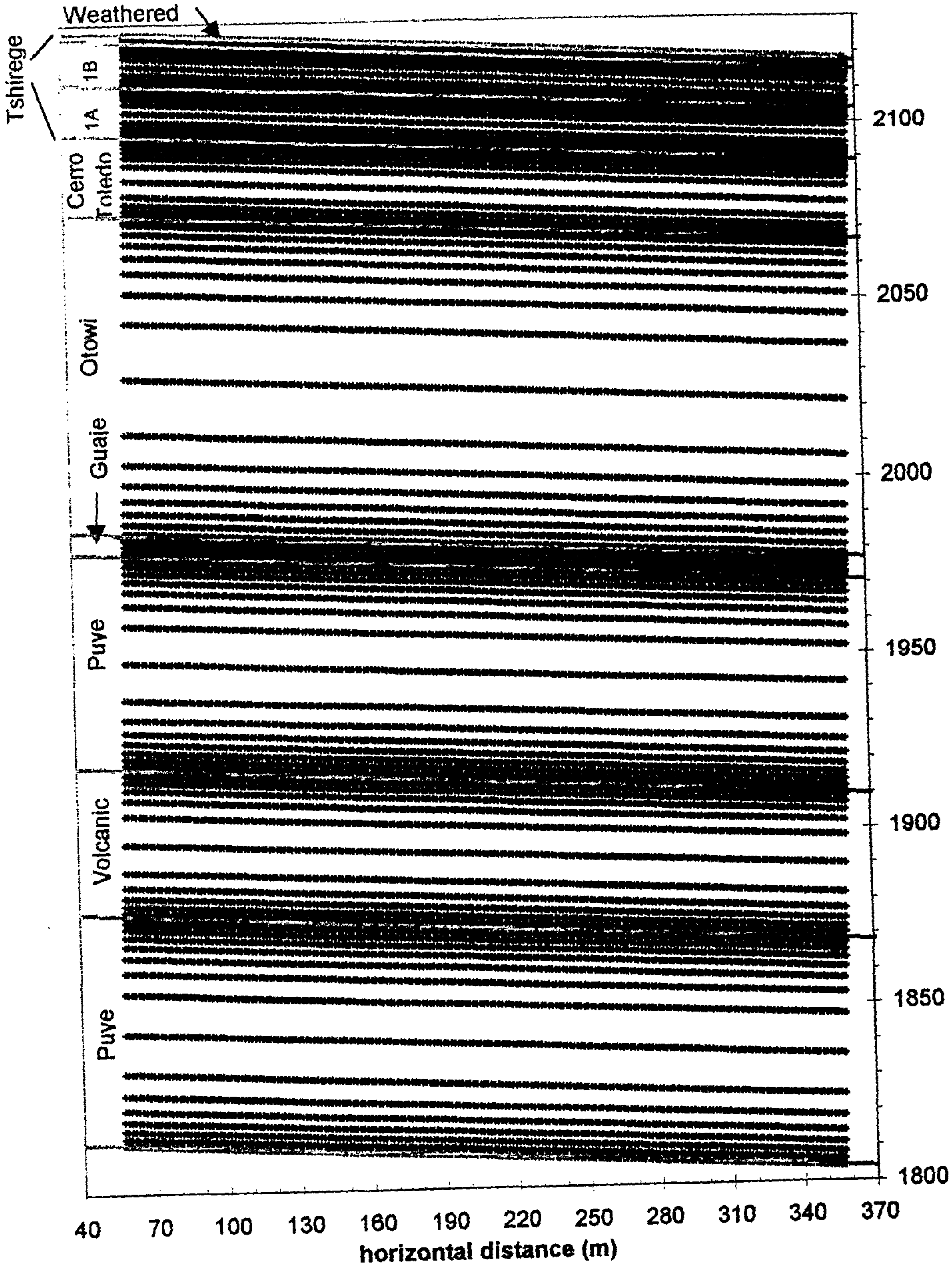

Figure 5.23 Node locations at corners of each rectangular element in Second Refined Grid, with about 2:3 vertical exaggeration.

up to 100% in the Guaje Pumice Bed. Saturations decrease with depth from 77% to 69% in the Weathered Tshirege, from 77% to 62% in the Tshirege Unit 1A, and from 69% to 56% in the Cerro Toledo Interval. Values tend to peak and dip at lithologic interfaces except for the base of the Otowi Formation which seems to be unaffected.

For the most part, average linear velocities and Darcy flux depth profiles appeared to be the same as in simulation 3, except for a slight variation at the top and bottom of the volcanics (Figures 5.15-5.18). Maximum horizontal velocities occur in a thin zone at the base of the Basalt/Tschicoma unit. In simulation 3, these velocities were over twice as high as those in simulation 2. Now in simulation 4 they are within 8% of those velocities in simulation 3. Maximum vertical velocities occur in a thin zone at the base of the upper Puye unit. In simulation 3, they were 5% higher than those in simulation 2. Now, in simulation 4 they are within 1% of those velocities in simulation 3. These maximum differences occurred within a single very thin zone and overall effect on the system were minimal. Therefore, grids numbered 3 and 4 were assumed adequately discretized and used for further simulations that varied certain parameter, because of the close match in simulation results.

5.6. GRID NUMBER 3 WITHOUT BASALT, SIMULATION 5

Earlier it was noted that the horizontal extent of the Tschicoma Formation and the Unit 2 Basalt are not known. The longitudinal section in Figure 3.6 shows both units pinching out near the center. In the previous simulations, these unit were treated as one and was continuous across the simulation domain. In this section, the simulation illustrates the effects when that unit is not present.

This simulation (number 5) was the same as the First Refined Tilted Grid simulation (number 3), except that nodes previously assigned fractured Unit 2 Basalt/Tschicoma material properties were assigned those of the Puye Formation.

Flow results were the same as in simulation 3 with the exception of pressures, saturations, and velocities throughout the Puye Unit. Previous simulations modeled the lower half of the domain as three separate units. With the removal of the volcanics and related lithologic contacts, flow results are now constant within the Puye Unit. Flow results are not presented as plots because of its simplicity; imagine drawing a straight line downward connecting data from the centers of the upper and lower Puye units in Figures 5.13-5.18.

Using the flow solution a particle tracking simulation was performed. The breakthrough curve labeled “First Refined with no Basalt” in Figure 5.6 shows the mean of the particles reaching the regional aquifer in approximately 14.8 years. This is approximately 1 year or 7% longer than the travel time when the volcanics were present. This simulation illustrates the overall effect of representing fractures in the system. However, specific fracture flow information was not acquired because the effective continuum approach (weighted average of matrix and fracture material properties) was used.

5.7. VARYING UPPER BOUNDARY FLUX WITH GRID NUMBER 3

5.7.1. Variations in Recharge Magnitude Simulations 6-9

Each of the water budget components used to calculate recharge have uncertainty associated with them. Therefore, recharge inherits uncertainties of all the components. Knowledge of system behavior with various recharge is important for predicting potential contaminant pathways and rates of movement when those recharge conditions apply. Discussion that follows shows how the system reacts to recharge higher and lower than the water budgets base case estimate. Evenly distributed recharge across the upper boundary of 2, 1/2, 1/10, and 1/100 times the base case are examined. The 2 times the base case recharge scenario was examined to represent the system behavior during wetter periods. The lower recharge scenarios (1/2, 1/10, and 1/100 times base case) were examined to explore the system behavior during dryer periods as well as in dryer portions of the canyon and away from the canyon axis. Birdsell et al. (1997) estimated recharge under mesa tops to be less than the 1/100 times this base case. Figure 5.24 is a plot showing these constant recharge values as well as an increasing and decreasing function discussed in section 5.7.2.

Simulations were performed in the same manner as all other simulations using grid number 3; with the exception of changes to the amounts of recharge used at the upper boundary nodes.

Results for each recharge condition are plotted as depth profiles in Figures 5.25, 5.26, 5.27, 5.28, and 5.29.

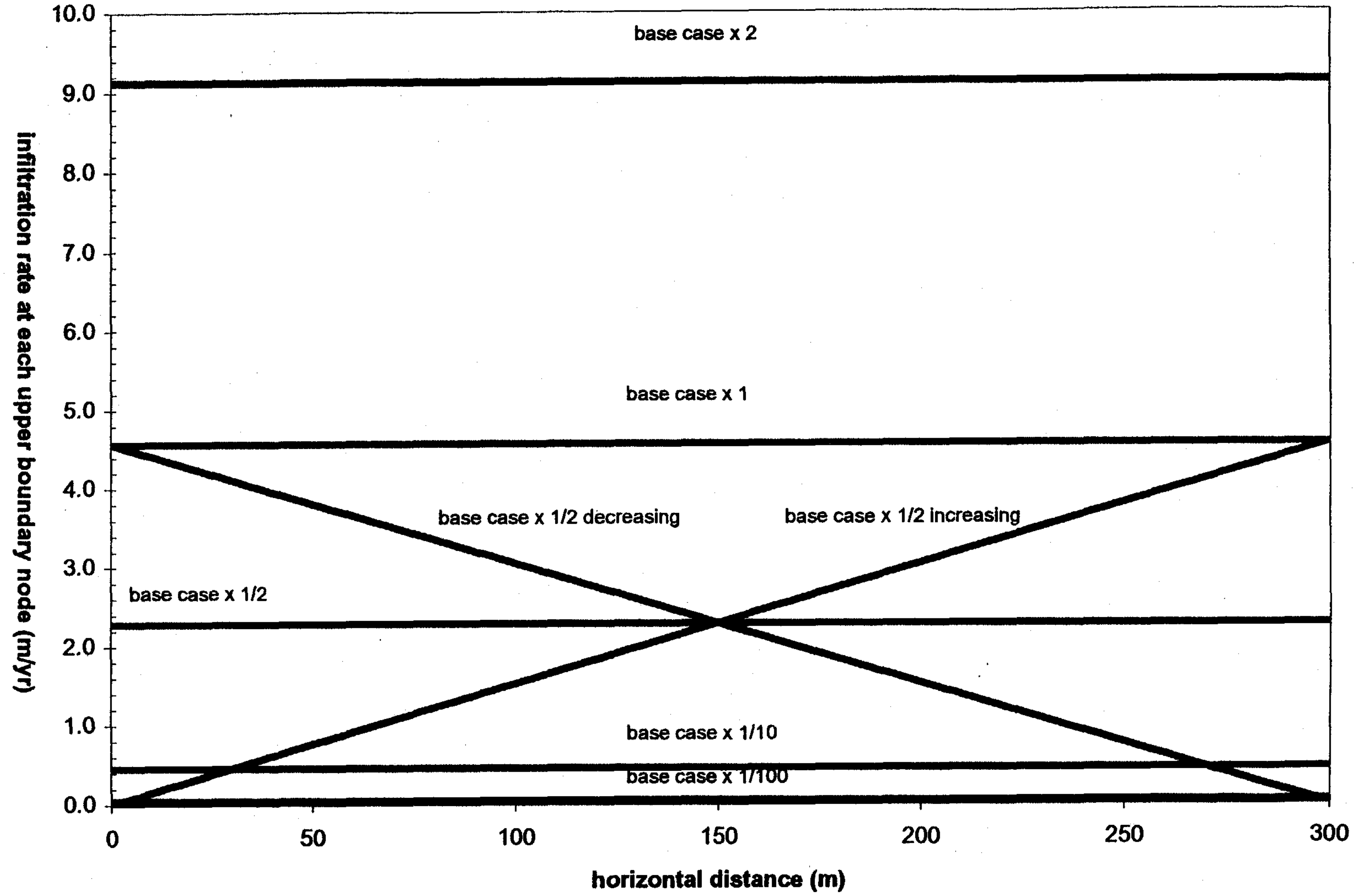

Figure 5.24 Infiltration distributions across upper boundary of grid.

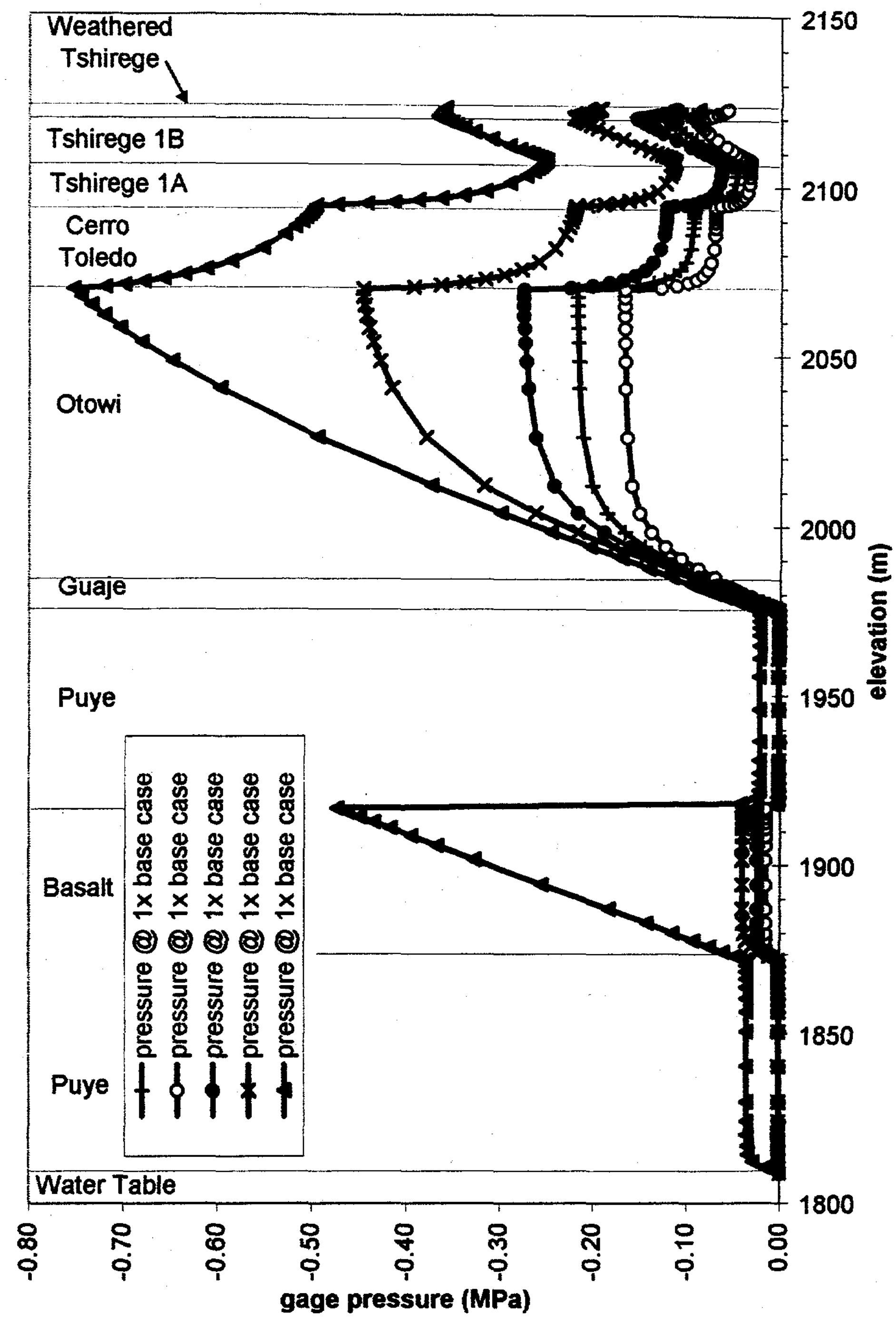

Figure 5.25 Pressure profiles for variable recharge conditions on First Refined Grid.

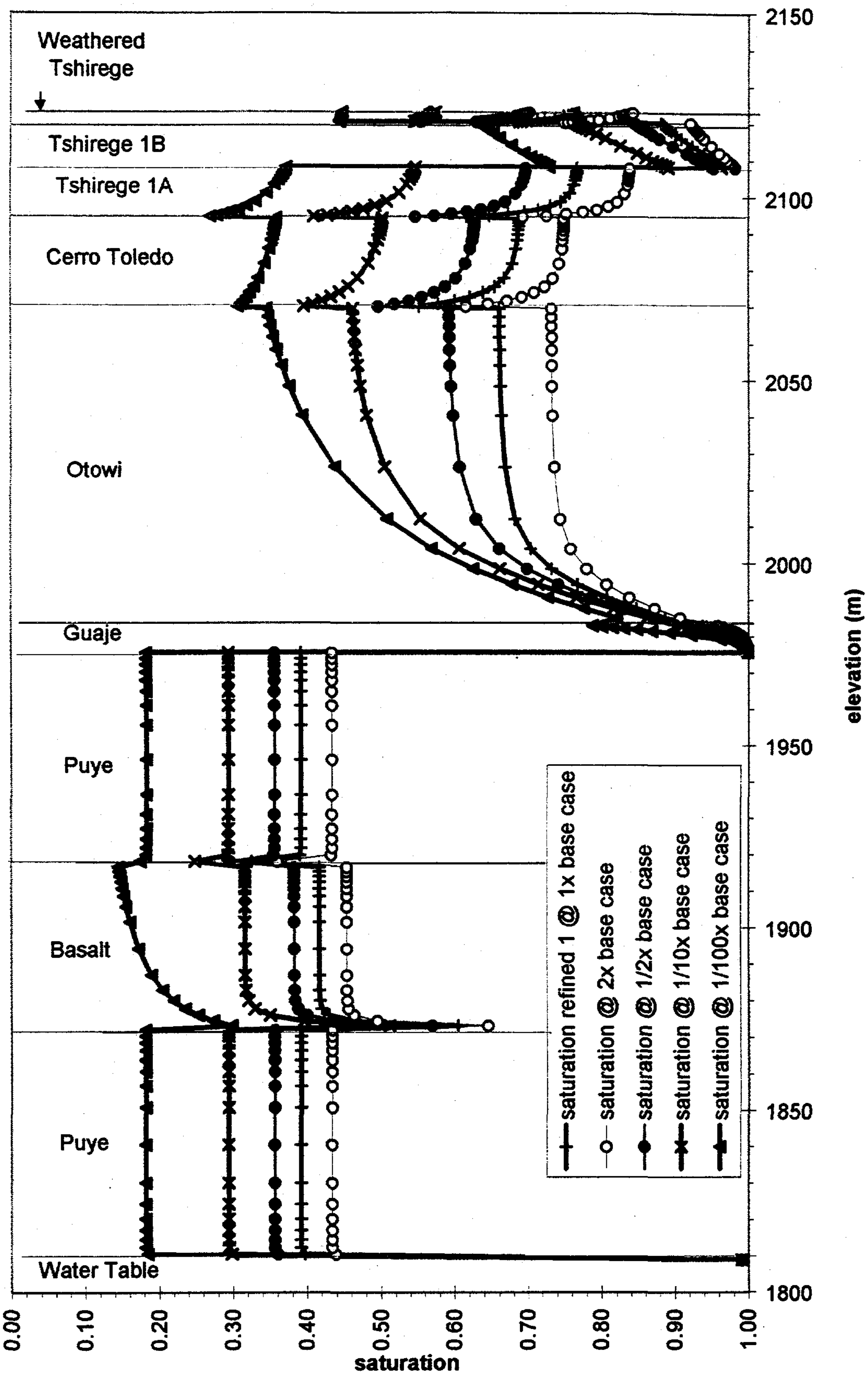

Figure 5.26 Saturation depth profiles for variable recharge conditions on First Refined Grid.

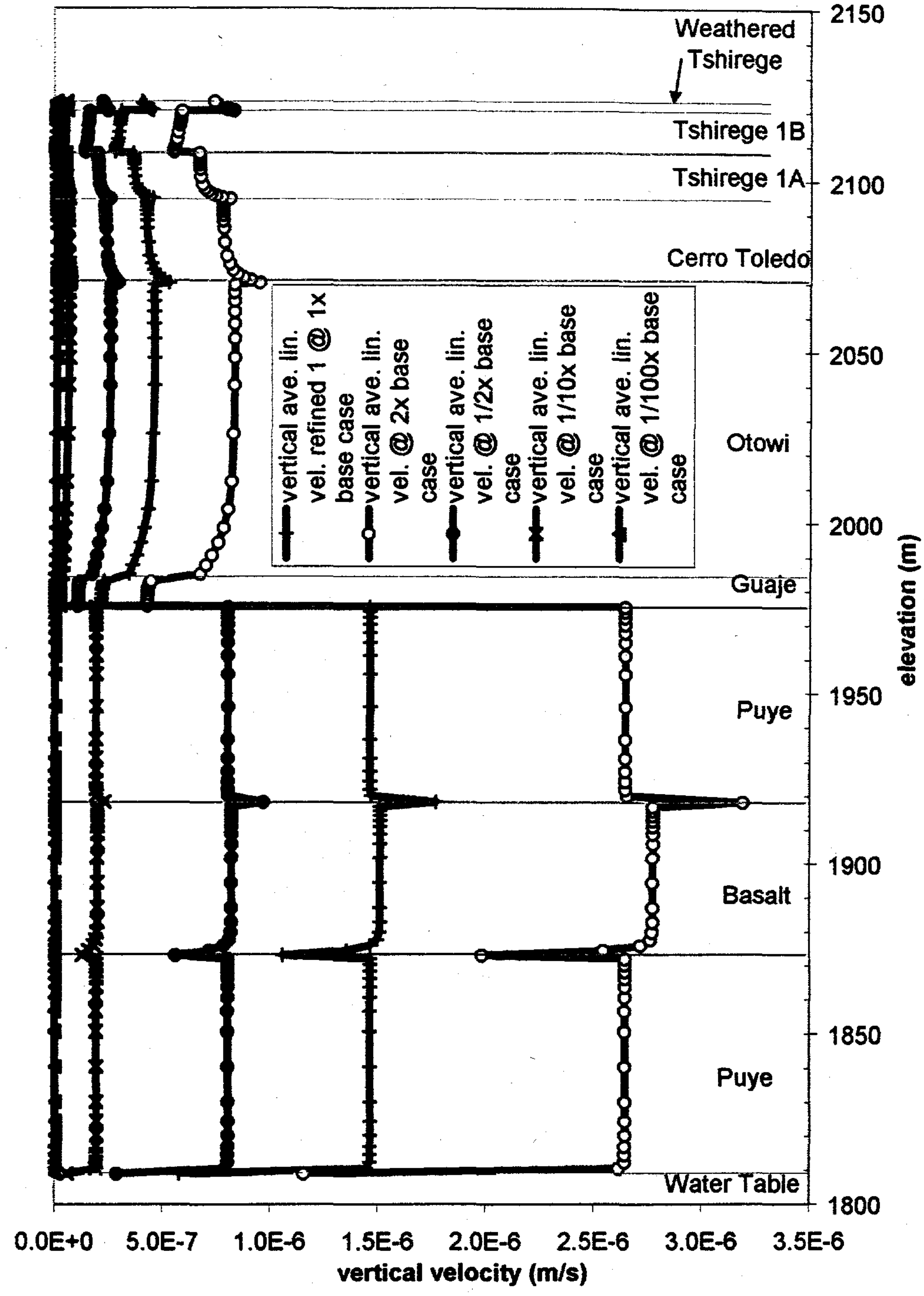

Figure 5.27 Vertical average linear velocity depth profiles for variable recharge conditions on First Refined grid.

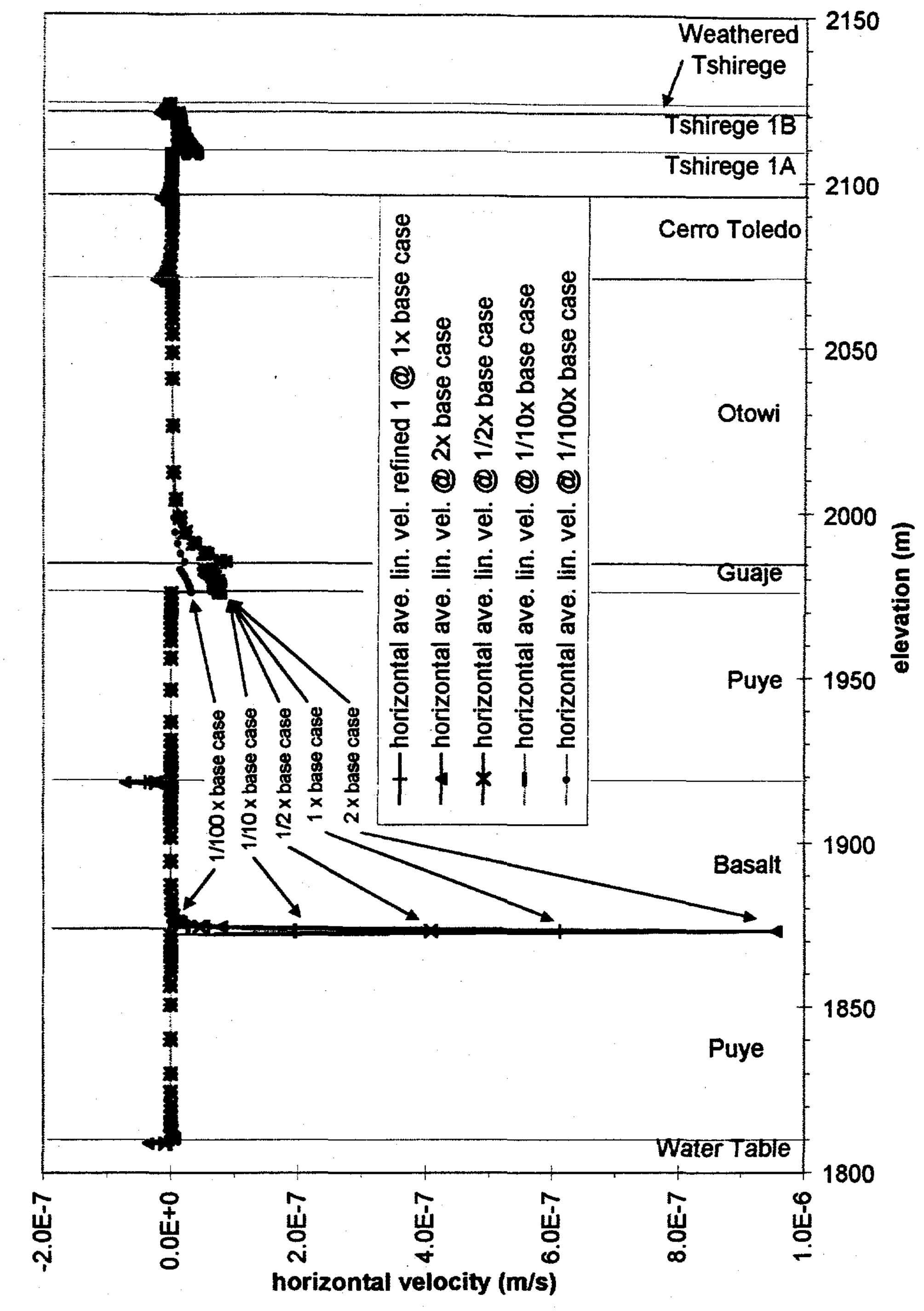

Figure 5.28 Horizontal average linear velocity depth profiles for variable recharge conditions on First Refined Grid.

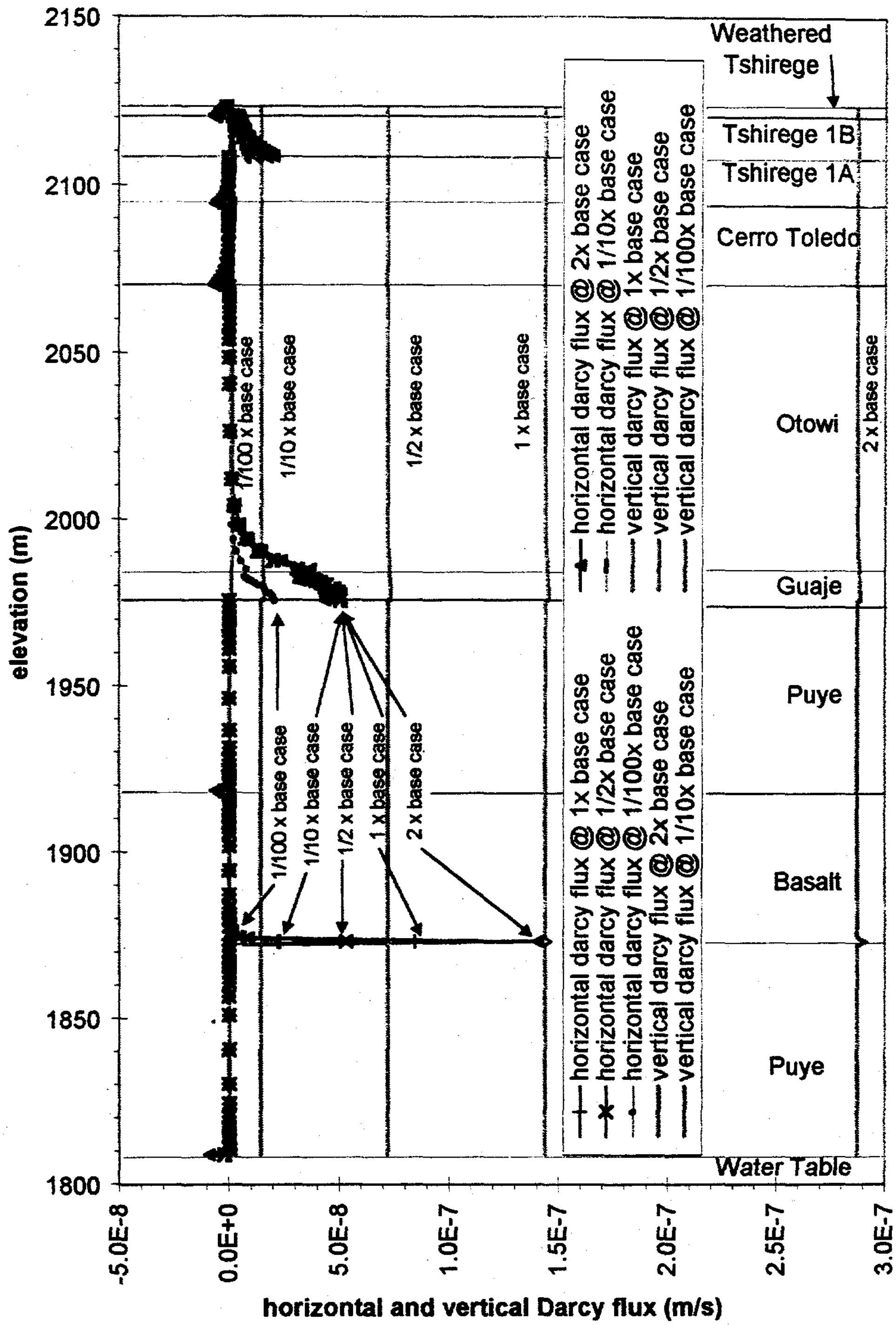

Figure 5.29 Horizontal and Vertical Darcy flux profiles for variable recharge conditions on First Refined Grid.

Many of the same solution trends observed in simulation 3 occur with variation in recharge, but at different magnitudes. One effect to note from Figures 5.25 and 5.26 is that pressures in the Puye and volcanics appear to be atmospheric (0.1 MPa), yet very slight change in pressure causes a large change in saturation following the steep slope seen on the moisture characteristic curve (Figure 3.3A-B). Another effect of importance is that saturation always occurs at the base of the Guaje Pumice Bed. The Otowi Formation supports the largest range of pressures and saturations with each recharge applied. The 1/100 times the base case recharge scenario produces a somewhat different but valid distribution behavior in the volcanics in both the pressure and saturation depth profiles in figures 5.25 and 5.26.

At the base of the volcanics where horizontal velocities are at their greatest, variations in recharge caused the following to occur in relation to the base case scenario: Applying 2 times the recharge caused a 56% increase in velocity; 1/2 times the recharge caused a 33% reduction in velocity; 1/10 times the recharge caused a 68% reduction in velocity; 1/100 times the recharge caused a reduction in velocity well below .01%. At the base of the upper Puye where vertical velocities are at their greatest, variations in recharge caused the following to occur in relation to the base case scenario: Applying 2 times the recharge caused a 87% increase in velocity; 1/2 times the recharge caused a 53% reduction in velocity; 1/10 times the recharge caused a 88% reduction in velocity; 1/100 times the recharge caused a reduction in velocity well below .001%. One can see from the percentages above that the effect from changing recharge on vertical velocities is greater than the effect on horizontal velocities. Hence, at very low recharge rates, such as 1/10 and 1/100 times the base case, horizontal flow can exceed vertical flow throughout the Guaje Pumice Bed, and at the base of the Otowi, volcanics, and Tshirege 1B units. This is due to a large hydraulic conductivity difference at the lower contact.

Using the flow solutions from these simulations numbered 6-9, particle tracking simulations were performed. The particle tracking technique was used in the same manner as in the previous first refined grid simulation, except for the location where particles were injected. For the 1/10 and 1/100 times the base case recharge simulations, particles were injected up-gradient from the center, to keep them from migrating laterally into a zone influenced by the side boundary conditions. The times in years required for each of the particles to reach the regional aquifer are indicated in a breakthrough curve in Figure 5.30 for each recharge applied.

Mean particle breakthrough times at the lower boundary using 2, 1, 1/2, and 1/10 times the base case recharge values were 7.6 years, 13.8 years, 26.2 years, and 109.5 years, respectively. Differences in arrival times for each simulation increases with decreasing recharge rates. This is because some particles move further horizontally and the range of distance traveled is greater. With 1/100 times the base case recharge scenario, particles are expected to reach the regional aquifer after 1400 years, based on the few particles that traveled through the system away from the zone of influence from the side boundary.

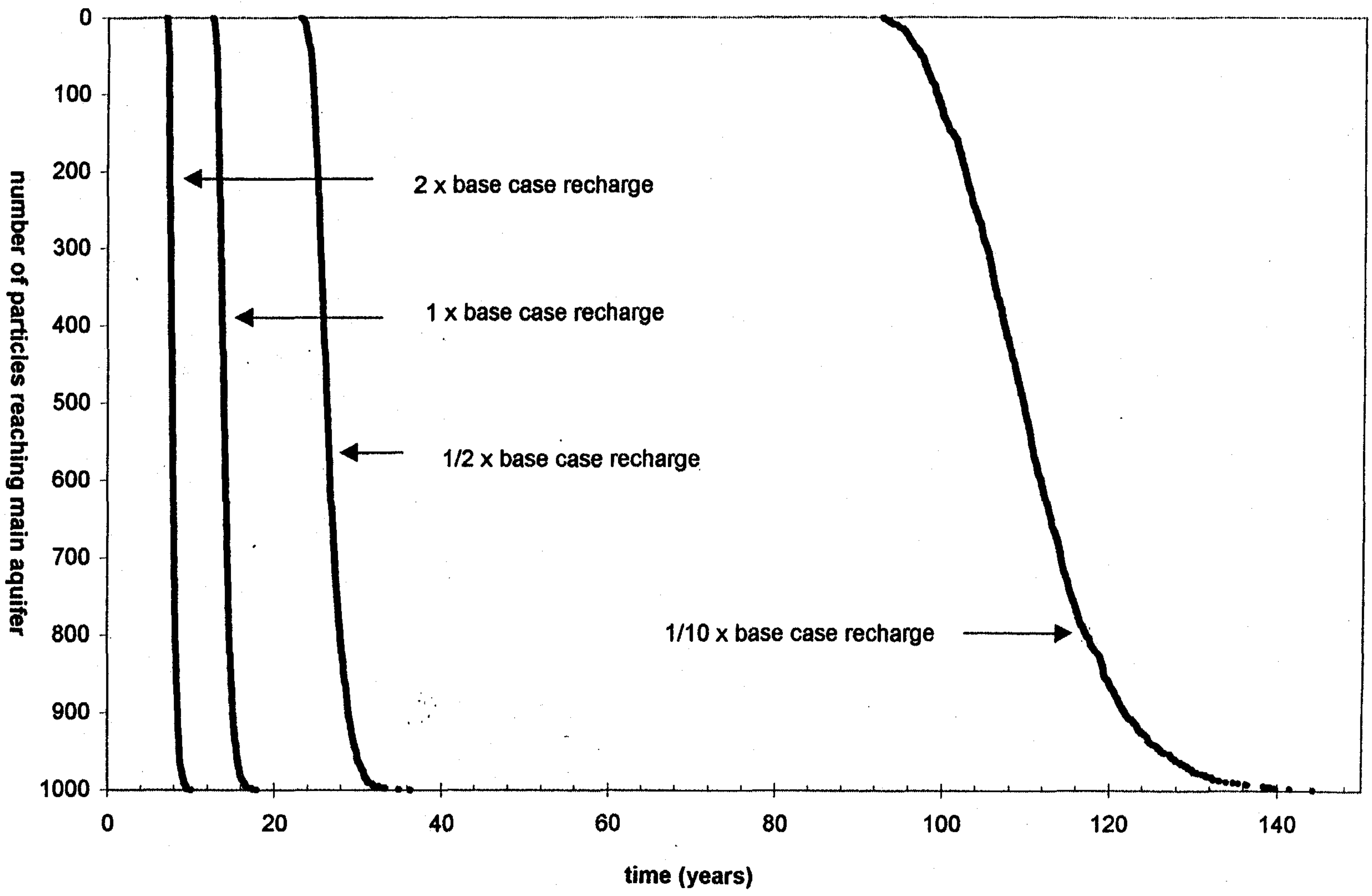

Figure 5.30 Breakthrough curves for variable recharge conditions.

Results from the particle tracking simulation are also plotted as snapshots representing particles in Figures 5.31, 5.32, 5.33, 5.34, and 5.35 moving through the system at specified times for each recharge senerio. Contours encompassing groups of nodes in the domain with one or more particles are shown at specific times since entering the system. For each plot, several times are presented and vary for each figure to illustrate particle movement throughout the domain without overlap. Particles are not seen in the Basalt/Tschicoma because the fluid volume containing the particles is small due to the low saturation and porosity in the fractures and matrix. The figures show greater spreading (both horizontally and vertically) and rate of particle movement in the lower units (Puye, Basalt/Tschicoma, and Guaje) than in the upper units (Otowi, Cerro Toledo, and Tshirege). This is attributed to the difference in average linear velocities between the upper and lower units.

When recharge was decreased the lateral distance particles traveled increased. In the case of the 1/100 times the base case recharge, in Figure 5.35, particles reached the Guaje Pumice Bed, moved across the grid, and down the other side. This plot does not illustrate particle breakthrough at the lower boundary correctly, because the particles entered the zone influenced by side boundary effects. What this figure does illustrate is horizontal flow at very low recharge fluxes within the Guaje Pumice Bed. The existence of horizontal flow could be important to contaminant pathways. The results suggest that contaminants could travel large distances within the Guaje Pumice Bed, but at very slow rates. Especially in situations such as attempting to find contamination during

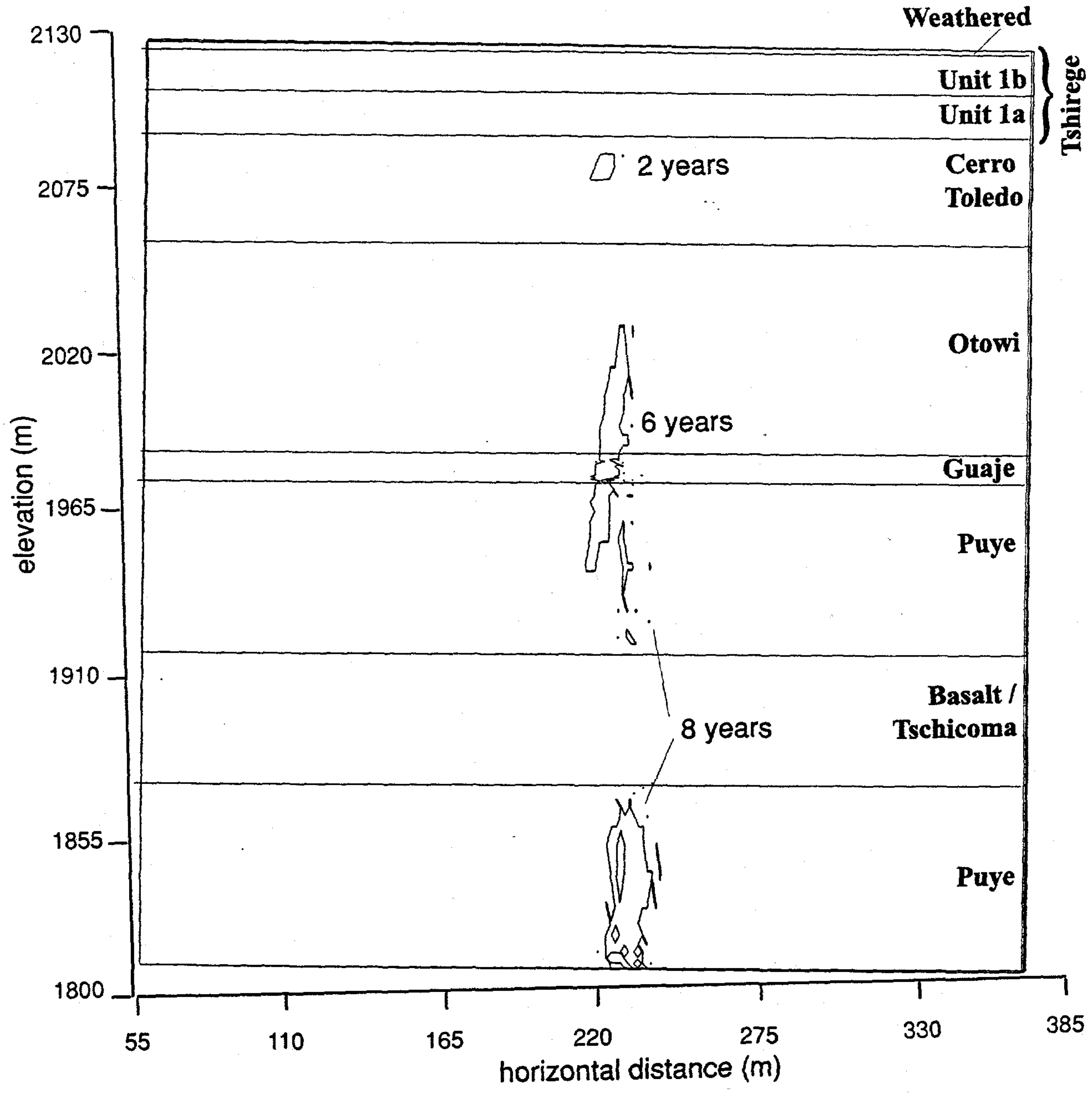

Figure 5.31 **Particle distributions for 2 x base case recharge simulation through First Refined Rectangular Grid.**

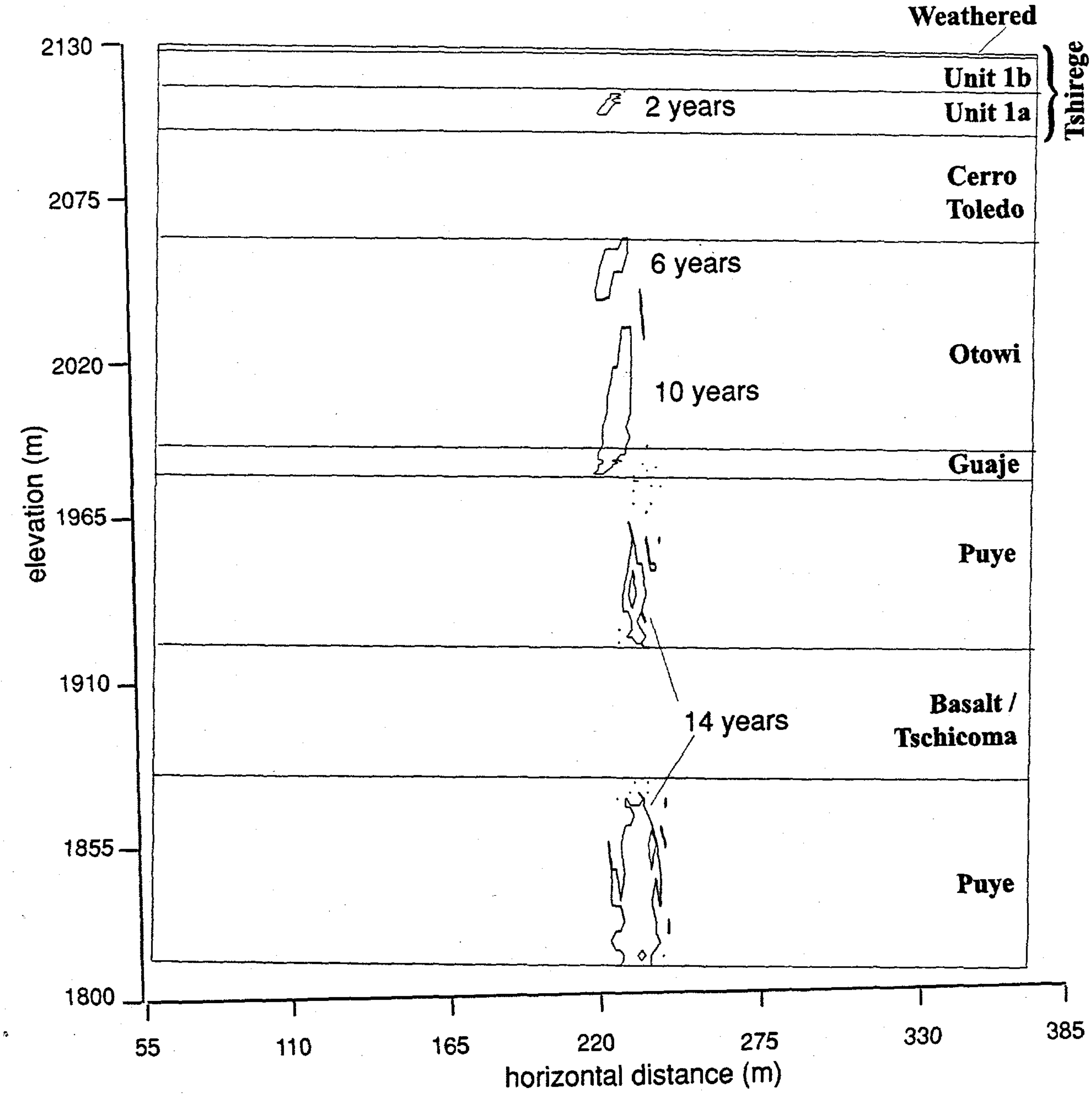

Figure 5.32 **Particle distributions for 1 x base case recharge simulation through First Refined Rectangular Grid.**

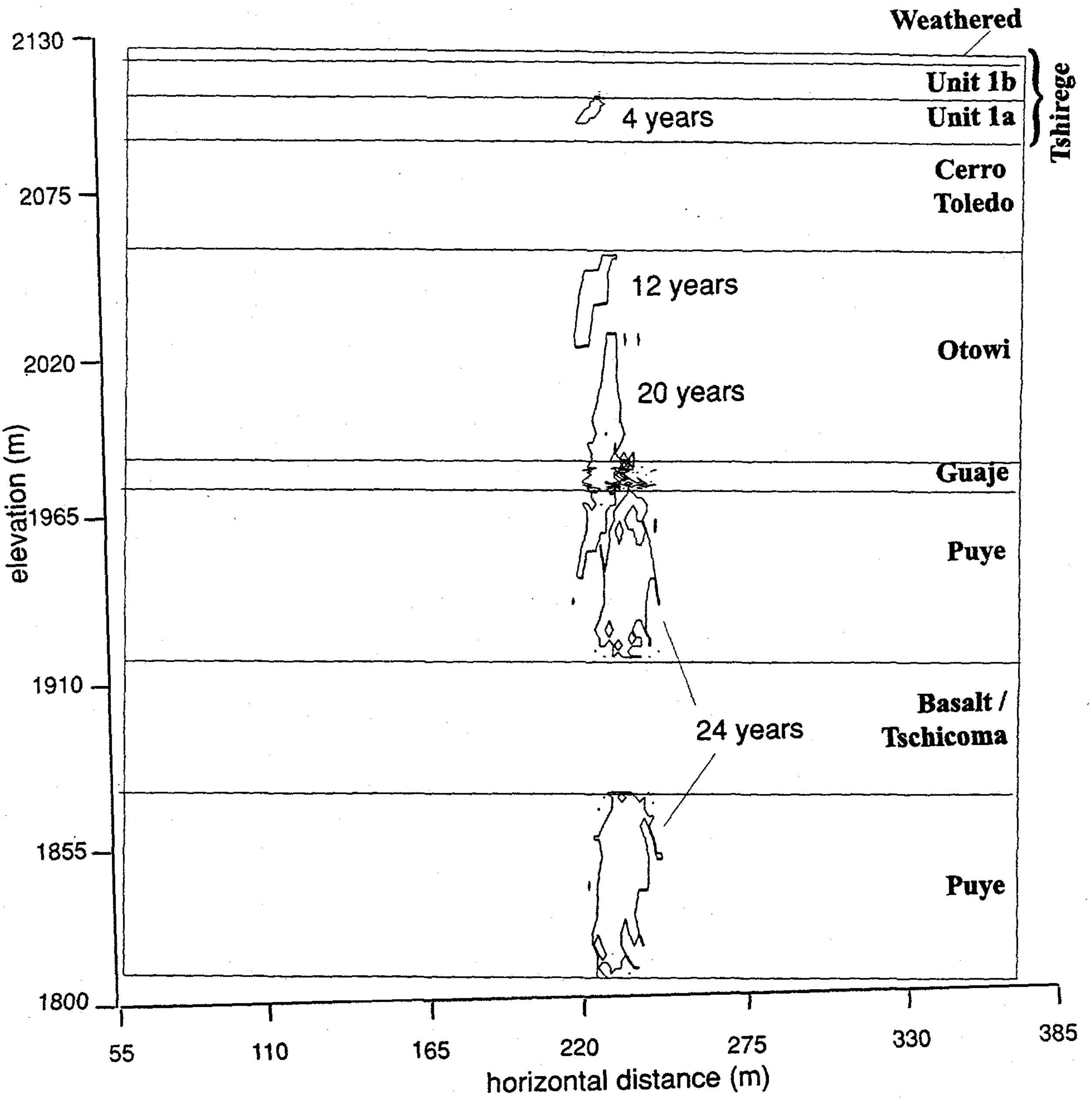

Figure 5.33 **Particle distributions for 1/2 x base case recharge simulation through First Refined Rectangular Grid.**

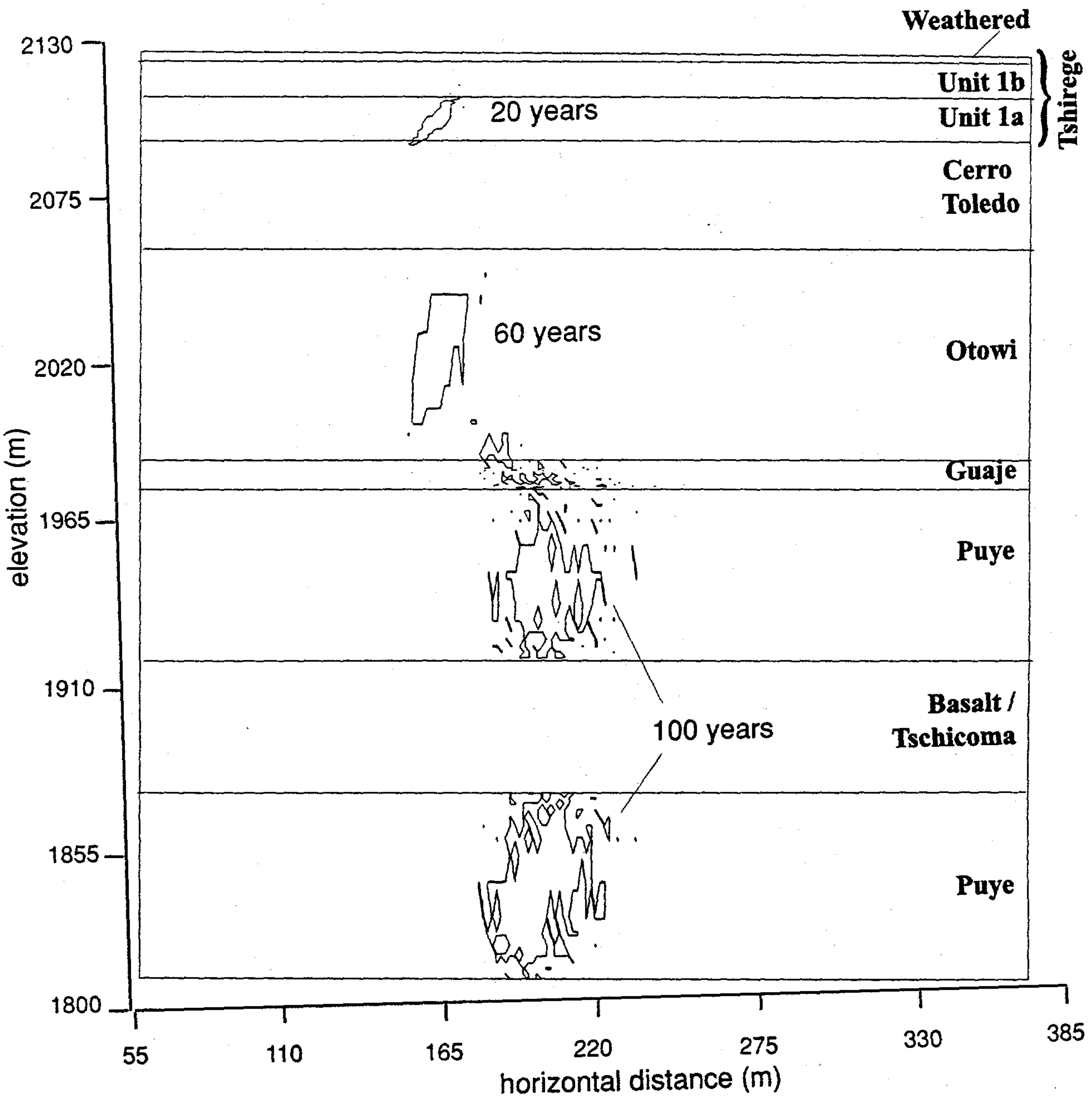

Figure 5.34 Particle distributions for 1/10 x base case recharge simulation through First Refined Rectangular Grid.

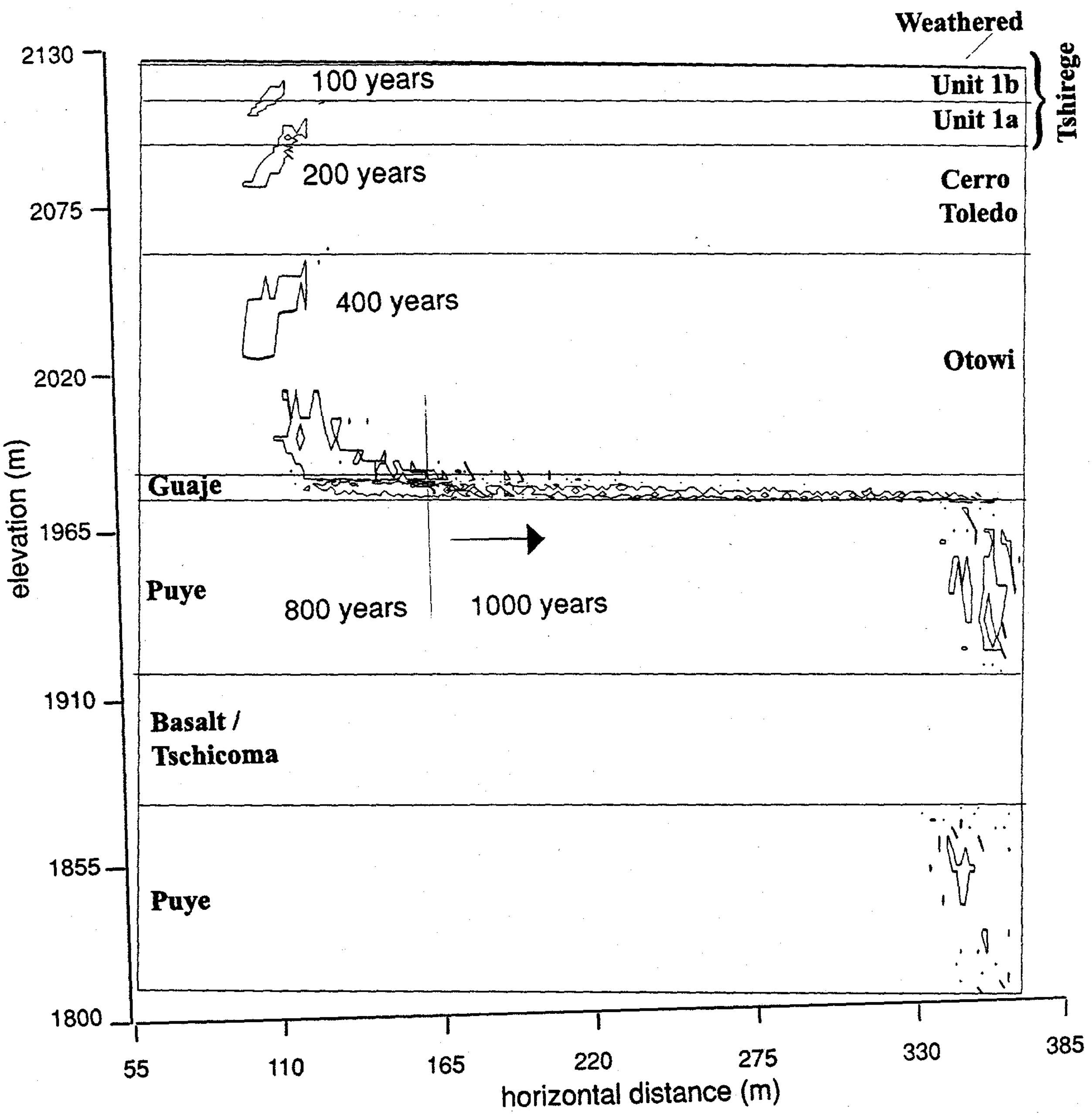

Figure 5.35 Particle distributions for 1/100 x base case recharge simulation through First Refined Rectangular Grid.

monitoring or perhaps remediation activities. Without a good understanding of the potential for horizontal transport of waters and contaminants during these activities, improper decisions on detection, locations, and effectiveness are possible.

5.7.2. Variations in Recharge Magnitude with Respect to Horizontal Position, Simulations 10 and 11

Previous cases assumed that distribution of recharge from the alluvial groundwater system into the tuff was uniform along the upper boundary of the model. It is not known how this recharge is actually distributed. Results that follow show how the system reacts with two possible extreme cases. The first is a linear decrease in recharge eastward (downstream) along the upper boundary. The second is a linear increase in recharge eastward along the upper boundary. Recharge totals equaled 1/2 times the base case, ranging between zero and base case for both functions. This range hopefully captured recharge fluxes that may be present, or might be expected further down canyon or away from the canyon axis. The linear recharge functions are indicated as increasing and decreasing with respect to position in Figure 5.24.

Simulations were performed in the same manner as in the First Refined Tilted Rectangular Grid simulation with the exception of changes to the distribution of recharge used at the upper boundary nodes.

Flow results were not plotted as depth profiles due to the large horizontal variation in results because of the recharge distribution.

Using these flow solutions particle tracking simulations were performed by distributing 1000 particles evenly across all upper boundary nodes. Results from the these simulations are plotted as snapshots of particles in Figures 5.36 and 5.37 moving through the system at specified times for the increasing and decreasing recharge scenarios, respectively. These plots illustrate solute movement over a range of recharge and indicate variations in transport times over that range. Although contours of particles are shown near the sides (within 50 m), they should be excluded from any analysis as they are affected by the side boundary conditions. This plot can also be used to compare all recharge scenarios, within this range, with a single figure. The plots differ from similar plots of constant recharge because the concentration of solute particles along the top is less (1000 particles at a single upper boundary node verses over the entire upper boundary). If recharge were to decrease with distance from its main source, the Radioactive Waste Liquid Treatment Facility, one might expect the distribution of particles traveling from the surface at various times, similar to that of Figure 5.36. If recharge were to increase with respect to the thickness of the perched alluvial groundwater system, one might expect the distribution of particles traveling from the surface at various times, similar to that of Figure 5.37. As in the constant recharge plots, particles are not seen in the volcanics because the fluid volume containing the particles is small due to the low saturation and porosity in the fractures and matrix. It is not possible to distinguish what degree horizontal flow has affected the solution. The figures do show

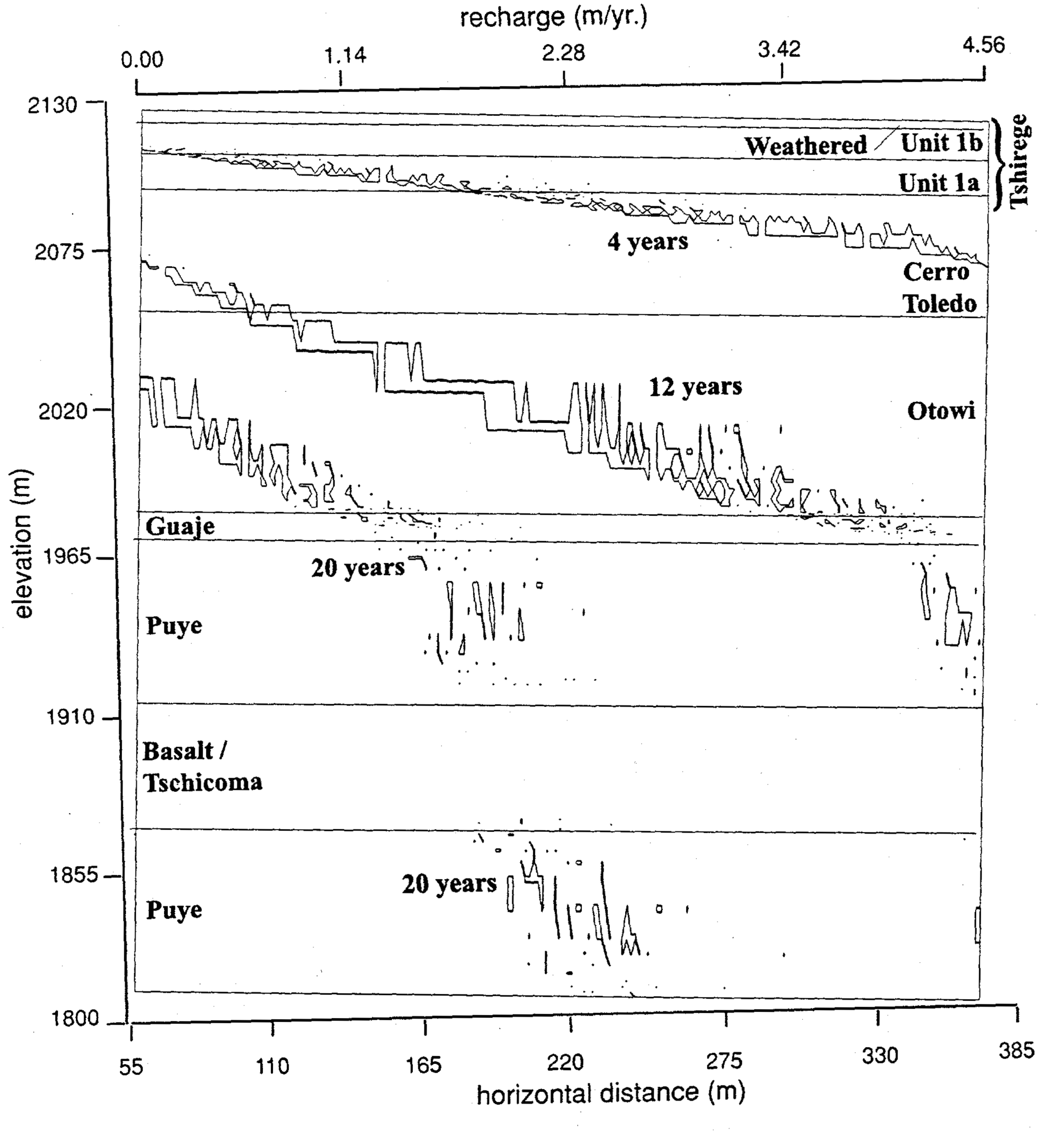

Figure 5.36 **Particle distributions for 1/2 x base case recharge simulation increased from 0 to 1 times base case across the upper boundary through First Refined Rectangular Grid.**

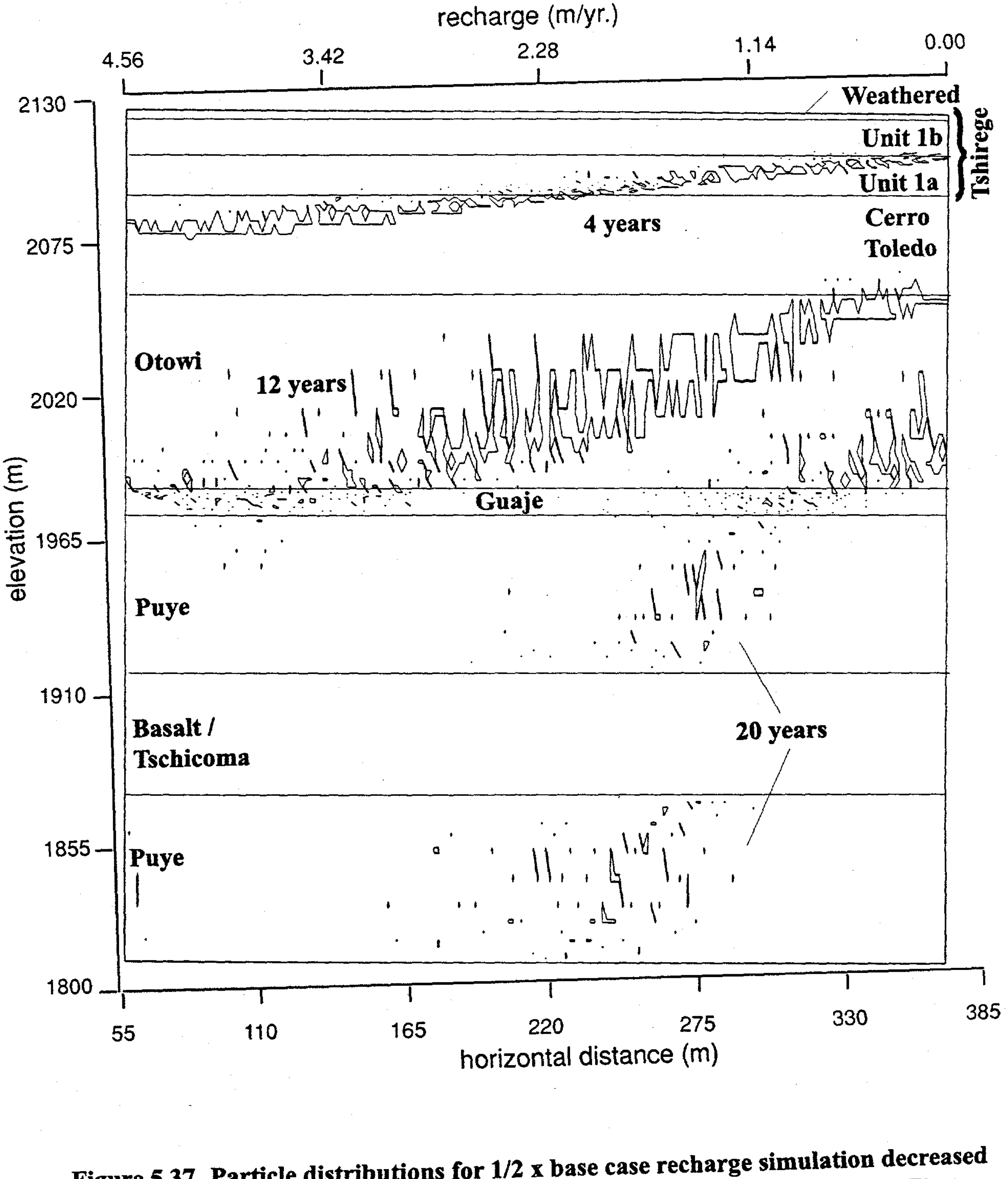

Figure 5.37 Particle distributions for 1/2 x base case recharge simulation decreased from 0 to 1 times base case across the upper boundary through First Refined Rectangular Grid.

greater spreading (vertically) and rate of particle movement in the lower units (Puye, Basalt/Tschicoma, and Guaje) than in the upper units (Otowi, Cerro Toledo, and Tshirege). This is attributed to the difference in vertical average linear velocities between the upper and lower units.

5.8. MORTANDAD CANYON GRID NUMBER 5, SIMULATION 12

The impact of grid spacing and recharge variation have been explored in the forgoing simplified simulations. The next simulation used an unstructured grid to utilize the best quality of finite elements (the ability to match stratigraphy) accommodating all lithologic boundaries within the longitudinal section in Figure 3.6. The purpose is to simulate the entire unsaturated zone beneath Upper Mortandad Canyon, whereas other simulations depicted a typical stratigraphic profile from that section and tilted it to represent dipping stratigraphy. The horizontal extent of the domain in this simulation is over six times that in the previous simulations. The vertical resolution seen in previous grids was decreased to accommodate the larger model area while keeping the number of nodes to a workable quantity. Therefore, in this one respect results may not be as accurate as those derived from the First Refined Tilted Grid simulation, number 3. However, this simulation does accomplish much meeting the objective above while producing results close to those in simulation 3.

Using the GEOMESH grid generator an unstructured, triangular, finite element grid was created with properties listed after grid number 5, in Table 5.1. The grid shown in Figure 5.38 encompassed the entire longitudinal section of Figure 3.6, and captured all stratigraphic interfaces at nodes. Vertical spacing of nodes was produced manually and used as input for the grid generator. Those spacing varied for each material and within some materials to best reflect vertical changes in results seen in the previous simulations. The grid generator determined variable horizontal spacing of nodes depending on vertical spacing by creating triangular elements with angles less than 90° ideal for code calculations.

The flow simulation was performed in the same manner as the previous simulations, with the exception of the recharge at the upper boundary. Because the area associated with each upper boundary node varied, this area was factored into new recharge values to distribute boundary flux evenly.

Pressure and saturation solutions over the entire domain are illustrated in Figures 5.39A-C and 5.40A-C. No vertical exaggeration is used, and the grid of the longitudinal section in Figure 3.6 was broken into three parts to show better detail of the values throughout the domain. For those reading thesis copies in black and white, a color version for these figures may be found on the web at this internet address: **http://drambuie.lanl.gov/~esh18/dander.html** Results in each plot depict system behavior very similar to and values close to the profiles First Refined Grid simulation in Figures 5.13 and 5.14. Irregularities in these colored plots and differences from previous profile plots are discussed below.

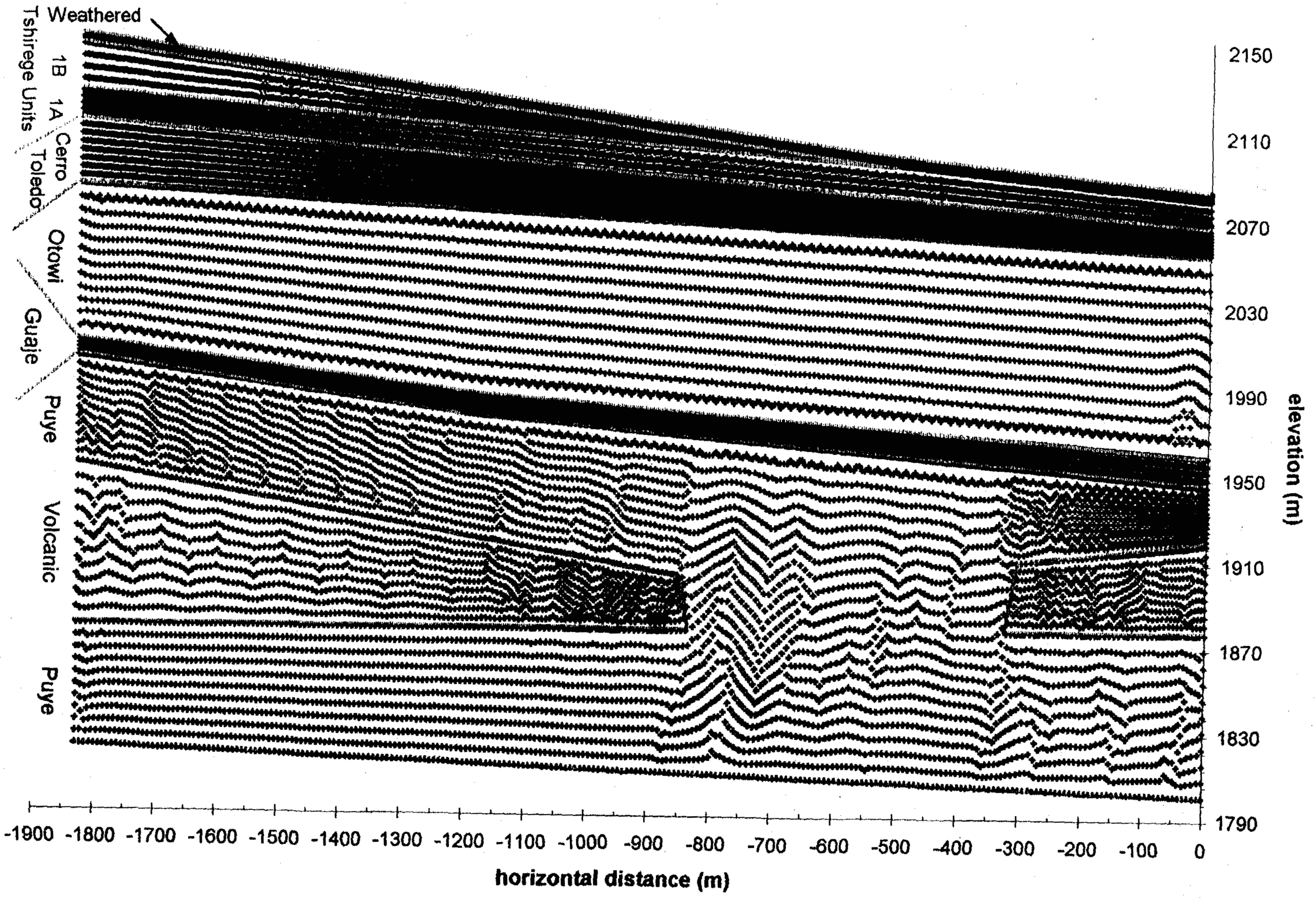

Figure 5.38 Mortandad Canyon Grid.

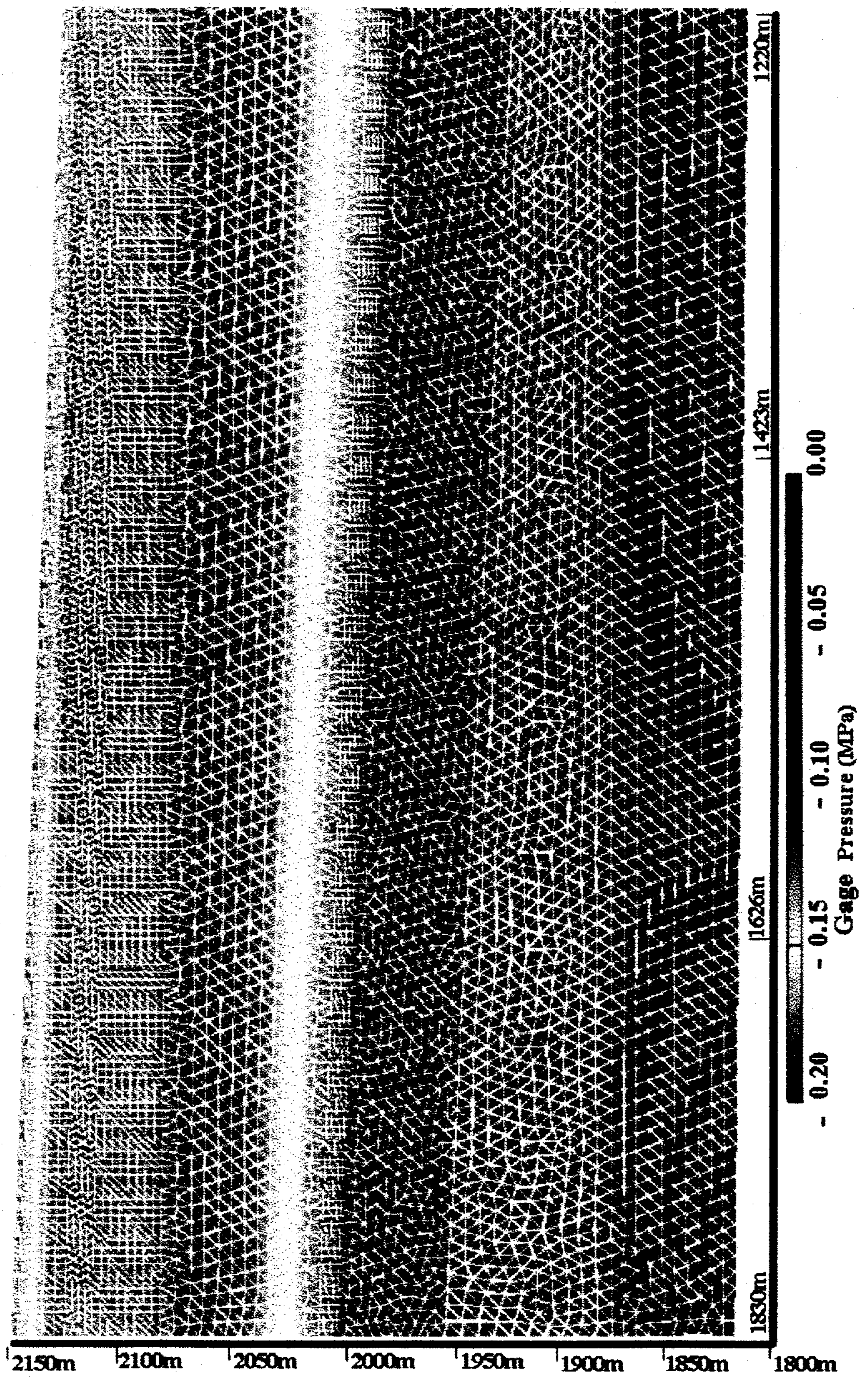

Figure 5.39A Pressure solution to the Mortandad Canyon Cross Section Grid. Pressure units are in MPa.

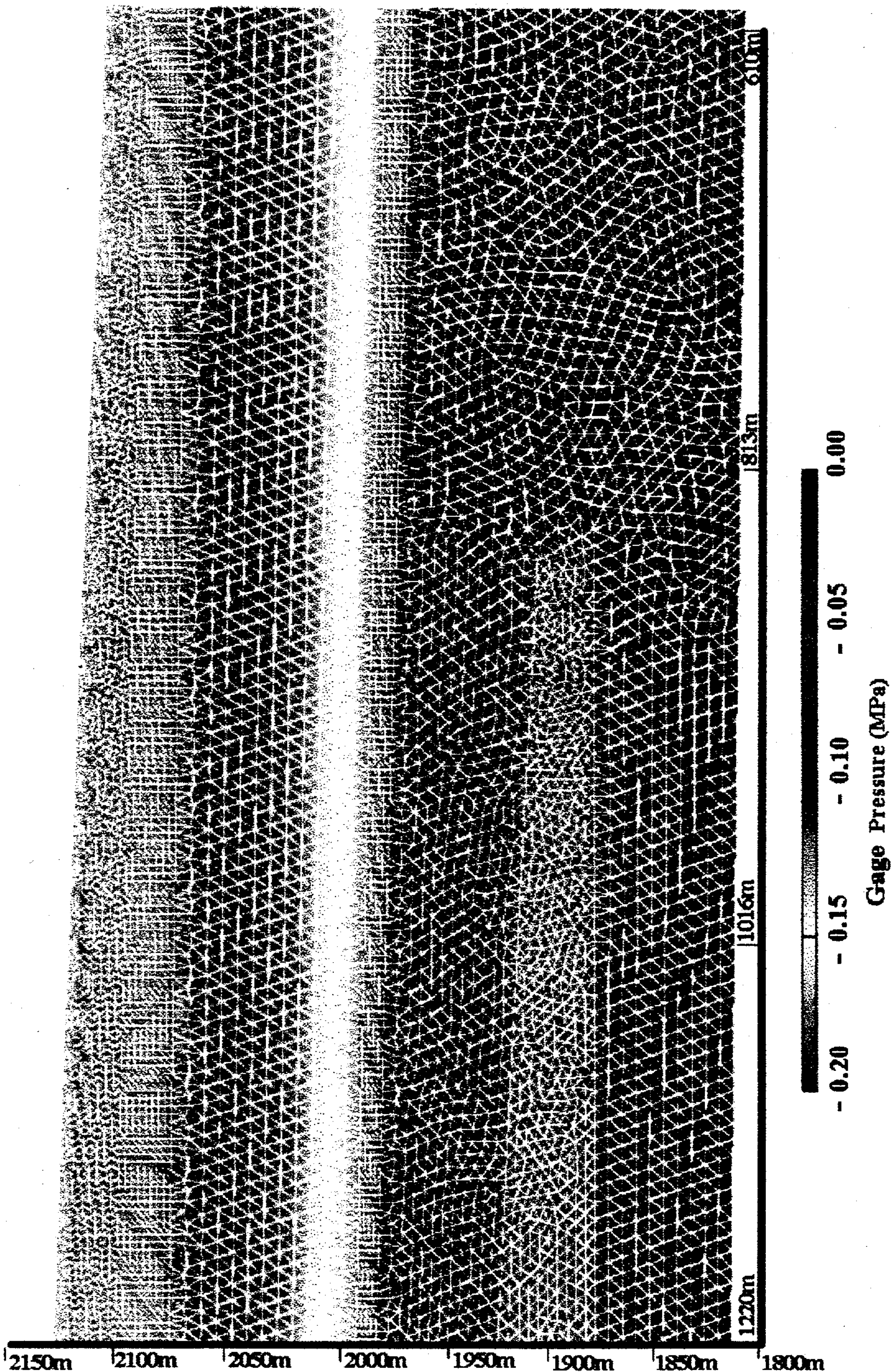

Figure 5.39B Pressure solution to the Mortandad Canyon Cross Section Grid. Pressure units are in MPa.

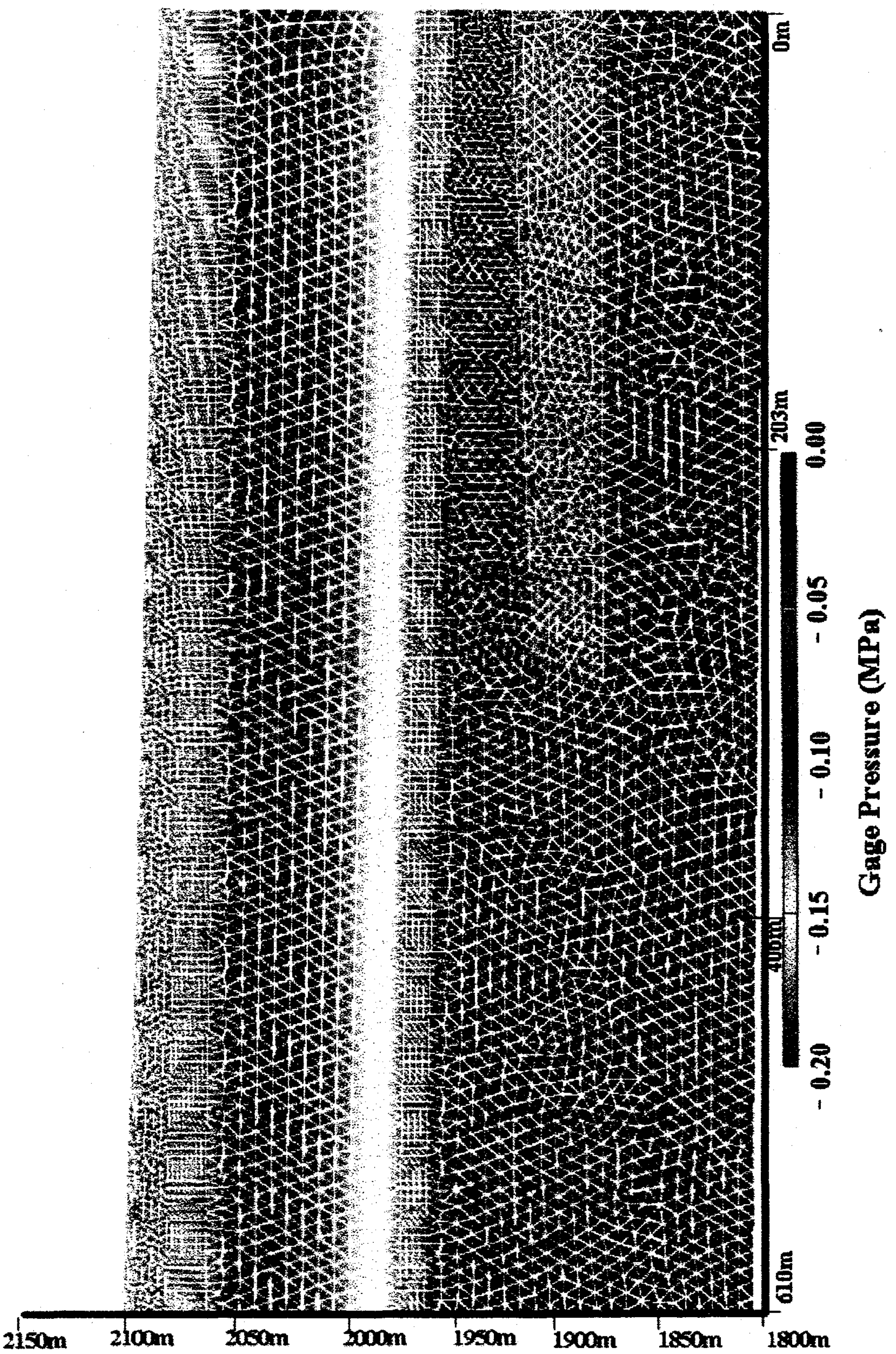

Figure 5.39C Pressure solution to the Mortandad Canyon Cross Section Grid. Pressure units are in MPa.

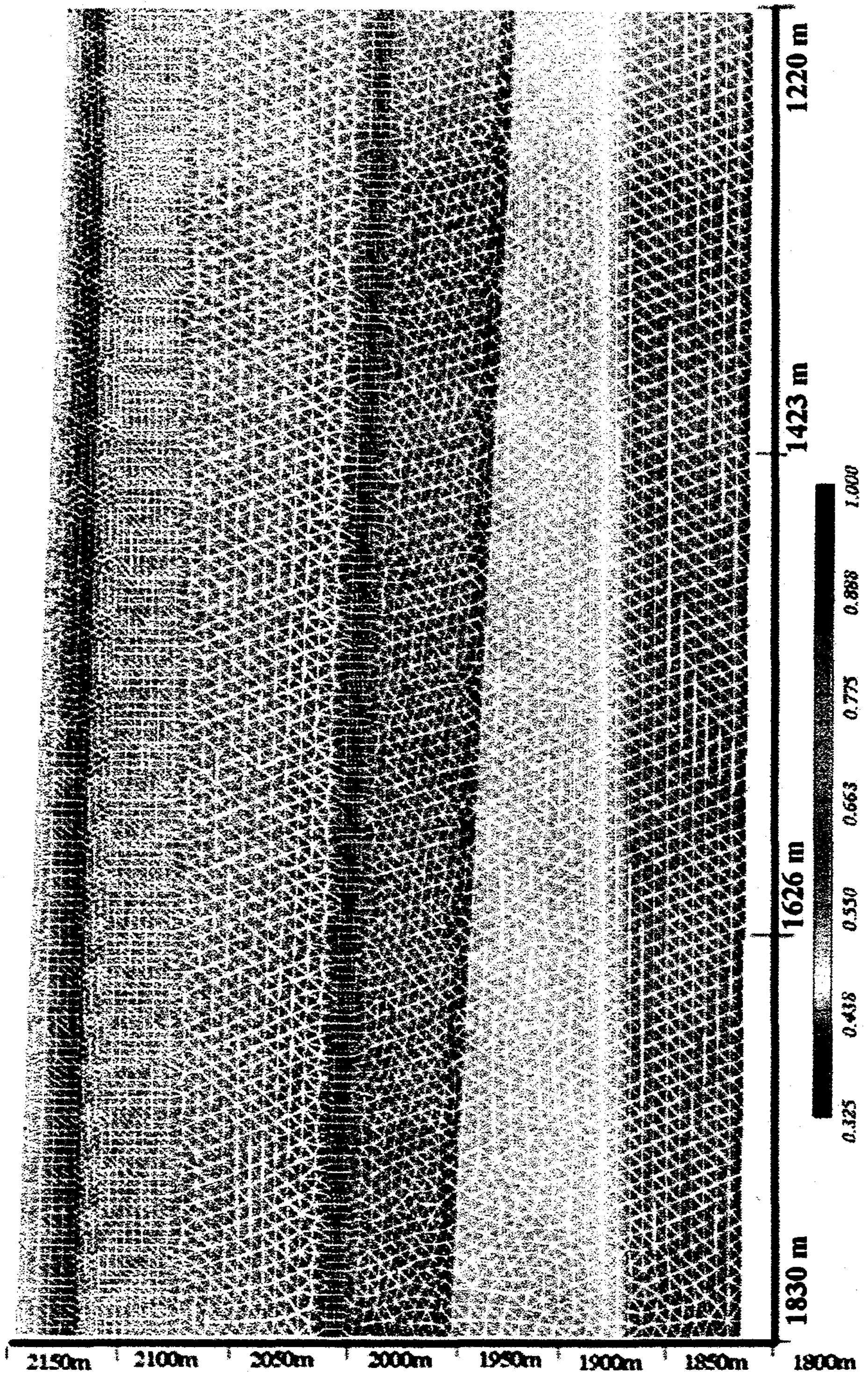

Figure 5.40A Saturation solution to the Mortandad Canyon Grid simulation.

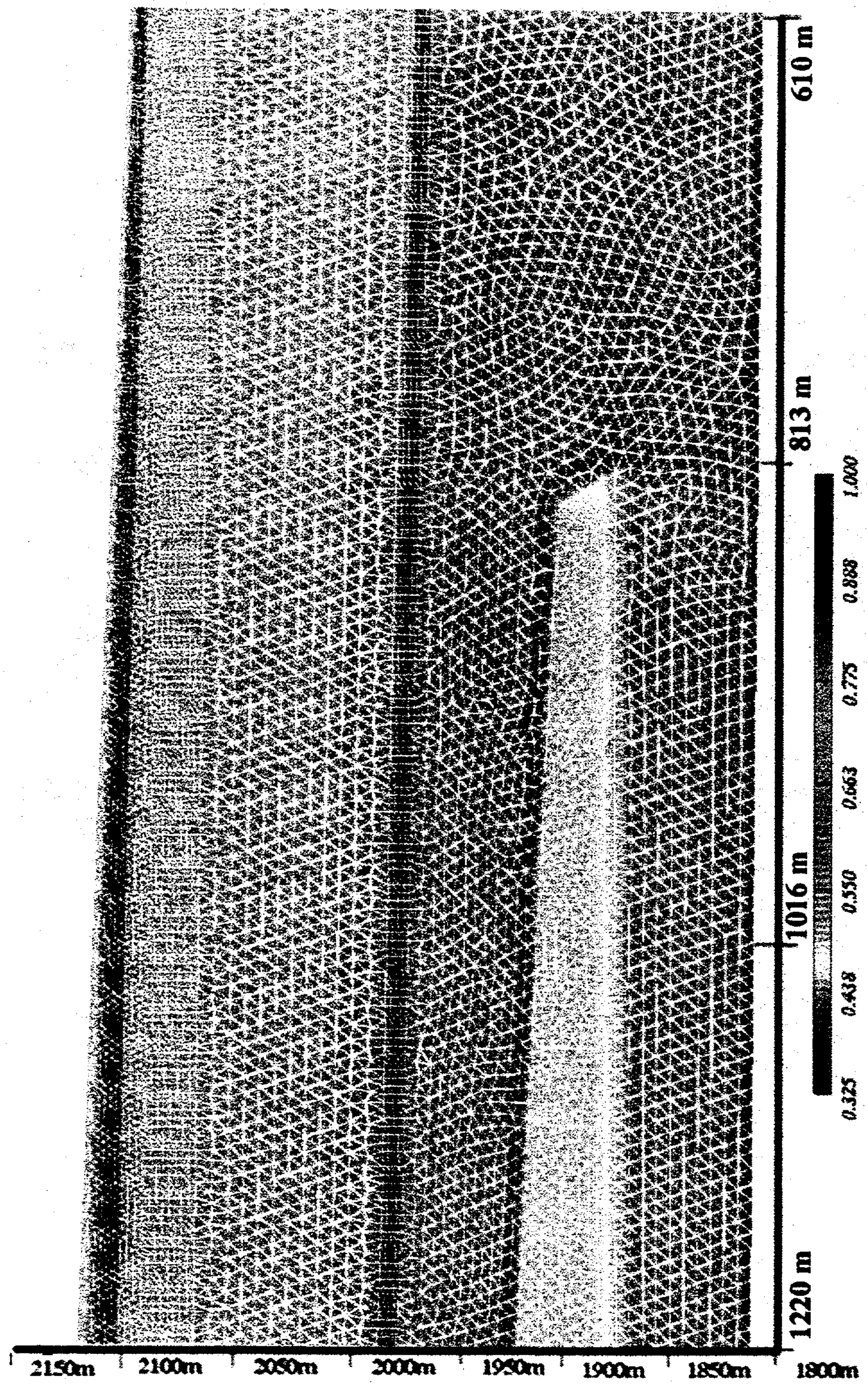

Figure 5.40B Saturation solution to the Mortandad Canyon Grid simulation.

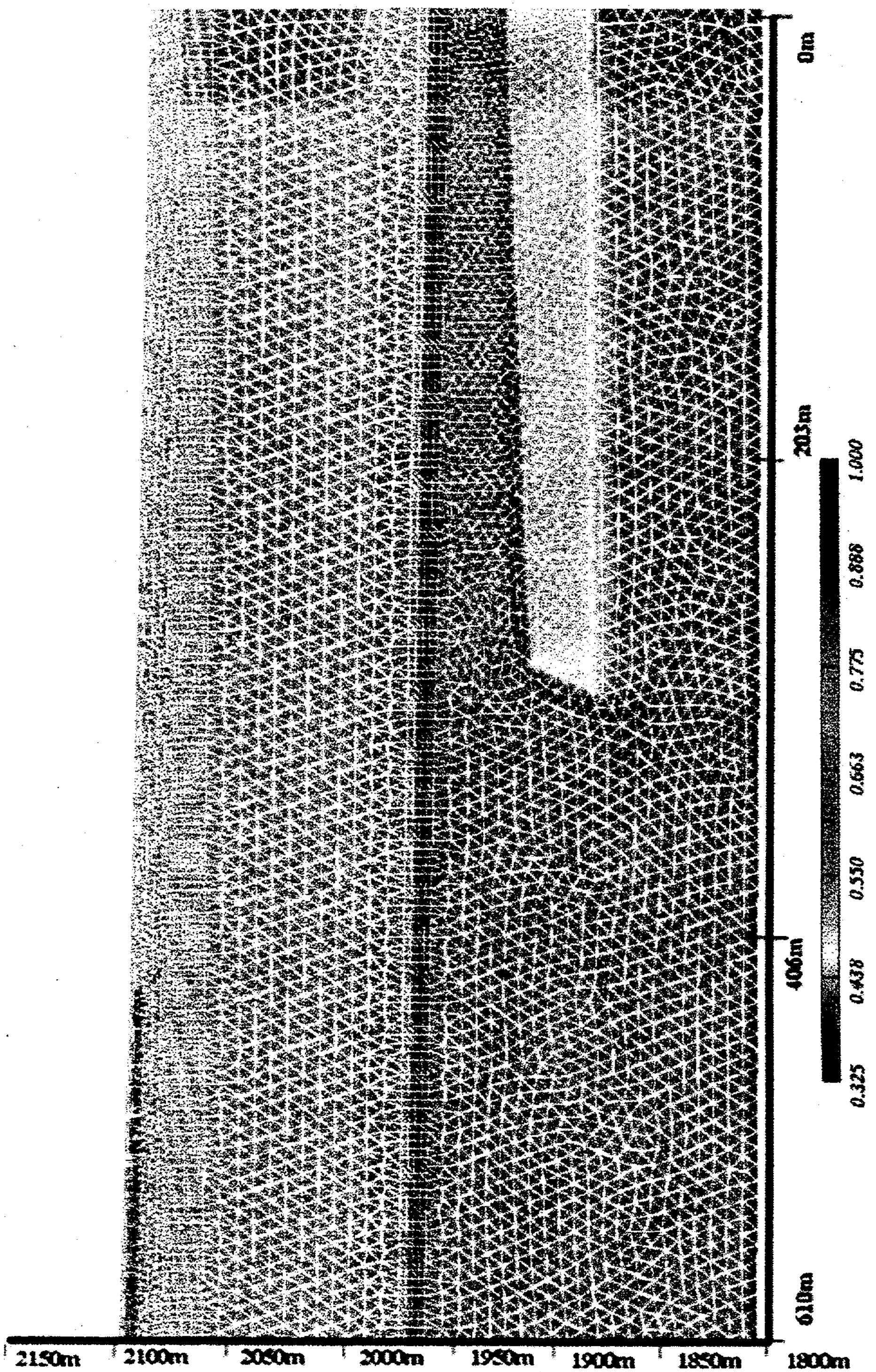

Figure 5.40C Saturation solution to the Mortandad Canyon Grid simulation.

Vertical changes in pressure and saturation are better observed in depth profiles presented later. Figures 5.39-5.40 best show horizontal variations in pressure and saturation when the stratigraphy varies as well. Careful inspection shows slight horizontal variations in results close to the left side boundary in Figures 5.39A and 5.40A and the right side boundary in Figures 5.39C and 5.40C. These horizontal variations are from the side boundary conditions and do not affect the solution away from the sides, approximately 50 m. A slight streaking zone of low saturation is noticeable below the lower right and lower left corners of the pinched-out Unit 2 Basalt and Tschicoma Formation in Figures 5.39B and 5.40C, respectively. These streaking zones are caused by the lack of recharge from the less saturated near vertical interfaces between the Puye and volcanics above.

Pressure and saturation depth profiles were observed at five transects across the grid. The five transects, lying at 300 m intervals indicated in Figure 3.6, were chosen at important stratigraphy changes. Those locations captured lithologic thickness variations; intervals with and without volcanics; the edge and middle of the volcanics; and the intervals with and without the Tshirege 1B. Results for the five transects are shown in depth profiles in Figures 5.41 and 5.42. Those results came from the same data used to plot the colored pressure and saturation plots in Figures 5.39 and 5.40. They exhibit behavior similar to and values close to the First Refined Grid

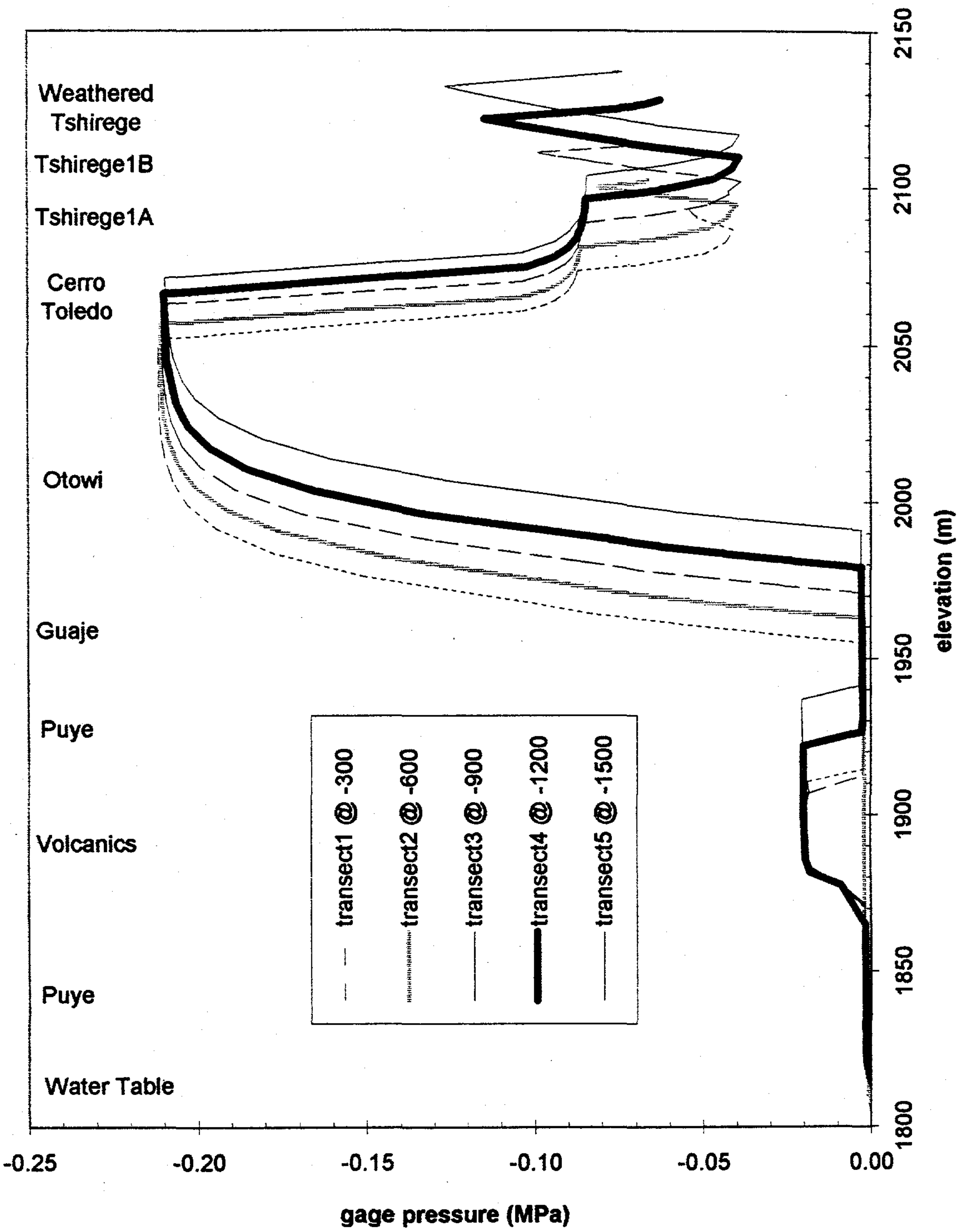

Figure 5.41 Pressure depth profiles for Mortandad Canyon Grid.

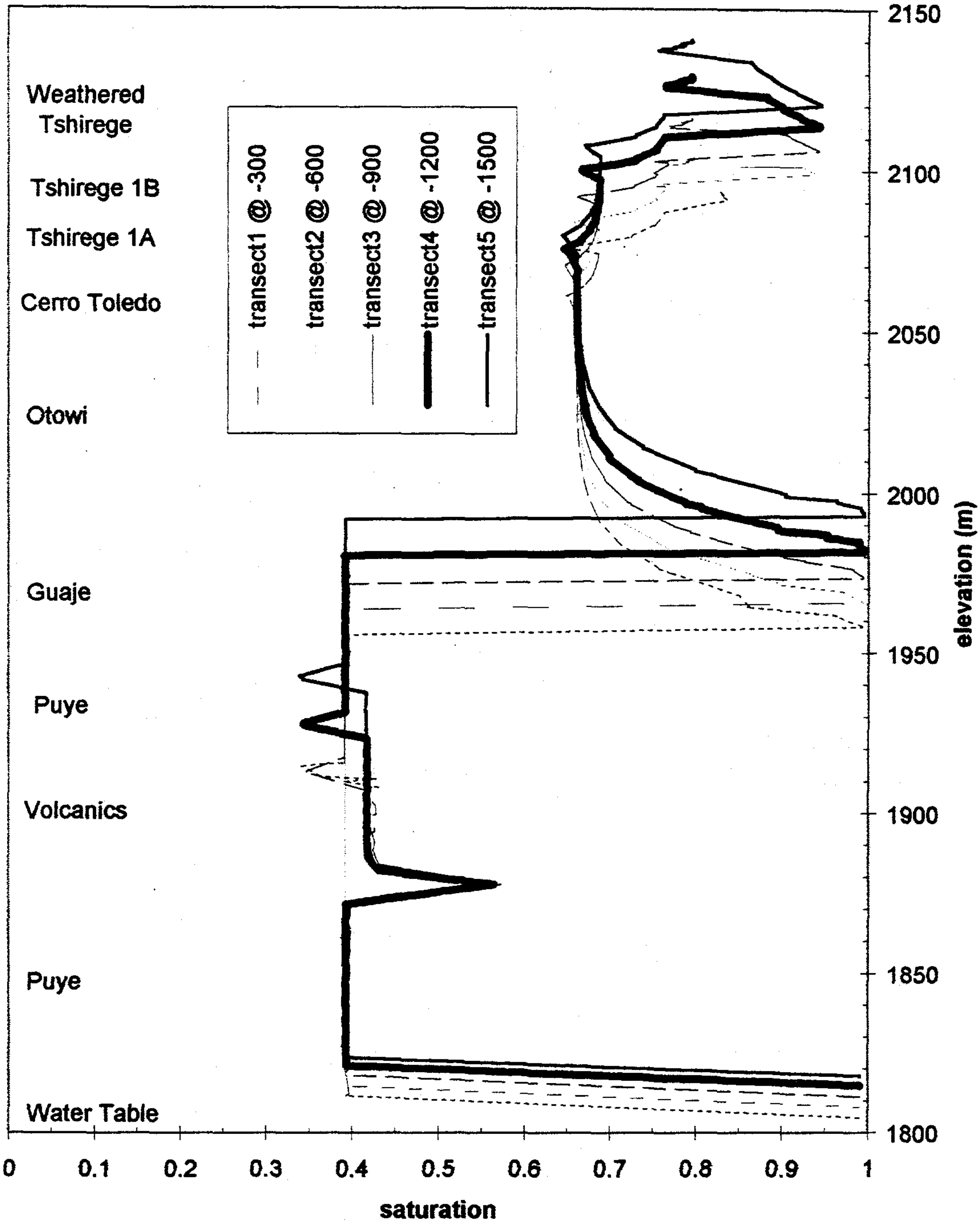

Figure 5.42 Saturation depth profiles for Mortandad Canyon Grid.

simulation in Figures 5.13 and 5.14 with the exception of the lithologic contact elevations. Those contacts are not shown because their elevations vary for each transect. However, the units are labeled and approximation of contact elevations for each transect can be seen from the plotted results. Peaks and dips in pressures and saturations at lithologic interfaces are less than those in the First Refined Grid simulations. This is because vertical spacing of nodes at those interfaces were larger then those in the refined grids.

Velocity depth profiles are not presented for the following reason:

> "FEHM solves for the flux between nodes rather than velocity. One can approximate the velocity field based upon the flux; however, the velocity is not the fundamental quantity that is solved for, so any representation of a velocity field is only an approximation. While the approximation works well with structured grids, the approximations made are less valid for highly unstructured grids."(Gable, 1998)

Because particle tracking is done on a cell-by-cell basis using mass fluxes to adjacent cells, the lack of velocities did not affect the particle tracking solution. Using the flow solution from this simulation, a particle tracking simulation was performed. Particles were introduced along the upper boundary at five node locations above the five transects described above.

Results from the particle tracking simulation are plotted as breakthrough curves at the lower boundary (Figure 5.43). The curves for this simulation show the mean of the particles reaching the regional aquifer between 13-14 years. The mean breakthroughs of the

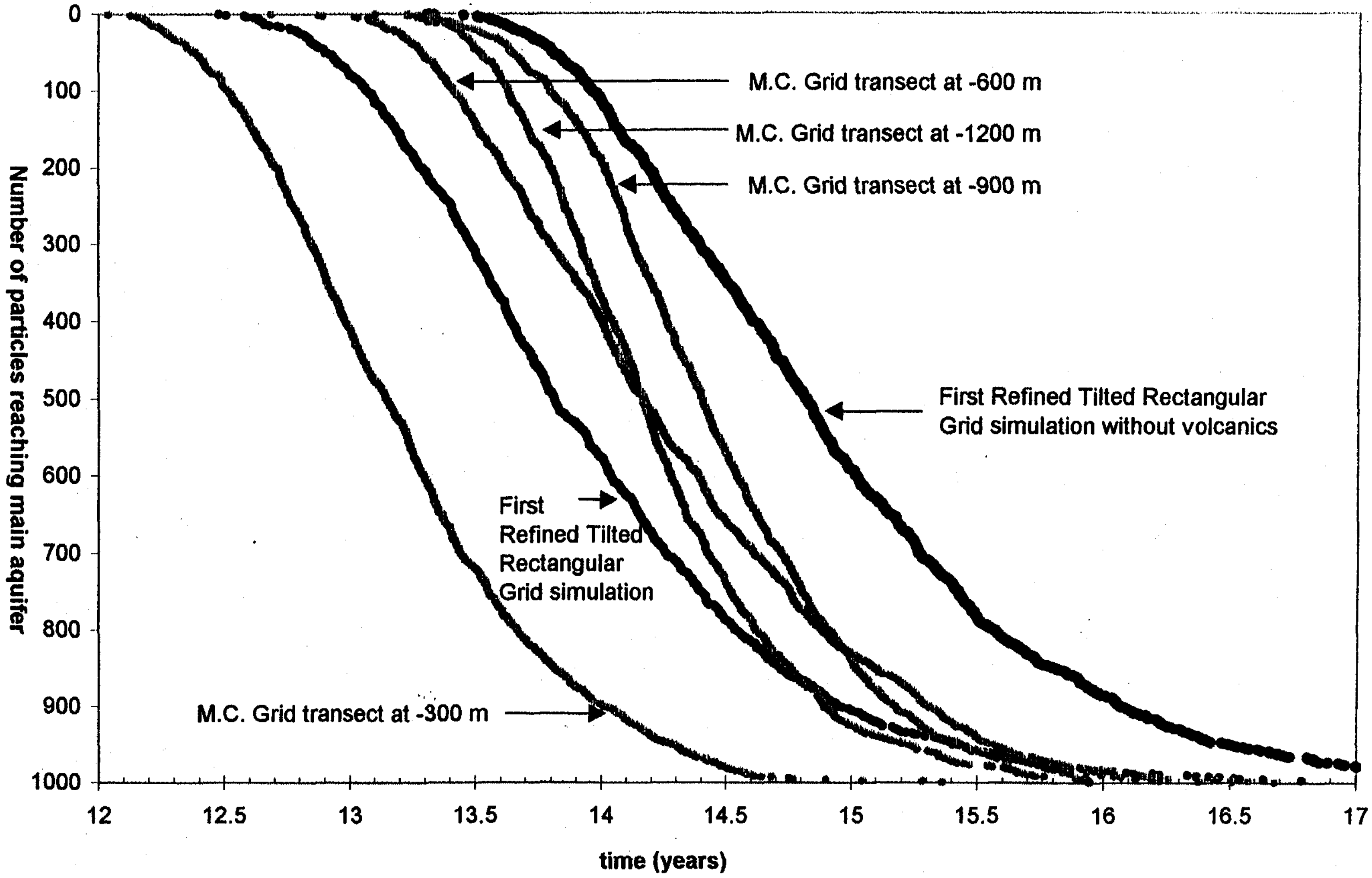

Figure 5.43 Breakthrough curves for Mortandad Canyon Grid and First Refined Rectangular Grid simulations at base case recharge.

particles introduced at -300 m and -900 m on the longitudinal section were about 13.2 and 14.2 years, respectively. The difference in breakthrough times is probably a result of the increased distance traveled and variation of lithology encountered. The variation in arrival times caused by the variation in flow paths is similar to those in the First Refined Tilted Rectangular Grid simulation, number 3. The mean breakthrough of the particles introduced at -600 m on the longitudinal section was about 14.4 years. The spread in arrival times for these particles is slightly less than in the previous two curves. This possibly indicates that the volcanics and two additional lithologic contacts cause greater spread. The longer travel time and reduction of spreading in arrival times is probably due to the fact that only Puye was encountered at the lower elevations in the simulation. The mean breakthrough of the particles introduced at -1200 m on the longitudinal section was about 14.2 years. This transect was at the same location that the stratigraphic profile used in all other simulations was taken from. The mean breakthrough of the particles was about the same for both the -900 m curve and the curve for simulation number 3. Results for particles introduced at -1500 m on the longitudinal section were lost, but suspected to be similar to results from the simulation with particles introduced at -1200 m on the longitudinal section with similar stratigraphy.

Grid spacings for this simulation were fairly large. The First Refined Tilted Rectangular Grid (number 3) is considered the best representation of flow beneath the canyon. This simulation was helpful for comparisons and necessary to represent stratigraphy throughout the entire longitudinal section below Upper Mortandad Canyon.

Snapshots of the five plumes show concentrations of particles moving through system at specified times in Figure 5.44. At certain times particles at different locations may be found in different lithologic units because of the variable lithology below each of the five injection points. Some of the particles at the –300 and –600 transects, migrate around or into the pinched-out volcanics.

5.9 COMPARISON OF MODELED AND FIELD DATA

Depth profiles of saturation of core samples from Rogers and Gallaher (1995) are available for wells MCM-5.1 and MCM-5.9A, further down canyon from this study area (Figure 3.1). Those profiles are presented in Figure 5.45 with the results from the First Refined Tilted Grid simulation, number 3. The field data were not used for calibration because of their location further downstream in the canyon, where recharge may be lower. The different locations also caused the lithologic contacts and thickness to differ. Furthermore, the field data only covers part of the modeled profile.

There is little data in the Tshirege units to compare with modeled results, however, the available data in that unit does suggest lower saturations similar to the 1/10 and 1/100 times base case recharge simulations. Effects on the model solution caused by changes in recharge were examined in section 5.7.

The field data show high variability with peaks and dips of saturation within the Cerro Toledo Interval, averaging about 50% saturation. Saturations in the modeled Cerro

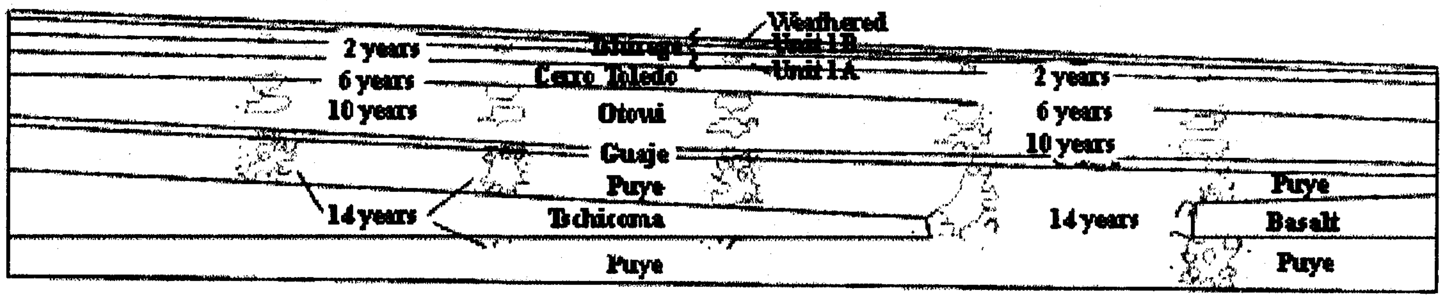

Figure 5.44 Particle tracking concentrations for Mortandad Canyon Longitudinal-Section Grid.

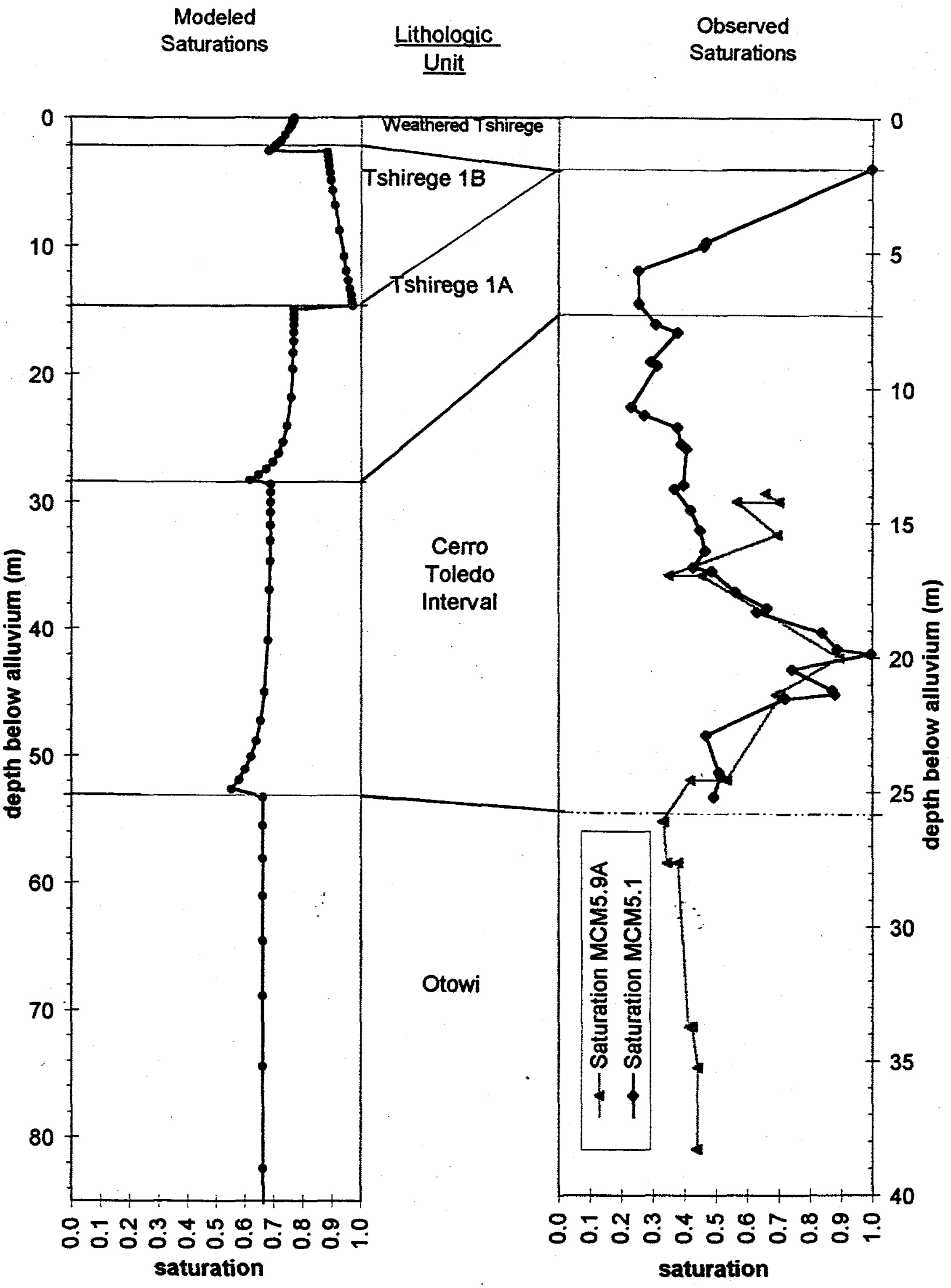

Figure 5.45 Modeled and observed saturation data.

Toledo Interval average about 65%, and values decrease from 72% to 55% with depth. This may be caused by the heterogeneous nature of the rocks compared to the assumed homogeneous model lithology. That is, there are likely lithologic contacts on scales smaller than modeled during this study that show significant effects on the system behavior. Capillary barriers to vertical flow within the materials may be common, therefore more horizontal flow could occur than simulations show reducing vertical flow and increasing the travel times to the regional aquifer.

A relatively constant saturation averaging 40% in the Otowi Unit field data suggest it is a homogeneous material. This saturation is a bit less than the modeled results, averaging 65%, but again similar to the 1/10 and 1/100 times base case recharge senerio. Saturation in the core data could be lower than the base case modeled results due to lower recharge at the well locations.

A recharge study by Abrahams et al. (1961) of a mesa top environment concluded that the downward movement of water is impeded or stopped by the dense transition zone between the soil and Bandelier Tuff. Prior to releasing effluents into Upper Mortandad Canyon Baltz et al. (1963) concluded that the amount of liquid moving from the alluvium to the underlying Bandelier Tuff will be relatively small and is unlikely to make it to the regional aquifer. In this study, interconnected flow between the saturated alluvial system and the regional aquifer is shown to occur. Travel times over this distance thought to be lengthy are not, in fact, they are quite rapid.

Recharge and location for each study mentioned above is different. Hence, results were expected to differ also, but, comparisons are needed to help draw conclusions about this study.

6. CONCLUSIONS

6.1 CONCLUSIONS

The study of the unsaturated system beneath Upper Mortandad Canyon showed that: Unsaturated groundwater flow is predominately downward. Horizontal components of flow occur near the lithologic contacts and are most prevalent at the base of the Tshirege 1B, Guaje Pumice Bed, and volcanics. Flow results, particle paths and particle travel times are highly dependent of recharge applied to the system. Interconnected flow between the saturated alluvial system and the regional aquifer is shown to occur. Travel times over this distance are quite rapid on the order of tens of years. The proportion of lateral flow to vertical flow increases when recharge decreases, and lateral flow can even surpass the vertical flow at very low recharge.

Knowledge of the degree of horizontal flow present in the system could be important to contaminant pathways. This importance lies in situations such as attempting to find contamination during monitoring or perhaps remediation activities. Without a good understanding of the potential for horizontal transport of water and contaminants during these activities, improper decisions on detection, locations, and effectiveness are possible. Additionally, heterogeneity within materials may be common and could cause even more horizontal flow to occur than represented here.

Saturation occurs within the lower portion of the Guaje Pumice Bed regardless of how much recharge was applied. The base of the Tshirege 1B unit almost reaches saturation with water budget estimated recharge and higher values, and changing recharge does change the saturation values. Variations in recharge (temporal and spatial) are expected in different parts of Mortandad Canyon, as well as other canyons and under the dry mesa tops. The variable recharge magnitudes and distributions simulated in this study illustrate system behavior in such situations. The water budget for the canyon indicates that seasonal and annual fluctuations are causing a transient pulse of recharge. Although steady-state conditions were examined, some conclusions drawn using various recharge scenarios may be applicable to these transient scenarios as well.

Downward average linear flow velocities were the greatest in the Puye and volcanics and were about three times those in the Bandelier Tuff. The Puye and volcanics also showed lower saturations than the Bandelier Tuff. Additional simulations using volcanics matrix properties only (no fracture properties) generated near-saturated conditions and flow velocities about half of those of effective continuum simulations, within the Basalt. The extent and degree of fracturing in the volcanics is not known, and simulations were based on an estimate of the values. Properties of volcanics could vary from no fractures to highly fractured, if present at all below Upper Mortandad Canyon.

Small vertical grid spacing, <0.1 m at lithologic interfaces where material properties contrast greatly, are necessary for an accurate solution. Horizontal grid spacing could vary without affecting the flow solution, as long as the element aspect ratio did not become too great, causing convergence problems. The horizontal domain width, on the other hand, needs to be large enough to isolate effects from the side boundary conditions from the results being analyzed.

6.2. RECOMMENDATIONS FOR FUTURE WORK

Based on the conclusion that the flow in the unsaturated zone beneath Upper Mortandad Canyon is highly sensitive to recharge, the accuracy of the water budget is of great importance. The water budget could be recalculated using current flow data, alluvial groundwater depths, and evapotranspiration estimates. This would require the installation of a gaging station near the lower end of the study area. Water level and evapotranspiration measurements from the site soon will be available.

The placement of a deep well in Upper Mortandad Canyon would be highly beneficial to further studies in several ways. Deep well data are needed to determine precise contact depths, rock properties, degree of fracturing, insitu pressures and saturations especially in the deeper units such as the Guaje Pumice Bed, Puye Formation, and volcanics.

The large differences in flow behavior found in simulations with different recharge suggest temporal variation may be important. Simulations that were performed were based on constant recharge over time. Seasonal variations of recharge should be considered during further modeling.

Further flow and transport modeling of this system could also include other code capabilities to improve model accuracy. These might include modeling vapor flow, non-isothermal conditions, matrix diffusion and dispersion, and double nodes at lithologic interfaces. Other useful variations that could improve this models accuracy include:

Modeling in the third-dimension and including the saturated alluvium as an upper boundary and letting it drain to recharge the lower unsaturated units.

Another FEHM code option called dual porosity/dual permeability is superior to the effective continuum approach used in this study and could be used for further modeling. The effective continuum approach uses a weighted average between flow properties of the fractures and matrix. These properties may never exist in the system and only approximate the solution between the two possible extremes. If more can be learned about the rocks the dual porosity/dual permeability approach would allow fracture and matrix flow to occur concurrently, leading to a more realistic solution.

Accurate representation of lateral diversion of flow at capillary barriers are important to larger scale flow and contaminant migration conclusions for this system. Two references suggested for review prior to further or related studies on this subject are by Ross (1990 and 1991). They examine more closely the flow behavior and diversion capacity at capillary barriers. Two other reference worthy of review are by Warrick et al. (1996) and Selker (1997). These papers examine effects of variations in slope, recharge, and lithology on flow behavior and diversion capacity at capillary barriers.

APPENDIX A: INPUT FILES

```
title: 2d - Mortandad Canyon required data for flow simulation
#***************************75
pres
-1 0 0  0.974890977E-01   0.288141634E+00 2
-2 0 0  0.983598070E-01   0.290793914E+00 2
-3 0 0  0.796964858E-01   0.415766895E+00 2
-4 0 0 -0.287806941E-01   0.790719014E+00 2
-5 0 0 -0.114939565E+00   0.650872839E+00 2
-6 0 0  0.769448671E-02   0.677805465E+00 2
-7 0 0 -0.383920195E-01   0.858228610E+00 2
-8 0 0  0.200809939E-01   0.748442659E+00 2
-9 0 0  0.290226886E-01   0.773320457E+00 2

#***************************75
perm
-9    0 0 2.645e-13 2.645e-13  2.645e-13
-8    0 0 1.955e-13 1.955e-13    1.955e-13
-7    0 0 3.680e-13 3.680e-13    3.680e-13
-6    0 0 1.495e-12 1.495e-12    1.495e-12
-5    0 0 7.245e-13 7.245e-13    7.245e-13
-4    0 0 1.725e-13 1.725e-13    1.725e-13
-3    0 0 5.324e-12 5.324e-12    5.324e-12
-2    0 0 1.000e-13 1.000e-13    1.000e-13
-1    0 0 5.324e-12 5.324e-12    5.324e-12

#***************************75
rlp
3    .111   1.0    .138    1.583   2.    .061
3    .017   1.0    .044    1.660   2.    .019
3    .035   1.0    .222    1.592   2.    .028
3    .035   1.0    .187    1.481   2.    .027
3    .055   1.0    .066    1.711   2.    .036
3    .000   1.0    .081    4.026   2.    .010
3    .180   1.0    14.5    2.680   2.    .055
4    .066   1.0    3.84    1.474   2.    .076
    .03    1.0    3.84    1.474   2.    .020    1e-
06  1.e-13  1.e-4
3    .180   1.0    14.5    2.680   2.    .055

-9   0   0   1
-8   0   0   2
-7   0   0   3
-6   0   0   4
-5   0   0   5
-4   0   0   6
-3   0   0   7
-2   0   0   8
-1   0   0   9

#***************************75
rock
-9   0   0   1260   1000   0.460
-8   0   0   1180   1000   0.528
-7   0   0   1160   1000   0.509
-6   0   0   1250   1000   0.490
-5   0   0   1180   1000   0.469
-4   0   0   810    1000   0.667
-3   0   0   1200   1000   0.250
-2   0   0   1200   1000   1.e-4
-1   0   0   1200   1000   0.250

#***************************75
flow
 1   61   1   .1                .99    1e-2
 3784  3842 1  -1.157D-03   0.99000000000  0.
 3783  3783 1  -5.786D-04   0.99000000000  0.
 3843  3843 1  -5.786D-04   0.99000000000  0.

#***************************75
time
1e-2  1e9  50000   1  1997  1  0.0
0. 0.
#***************************75
ctrl
  15   1.e-3   8
  1    0 0 2
  0
  1.0  2   1.0
  10   1.2  1.e-10 1.825e12
  1  -1
#***************************75
iter
1.e-5 1.e-5 1.e-5 1.e-5 1.1
0 0 0 5  1200.
#***************************75
```

```
sol
1   -1
#***************************75
air
1
20.0 0.1
#***************************75
text
Output Controls

#***************************75
cont
avs  500000000  3.0e15
liquid
vel
pres
sat
mat
end
stop
coor (very long file)
elem (very long file)
zone (very long file)
test6.out (output file)
test6.fin (output file)
test6.his (output file)
test6.trc (output file)
test6.con (output file)
test6.dp (output file)
test6.stor (output file)
test6.chk (output file)
all
-0
```

title: 2d - Mortandad Canyon data needed for particle tracking simulation

```
#*********************75
pres
-1 0 0  0.974890977E-01   0.288141634E+00 2
-2 0 0  0.983598070E-01   0.290793914E+00 2
-3 0 0  0.796964858E-01   0.415766895E+00 2
-4 0 0 -0.287806941E-01   0.790719014E+00 2
-5 0 0 -0.114939565E+00   0.650872839E+00 2
-6 0 0  0.769448671E-02   0.677805465E+00 2
-7 0 0 -0.383920195E-01   0.858228610E+00 2
-8 0 0  0.200809939E-01   0.748442659E+00 2
-9 0 0  0.290226886E-01   0.773320457E+00 2

#*********************75
perm
-9    0  0  2.645e-13  2.645e-13    2.645e-13
-8    0  0  1.955e-13  1.955e-13     1.955e-13
-7    0  0  3.680e-13  3.680e-13     3.680e-13
-6    0  0  1.495e-12  1.495e-12     1.495e-12
-5    0  0  7.245e-13  7.245e-13     7.245e-13
-4    0  0  1.725e-13  1.725e-13     1.725e-13
-3    0  0  5.324e-12  5.324e-12     5.324e-12
-2    0  0  1.000e-13  1.000e-13     1.000e-13
-1    0  0  5.324e-12  5.324e-12     5.324e-12

#*********************75
rlp
3     .111    1.0     .138    1.583   2.      .061
3     .017    1.0     .044    1.660   2.      .019
3     .035    1.0     .222    1.592   2.      .028
3     .035    1.0     .187    1.481   2.      .027
3     .055    1.0     .066    1.711   2.      .036
3     .000    1.0    .081    4.026   2.     .010
3     .180    1.0     14.5    2.680   2.      .055
4     .066    1.0     3.84    1.474   2.      .076
     .03    1.0    3.84    1.474   2.     .020    1e-
06   1.e-13  1.e-4
3     .180    1.0     14.5    2.680   2.      .055

-9    0     0     1
-8    0     0     2
-7    0     0     3
-6    0     0     4
-5    0     0     5
-4    0     0     6
-3    0     0     7
-2    0     0     8
-1    0     0     9
```

```
#*********************75
rock
-9     0     0      1260    1000    0.460
-8     0     0      1180    1000    0.528
-7     0     0      1160    1000    0.509
-6     0     0      1250    1000    0.490
-5     0     0      1180    1000    0.469
-4     0     0      810    1000    0.667
-3     0     0      1200    1000    0.250
-2     0     0      1200    1000    1.e-4
-1     0     0      1200    1000    0.250

#*********************75
flow
 1   61   1   .1                      .99      1e-2
 3784   3842 1  -1.157D-03   0.9900000000  0.
 3783   3783 1   -5.786D-04   0.9900000000000
0.
 3843   3843 1   -5.786D-04   0.9900000000  0.

#*********************75
time
1.e2 1e4   50000    1  1995  5  0.0
1095 -2  1 1
2190 -2  1 1
3285 -2  1 1
4380 -2  1 1
5475 -2  1 1

#*********************75
ctrl
  15   1.e-3   8
  1    0 0 2
  0
  1.0  2   1.0
  10   1.2  1.e-10 1.825e12
  1  -1
#*********************75
iter
1.e-5 1.e-5 1.e-5 1.e-5 1.1
0 0 0 5  1200.
#*********************75
ptrk
28000 123456
0. 1e20 2e2 1e30
1 0 -3 0
1 0.0 9. 9. 9. 1e-10 1 .2 6.723e-8
```

```
1 0 0 1

3813 3813 1 500. 0. .00001

#*********************75
sol
1    -1
#*********************75
air
-1
20.0 0.1
#*********************75
text
Output Controls

#*********************75
cont
avs  50 2.0e155555
liquid
conc
end
stop
coor (very long file)
elem (very long file)
zone (very long file)
test6.out (output file)
test6.fin (output file)
test6.his (output file)
test6.trc (output file)
test6.con (output file)
test6.dp (output file)
test6.stor (output file)
test6.chk (output file)
all
-0
```

APPENDIX B: LIST OF SYMBOLS

L refers to length
m or M refers to mass
r refers to rock
l refers to liquid
A is the mass/unit volume $[M/L^3]$
f is the flux within the system $[M/t^3]$
q is mass flux $[M/t^3]$
Q is volumetric flux $[L^3/t]$
t is time
k is intrinsic permeability $[L^2]$
k_r is relative permeability [unitless]
ρ is the rock density $[M/L^3]$
P is pressure $[M/Lt^2]$
D is the transmissibility $[L^2/t]$
S_{flow} is the specified saturation [unitless]
S_l is the liquid saturation [unitless]
S_{lr} is the residual liquid saturation [unitless]
I is an impedance parameter [M/t]
$\overline{g}$ is the acceleration due to gravity $[L/t^2]$
θ is moisture content [unitless]
ϕ is porosity [unitless]
$\overline{v}$ is Darcy flux [L/t]
μ is the fluid viscosity [M/Lt]
P_{cap} is the capillary pressure [L]
P_o is the air entry pressure [1/L]
α is an experimentally determined van Genuchten parameter $[Lt^2/M]$
n is an experimentally determined van Genuchten parameter [unitless]
λ is an experimentally determined van Genuchten parameter [unitless]
K is hydraulic conductivity [L/T]
h is height [L]
A is area $[L^2]$
T is temperature in C°
I is a monthly heat index which is a function of T
i_n is the value of I for any particular month
I is the heat index
a is an empirical exponent
UPE is a monthly unadjusted potential evapotranspiration [L]
PE is a monthly potential evapotranspiration [L]
b is an adjustment factor [t]

REFERENCES

Abrahams, J.H., Weir J.E., and Purtymun, W.D., "Distribution of Moisture in Soil and Near-Surface Tuff on the Pajarito Plateau, Los Alamos County, New Mexico," *Geological Survey Research*, D142-D145p. (1961).

Abrahams, J.H., Baltz, E.H., and Purtymun, W.D., "Movement of Perched Groundwater in the Alluvium near Los Alamos, New Mexico," U.S. Geological Survey Professional Paper 450-B, 11p. (1962).

Baltz, E.H., Abrahams, J.H., and Purtymun, W.D., "Preliminary Report on the Geology and Hydrology of Mortandad Canyon near Los Alamos, New Mexico, with Reference to Disposal of Liquid Low-level Radioactive Waste" U.S. Geological Survey Professional Paper, 101p. (1963).

Birdsell, K.H., Soll, W.E., Bower, K.M., Wolfsberg, A.V., Orr, T.W., and Cherry, T.A., "Simulations of Groundwater Flow and Radionuclide Transport in the Vadose and Saturated Zones beneath Area G, Los Alamos National Laboratory", Los Alamos National Laboratory Report, LA-UR-97-157, 33pp. (1997).

Bishop, C.W., “Hydraulic Properties of Vesicular Basalt”, M.S. Thesis, University of Arizona, Tucson. 112pp. (1991).

Broxton, D.E., and Reneau, S.L., "Buried Early Pleistocene landscapes beneath the Pajarito Plateau, Northern New Mexico" *New Mexico Geological Society Guidebook, 47th Field Conference*, The Jemez Mountains Region, 325-334p. (1996).

Broxton, D.E., and Reneau, S.L., "Stratigraphic Nomenclature of the Bandelier Tuff for the Environmental Restoration Project at Los Alamos National Laboratory," Los Alamos National Laboratory Report LA-13010-MS, (1995).

Corey, A.T., Mechanics of Immiscible Fluids in Porous Media, Water Resources Publications, Highlands Ranch, CO., 252p. (1994).

Daniel B. Stephens and Associates, “Addendum to Laboratory Analysis of Hydraulic Testing for MCM 5.1 and MCC 5.9A Samples,” Prepared by Daniel B. Stephens and Associates, Inc., for Los Alamos National Laboratory, report no. DBSA/90-170/791-1 (1991a).

Daniel B. Stephens and Associates, “Laboratory Analysis of Soil Hydraulic Properties from TA-53 Impoundments Corehole #6, Corehole #7, and Corehole SIMO-1,” Prepared by Daniel B. Stephens and Associates, Inc., for Los Alamos National Laboratory, report no. DBSA/90-170/791-1 (1991b).

Davis, L.A., and Neuman, S.P., "Documentation and User's Guide: UNSAT2 - Variably Saturated Flow Model", U.S. Nuclear Regulatory Commission, NUREG/CR-3390 WWL/TM-1791-1 (1983).

Environmental Protection Group, "Environmental Surveillance at Los Alamos During 1993", Los Alamos National Laboratory Report LA-12973-ENV, (1994).

Gable, C.W., Personal Communication, (1998).

Gable, C.W., Cherry, T., Trease, H., and Zyvoloski, G.A., "GEOMESH Grid Generation" Los Alamos National Laboratory Report LA-UR-95-4143, 59p. (1995).

Geddis, A.M. "Preliminary Modeling of Moisture Movement in the Tuff Beneath Mortandad Canyon, Los Alamos National Laboratory", Los Alamos National Laboratory Report LA-UR-92-2577, 38p. (1992).

Goff, F., Gardner, J.N., Baldridge, J.B., Hulen, D.L., Nielson, D.L., Vaniman, D., Hiken, G., Dungan, A., and Broxton, D., "Excursion 17b: Volcanic and Hydrothermal Evolution of Valles Caldera and Jamez Volcanic Field," *New Mexico Bureau of Mines and Mineral Resources Memoir* 46, 381-434pp. (1989).

Hantush, M.S., "Potential Evapotranspiration in Areas along the Rivers of New Mexico", New Mexico Institute of Mining and Technology, 101p. (1959).

Koenig, E.D., and McLin, S.G.,"Application of a Lumped-Parameter Model Towards Understanding the Behavior of the Mortandad Canyon Perched Alluvial System, Los Alamos, New Mexico" Los Alamos National Laboratory Informal Report, 45p. (1992).

Lundquist, L. "Rectangular Grid Generator", Los Alamos National Laboratory Report, 10p. (1994).

Miera, F.R., Bostick, K.V., Hakonson, T.E., Nyhan, W., "Biotic Survey of Los Alamos Radioactive Liquid-Effluent Receiving Areas," Los Alamos National Laboratory Report, LA-6503-MS (1977).

Montazer, P., and Wilson W.E., "Conceptual Hydrologic Model of Flow in the Unsaturated Zone, Yucca Mountain, Nevada" U.S. Geological Survey Water-Resources Investigations Report 84-4345, 55p. (1984).

Mostafa, G.A.T.M., "Applicability of TRACR3D to Plutonium Migration", M.S. Thesis, New Mexico State University, Las Cruses, 107p.(1993).

Purtymun, W.D., "Progress Report on Hydrology of Mortandad Canyon Disposal System for Treated Low-level Radioactive Waste, June 1961 to June 1963," U.S. Geological Survey Admin. Report, 17p. (1964).

Purtymun, W.D., "Disposal of Industrial Effluents in Mortandad Canyon, Los Alamos County, New Mexico", Los Alamos Scientific Laboratory Report GS-LA-100, 74p. (1967).

Purtymun W.D., "Geohydrology of the Pajarito Plateau with Reference to the Quality of Water 1949-1972," Los Alamos Scientific Laboratory Report (1975).

Purtymun, W.D.," Geologic and Hydrologic Records of Observation Wells, Test Holes, Test Wells, Supply Wells, Springs, and Surface Water Stations in the Los Alamos Area," Los Alamos National Laboratory Report LA-12883-MS, 339p. (1995).

Rogers, D., and Gallaher, B.M., "The Unsaturated Hydraulic Characteristics of the Bandelier Tuff," Los Alamos National Laboratory Report LA-12968-MS, 76p. (1995).

Ross, B., “The Diversion Capacity of Capillary Barriers,” *Water Resources Research* 26, 2625-2629pp. (1990).

Ross, B., “Reply,” *Water Resources Research* 27, 2157pp. (1991).

Selker, J., “Design of Interface Shape for Protective Capillary Barriers” *Water Resources Research* 33, 259-260pp. (1997).

Stephens, D.B., see Daniel B. Stephens and Associates.

Stoker, A.K., Purtymun, W.D., McLin, S.G., and Maes, M.N. "Extent of Saturation in Mortandad Canyon", Los Alamos National Laboratory Report LA-UR-91-1660, p.136 (1991).

Stone, W.J., "Preliminary Results of Modeling the Shallow Aquifer, Mortandad Canyon, Los Alamos National Laboratory, New Mexico," NMED/DOE/AIP-95-1, 32p. (1995).

van Genuchten, M.T. "A Closed-Form Equation for Predicting the Hydraulic Conductivity of Unsaturated Soils," *Soils Science Society of America Journal* 44, 892-898pp. (1980).

van Genuchten, M.T., Leij F.J., and Yates S.R. "The RETC Code for Quantifying the Hydraulic Functions of Unsaturated Soils." U.S. Environmental Protection Agency Report EPA/600/2-91/065 (1991).

Vaniman, D., Cole, G., Gardner, J., Conaway, J., Broxton, D., Reneau, S., Rice, M., WoldeGabriel, G., Blossom, J., and Goff, F. "Development of a Site-Wide Geologic Model for Los Alamos National Laboratory", Los Alamos National Laboratory Report, p.42 (1997).

Vollick, T.K., "An Analytical and Numerical Method of Modeling the Migration of a Radionuclide Through the Perched Aquifer of Mortandad Canyon", M.S Thesis, New Mexico State University, Las Cruses, 123p. (1992).

Warrick, A.W., Wierenga, P.J., and Pan, L., "Downward Water Flow through Sloping Layers in the Vadose Zone: Analytical Solutions for Diversions", *Journal of Hydrology* 192, 321-337pp. (1997).

Water Quality and Hydrology Group, "Groundwater Discharge Plan Application for the TA-50 Radioactive Waste Liquid Treatment Facility" Los Alamos National Laboratory Report (1996).

Zyvoloski, G.A., Robinson, B.A., Dash, Z.V., and Trease, L.L., "Models and Methods Summary for the FEHM Application", Los Alamos National Laboratory Report LA-UR-94-3787, p.65 (1994a).

Zyvoloski, G.A., Robinson, B.A., Dash, Z.V., and Trease, L.L., "User's Manual for the FEHM Application", Los Alamos National Laboratory Report LA-UR-94-3788 (1994b).